SYNTHESIS AND CHARACTERIZATION OF NiMnGa FERROMAGNETIC SHAPE MEMORY ALLOY THIN FILMS

A Thesis

by

NISHITHA JETTA

Submitted to the Office of Graduate Studies of
Texas A&M University
in partial fulfillment of the requirements for the degree of

MASTER OF SCIENCE

August 2010

Major Subject: Mechanical Engineering

Synthesis and Characterization of NiMnGa Ferromagnetic Shape Memory Alloy Thin Films

SYNTHESIS AND CHARACTERIZATION OF NiMnGa FERROMAGNETIC SHAPE MEMORY ALLOY THIN FILMS

A Thesis

by

NISHITHA JETTA

Submitted to the Office of Graduate Studies of
Texas A&M University
in partial fulfillment of the requirements for the degree of

MASTER OF SCIENCE

Approved by:

Chair of Committee,	Xinghang Zhang
Committee Members,	Ibrahim Karaman
	Dimitris C. Lagoudas
Head of Department,	Dennis C. O'Neal

August 2010

Major Subject: Mechanical Engineering

ABSTRACT

Synthesis and Characterization of NiMnGa Ferromagnetic Shape Memory Alloy Thin Films.

(August 2010)

Nishitha Jetta, B.E., Osmania University

Chair of Advisory Committee: Dr. Xinghang Zhang

Ni-Mn-Ga is a ferromagnetic shape memory alloy that can be used for future sensors and actuators. It has been shown that magnetic field can induce phase transformation and consequently large strain in stoichiometric Ni_2MnGa. Since then considerable progress has been made in understanding the underlying science of shape memory and ferromagnetic shape memory in bulk materials.

Ni-Mn-Ga thin films, however is a relatively under explored area. Ferromagnetic shape memory alloy thin films are conceived as the future MEMS sensor and actuator materials. With a 9.5% strain rate reported from magnetic reorientation, Ni-Mn-Ga thin films hold great promise as actuator materials.

Thin films come with a number of advantages and challenges as compared to their bulk counterparts. While properties like mechanical strength, uniformity are much better in thin film form, high stress and constraint from the substrate pose a significant challenge for reorientation and shape memory behavior. In either case, it is very important to understand their behavior and examine their properties. This thesis is an

effort to contribute to the literature of Ni-Mn-Ga thin films as ferromagnetic shape memory alloys.

The focus of this project is to develop a recipe for fabricating NiMnGa thin films with desired composition and microstructure and hence unique properties for future MEMS actuator materials and characterize their properties to aid better understanding of their behavior. In this project NiMnGa thin films have been fabricated using magnetron sputtering on a variety of substrates. Magnetron sputtering technique allows us to tailor the composition of films which is crucial for controlling the phase transformation properties of NiMnGa films. The composition is tailored by varying several deposition parameters. Microstructure of the films has been investigated by X-ray diffraction (XRD) and transmission electron microscopy (TEM) techniques. Mechanical properties of as-deposited films have been probed using nano-indentation technique. The chemistry of sputtered films is determined quantitatively by wavelength dispersive X-ray spectroscopy (WDS). Phase transformation is studied by using a combination of differential scanning calorimetry (DSC), in-situ heating in TEM and in-situ XRD instruments. Magnetic properties of films are examined using superconducting quantum interface device (SQUID).

To my parents, my little sister and my beloved

ACKNOWLEDGEMENTS

In my journey of life, there have been many crossroads that helped me grow beyond myself. Of all these places, Aggieland is probably the most special. My last 3 years here have been enriching and life changing. The advice, responsibility, honor, memories, lessons I have been rendered in this one place are more than I could ever hope for. Before I get flushed out into the big bad world, I want to thank everyone who has touched my life in the last 3 years.

The list has to start with my advisor, Dr. Xinghang Zhang who has been one of the biggest inspirations. He has not just taught me technical skills, but imbibed values that I will cherish for the rest of my life. Thanks to my committee members, Dr. Ibrahim Karaman and Dr. Dimitris Lagoudas for their continued support and advice. Dr. Haiyang Wang has been very kind in letting me use their equipment for my research.

Some of the most boring days in research seemed interesting and intriguing alongside Steven Rios, Dan Bufford, Byoungsoo Ham, Yue Liu, Jeremy Gonzalez, Cheng Sun, Kaiyuan Yu, Osman Anderoglu, Nan Li and Engang Fu. If there was one person without whom I could not finish my project, it would be Steven. I am deeply thankful to him for being more like an inspiration than a collaborator. It was a pleasure to have worked with a collaborator like Nevin who went out of her way to help me finish my work on time.

My experience at Texas A&M would not be as fun without all the friends I made here. Thanks to my friends Nikhila, Soumya, Aswani, Geetha, Shantala, Deepthi, Divya,

Kalpana, Sireesha, Naveen, Ramnath, Aravind, Sandip and Manish for counting the days with me and making it seem like help was just a phone call away.

Finally, I have to thank my parents, sister and beloved without whom any achievement wouldn't mean anything. No acknowledgement would measure up in thanking my father, Sudhakar Jetta and mother, Arundathi Jetta who inspired me to dream big and filled my life upto the brim with love. Having my uncle, Chinnappu Reddy Katakam who has inspired me to look beyond my materialistic needs and see life in a different light has been an asset. Homesickness has never been a part of my graduate life, thanks to my cousins, Prabhakar Mekala, Samyuktha Mekala, little Tanvi and Minnathi who have given me a home away from home during these 3 years. Life would not have been worth looking forward to and so much fun if it wasn't my little sister, Deekshitha Jetta and my best friend, Ashwini Prasad Kalapala who tap my back and lend me a giggle whenever I need one.

TABLE OF CONTENTS

Page

Page

LIST OF FIGURES

FIGURE Page

FIGURE Page

FIGURE Page

FIGURE Page

LIST OF TABLES

1. INTRODUCTION

There has been continuous technological interest and challenge for developing active actuator materials that exhibit large strains with a rapid response time [1]. A number of active materials like rare earth alloys, $TbFe_2$, Terfenol-D that show magnetostriction of a few percent strain under an applied magnetic field [2, 3] have been proposed as actuator materials. These alloys are plagued with some disadvantages like poor electrical and thermal conductivity at elevated frequencies (unless they are used with small lateral dimensions). For practical field-induced-strain type of applications like actuators, larger strains that are available at high frequency of operation are desirable.

Shape memory materials that undergo a diffusionless, displacive, structural martensitic transformation can exhibit super-elasticity of a few percent and thermally recoverable strains as large as 15% (eg. Cu-Al-Ni) [4]. As the name suggests, these materials have an ability to reverse a large stress induced deformation in martensitic phase on heating above their transformation temperature. In many materials this transformation can also be achieved by an applied stress. However, heating or cooling through a transformation temperature is not an efficient method of actuation for many applications. Heating also has disadvantages of poor energy conversion and slow response time that limits the applicability of shape memory actuators.

This problem, slow response time, can be addressed by materials in which

---

This thesis follows the style of Advanced Materials Research.

magnetic field can be used to induce shape memory effect. These materials are called magnetic shape memory alloys (MSMA). In MSMA's, large thermo-elastic strain related to shape memory effect can be achieved by application of a magnetic field on martensites which are ferromagnetic. Very large strains as high as 9.5% can be captured by magnetic field induced reorientation (MFIR) which involves reorientation of the grains to align themselves in the direction of magnetic field [5]. In 1996 Ullakko suggested the mechanism of magnetic field induced strain (MFIS) in MSMA's with large magnetic anisotropy. The mechanism is based on the MFIR of the crystallographic domains (twin variants) that have lower magnetization energy [6].

In other words, if magnetic field is applied in the direction of an easy axis of one variant, it enables this variant to grow in volume at the expense of the martensite variants with different easy axis directions [5]. In materials with a transformation temperature below room temperature, magnetic field can be used to induce phase transformation. This is called Magnetic Shape Memory Effect (MSME). Magnetic field can be switched at high frequencies and is very easy to incorporate into applications operated with electric energy. Hence, magnetic field control of the shape memory is suggested as a principle of operation for a new class of actuator materials. Henceforth research has been focused on the pursuit of a magnetic alloy that will allow control of large displacements by application of a magnetic field at constant temperature [7].

Ni-Mn-Ga system which belongs to the family of Heusler alloys has been an interest of research after it was observed that 0.2% of strain can be induced by Magnetic

field of 8 kOe at 265 K [8]. Table 1.1 below is a comparison of the properties of important active materials that have been the interest of research in the past decade.

TABLE 1.1 Comparison of active materials [9].

	Magnetostr. Terfenol - T	**Multilayer Piezo**	**Bulk Piezo (PZT)**	**MSMA Ni-Mn-Ga**
Control Field	Magnetic	Electric	Electric	Magnetic
Max. strain ξ(μm/mm), linear	1.6	1.25	0.3	100
Work output, σ bl xξ(MPA X μm/mm)	112	25	6	300
Young's modulus (GPa)	25-35	45-62	48-74	7.7
Compressive strength (MPa)	700	50	60	700
Curie Temperature (˚C)	380	200-350	200-350	103
Max. operating temperature (˚C)	150	100	100	70
Resistivity (Ωm)	58×10^{-8}	10^{10}	10^{10}	80×10^{-8}
Relative permittivity	N/A	800 -2400	800-2400	N/A
Relative permeability	3 -10	1	1	1.5 - 40
Coupling factor (%)	75	70	75	75
Max. energy density (kJ/m^3)	27	18.5	2	90
Field strength for max. strain	240 kA/m	2MV/m	2MV/m	400kA/m

In addition to very high work outputs Ni-Mn-Ga has low resistivity and good mechanical strength especially in thin film form, making it very attractive for various applications.

High work outputs are particularly desirable in micro actuator systems as contactless control of large deformations is not easily achievable by other actuation principles in micro or nano space. Several applications have been developed using Ni-Mn-Ga thin films as micro actuator materials [10, 11]. Hence, it is important to study the properties of these technologically important materials with potential use as the future MEMS actuators and sensors. This work will outlay an effort to understand the mechanical, magnetic, structural and thermal properties of some interesting compositions of off-stoichiometric Ni-Mn-Ga alloys.

1.1 SHAPE MEMORY EFFECT

1.1.1 Phenomenon of shape memory effect

Shape memory effect is a phenomenon observed in some materials that exhibit two phases – austenite and martensite. The phase transformation between these two states is diffusionless and can be triggered by a change in either temperature, magnetic field or other variables. The transformation occurs at a particular temperature called "phase transformation temperature". Above this temperature the material has austenite phase that exhibits a highly ordered cubic structure, while below this temperature a more disordered structure called martensite exists. Martensite state which usually exists in

more than one variant is a disordered form of cubic structure – usually tetragonal, monoclinic, triclinic etc.

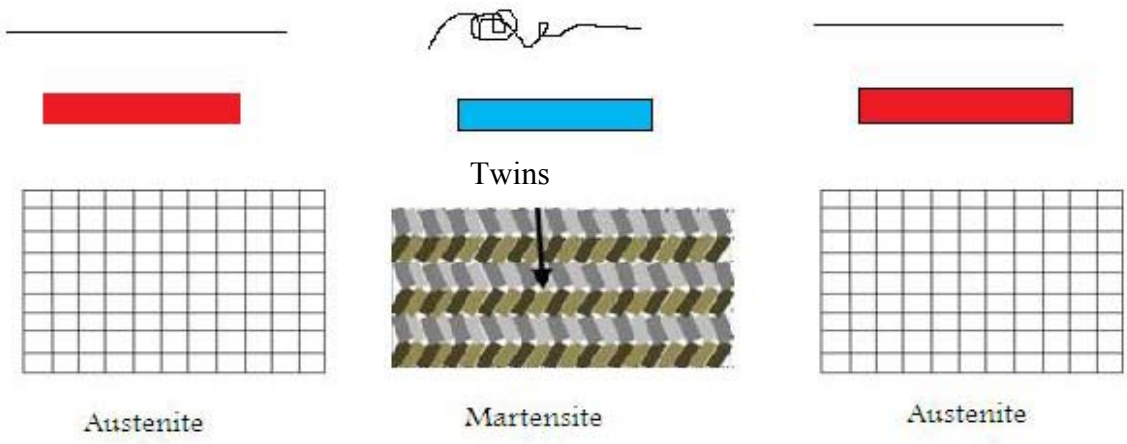

FIG.1.1 Schematic of shape change and structures of a trained shape memory material.

A variant here refers to martensite with a slight variation in crystal structure or orientation. These variants exist together and form twins. The picture above shows a schematic of a twinned martensite structure. The grey and green colors represent, two different variants, while the lighter and darker colors refer to the fine twins in a single variant which are oriented 180° to each other. This complex structure of martensite enables it to undergo large magnitude of deformation without experiencing plastic strain. On heating, the crystal structure reorders to form a Face centered cubic structure. In a trained shape memory material, the initial geometry would be recovered back giving it the name shape memory.

1.1.2 Thermal SME

Thermodynamically shape memory effect is related to the free energy of martensite and austenite states [12]. At temperatures below transformation temperature, the free energy of one phase becomes less than the other making it more stable at that temperature. At temperatures above transformation temperature the second phase becomes more stable resulting in a phase transformation into the second phase. The highly ordered phase is referred to as austenite, while the disordered phase is referred as martensite. The phenomenon of phase transformation caused due to a change in temperature is referred as thermal shape memory effect.

As described above, austenite and martensite phase's exhibit different crystal structures enabling shape memory. Phase transformation is characterized by four temperatures A_s, A_f, M_s, M_f which stand for austenite start-temperature, austenite finish-temperature, martensite start-temperature, martensite finish-temperature respectively. In an alloy like Ni-Mn-Ga where the higher temperature phase is cubic austenite and lower temperature phase is non-cubic martensite, the volume fraction of austenite – martensite w.r.t. temperature during phase transformation is shown in the Figure 1.2. It should be noted that a hysteresis in forward and reverse transformation is observed mainly because of energy dissipation during transformation. Typically, this effect is irreversible or one-way. By subjecting the material to a process called training, a reversible two way shape memory effect can be achieved in the material.

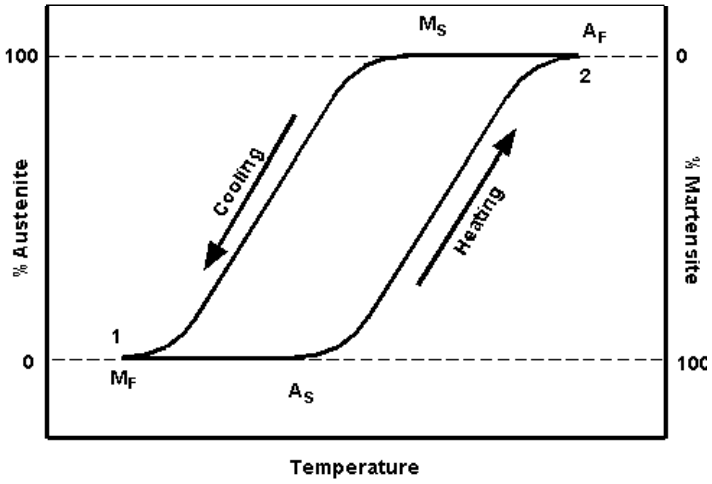

FIG. 1.2 Volume fraction of austenite – martensite during phase transformation [13].

1.1.3 Stress induced SME - Pseudoelasticity

Shape memory materials, when subjected to stress above a critical value, undergo elastic deformation that is almost fully recoverable on removing the stress. This superelastic-like behavior is termed as pseudoelasticity. When external stress is applied, the austenite phase transforms into martensite phase. The martensite phase has the ability to form a self accommodating complex variant structure which is capable of undergoing deformation without any plastic strain. When the stress is removed, the material undergoes a reverse phase transformation, i.e. reverts back into austenite phase without signs of deformation.

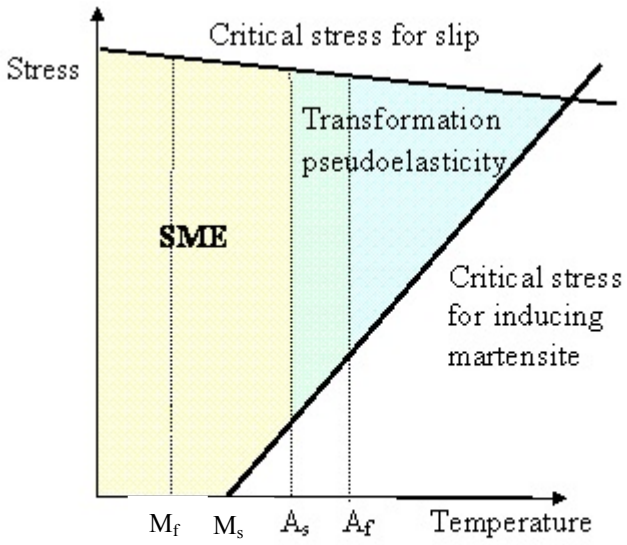

FIG. 1.3 Psuedoelasticity - stress vs. temperature behavior [14].

It should be noted that stress above a critical value is necessary for inducing this transformation. Figure 1.3 shows the variation of critical stress with the temperature. From M_f where the material is fully maternsite, the value of critical stress increases from zero as the temperature is increased.

Pseudoelasticity in Ni-Ti alloy has been used to make biomedical stents, scratch free eye glass frames, antennas etc. When stress is above critical stress, martensite phase is induced.

1.1.4 Magnetic field induced shape memory effect

In traditional SMA's phase transformation was accomplished by altering the temperature. It was later discovered that shape change can also be achieved by varying

the magnetic field. This phenomenon is explained by Magnetocaloric effect. It states that the magnetic and caloric variables are interrelated in materials exhibiting this effect [12]. By virtue of this effect the magnetization (M), temperature (T) and strain (ξ), which are the conjugate variables of magnetic field (H), entropy (S) and stress (σ) are inter-correlated.

Hence in the vicinity of phase transformation temperature, a slight change in magnetic field will induce a change in entropy, and in turn magnetic field induced phase transformation. If the austenite and martensite phases are ferromagnetic as in the case of Ni-Mn-Ga, this effect is referred as Ferromagnetic shape memory effect. Of all shape memory effects discovered, magnetic field induced shape memory effect is most conducive to application due to its high response frequency and large actuation strain. In practice, it is much more rapid to apply and control magnetic field than temperature to trigger shape memory effect.

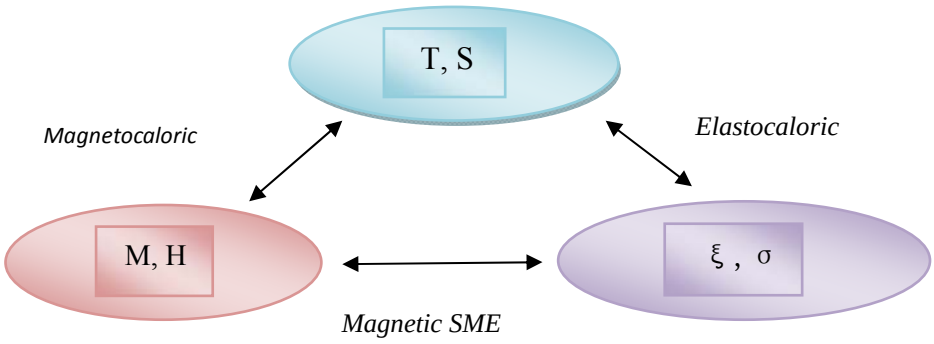

FIG. 1.4 Relationship between properties in ferromagnetic materials.

1.2 FERROMAGNETIC SHAPE MEMORY EFFECT

If both the martensite and austenite phases in a shape memory material are ferromagnetic, then that material is called a ferromagnetic shape memory material (FSM). To date strains as large as 9.5% [6] have been reported in FSM's. This is possible due to a unique mechanism called magnetic field induced re-orientation (MFIR) observed in this class of materials.

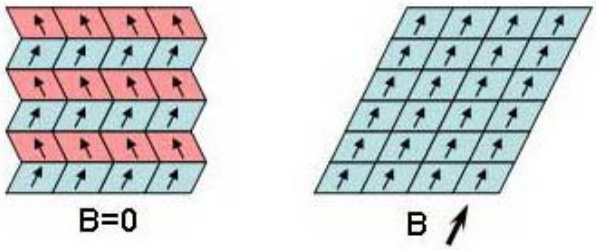

FIG. 1.5 Schematic of magnetic field induced re-orientation.

In these materials, the twin variants in martensite have magnetic moments in different directions. On the application of magnetic field of high intensity, the variants that are not aligned with the applied field, de-twin to align their moments with the external magnetic field. This movement results in a macroscopic change in the length resulting in strain.

Due to their technological importance, there has been a quest to find materials that are FSM's. It was discovered that Heusler alloys which were invented as early as 1903, fit into this class of materials. Since then a number of Heusler alloys like

Ni_2MnGa, Ni_2MnAl, Co_2MnAl, Pd_2MnGe, Cu_2MnSn, Fe_2VAl etc. have been extensively studied and successfully tested for Ferromagnetic Shape memory effect.

1.2.1 Heusler alloys

Heusler alloys are a series of metal based alloys that are ferromagnetic even though the constituent metals are non- magnetic. In 1903 Heusler et al. discovered that a copper based alloy, Cu_2MnSn showed saturation magnetization greater than ferromagnetic Ni [8]. It was later deduced that certain combinations of inter-metallics with the formula X_2YZ with XYZ belonging to the groups shown in Figure 1.6 showed Heusler phases. The X and Y atoms are transition metals while Z is either a semiconducting atom or non-metal.

The enhanced magnetism in these materials is a result of *double exchange mechanism* which will be described in the following sections. Depending on the alloy composition, Heusler alloys are of two types, *half Heusler alloys* (XYZ) and *full Heusler alloys* (X_2YZ). These two alloys differ not only in composition but also in structure and hence shape memory properties. Since shape memory is very closely associated with structure, it is important to study the structure of these alloys.

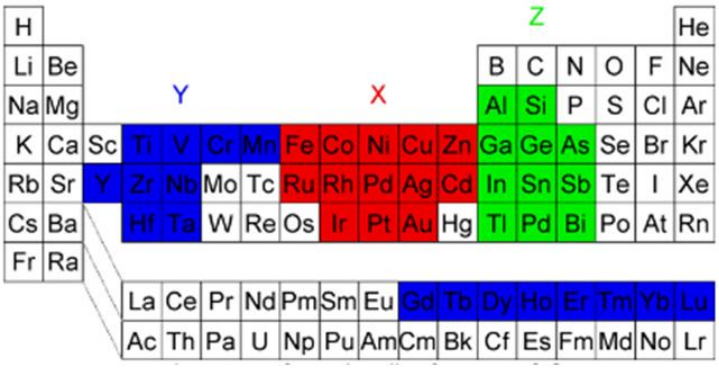

FIG. 1.6 Heusler alloy components [15].

1.2.2 Heusler alloys - Structure

As mentioned above, the property of shape memory is very sensitive to crystal structure of both austenite and martensite phases. Since the martensite phase is usually the disordered form of the austenite phase, it is very important to understand the structure of austenite. In this section, the structure of highly-ordered austenite phase in Heusler alloys will be discussed.

Webster et al. studied the structure of Heusler alloys and determined that they have a face centered cubic (FCC) structure in austenite phase [16]. As mentioned above the Heusler alloys with an empirical formula X_2YZ are referred to as *full heusler alloys*. They exhibit a $L2_1$ structure that resembles four interpenetrating f.c.c lattices as indicated in Figure 1.7 (b). In the structure, X atoms occupy the body centered positions in sub unit cells while the Y and Z atoms take the corner positions in the unit cell.

In half- heusler alloys, showing $C1_b$ structure, four of the body centered positions in sub-unit cells are empty, while the rest of the unit cell is the same as indicated in Figure 1.7 (a).

Heusler alloys are very sensitive to atomic disorder. In the $L2_1$ structure, a slight disorder in Y-Z atoms leads to a B2 structure shown in Figure 1.7 (c). A further disorder in X-Y and Y-Z atoms leads to a highly disordered A2 structure shown in Figure 1.7 (d).

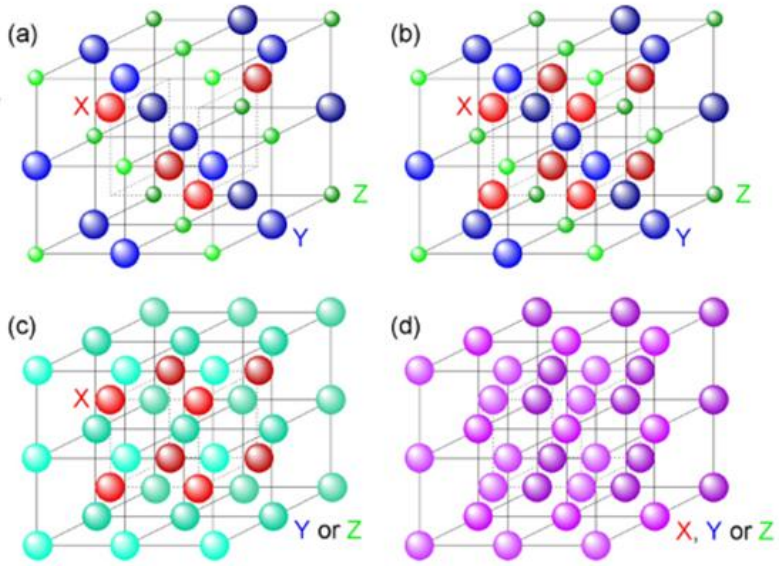

FIG. 1.7 Structure of Heusler alloys [15].

1.2.3 Heusler alloys - Magnetism

Heusler alloys are the most widely studied half metallic ferromagnetic (HMF) materials. These materials are characterized by the occurrence of anti-ferromagnetic and ferromagnetic properties although the constituent elements are not magnetic [17]. This is possible due to the alignment of adjacent d-shells of the transition elements. This

mechanism, proposed by Zener in 1951 [18] points out that the electron movement from one atom to the other is easier when the electron need not change its spin. In addition, the movement of electron results in reduction of kinetic energy. This behavior stands in accordance with the ease of existence of configurations having electrons aligned in one direction as stated by Hund's rule.

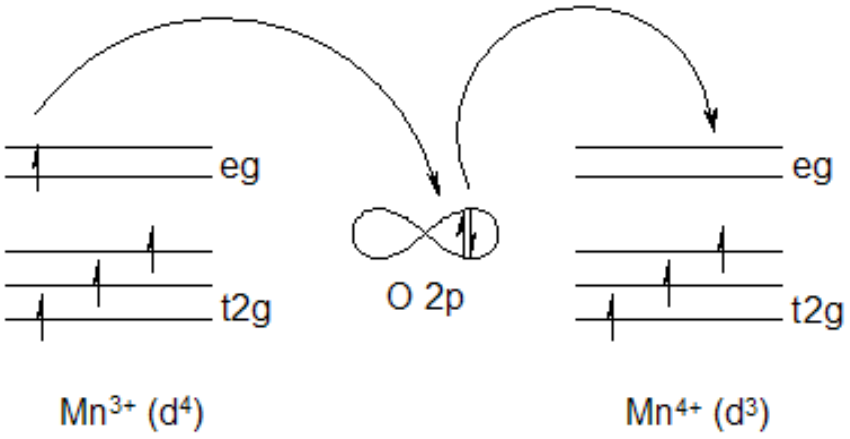

FIG. 1.8 Double exchange mechanism in Mn_2O.

For example, in Mn_2O the electron takes a 180° path in Mn-O-Mn bond to migrate from Mn^{3+} to Mn^{4+} via oxygen 2p orbital resulting in greater spin polarization. Hence, spin polarization which is very closely related to electrical conductivity and magnetism leads to ferromagnetic behavior.

1.3 NiMnGa HEUSLER ALLOYS

Heusler alloys are a series of intermetallics that exhibit special properties. These alloys usually have FCC like $L2_1$ structure and exhibit ferromagnetism even though the alloy constitutes don't. For instance, Cu_2MnSn alloy exhibited a magnetism of 8,000 gauss, exceeding that of Nickel (6100 gauss). It was later conferred that even though the constituent elements are not magnetic, these alloys show high levels of magnetism with *Double Exchange Mechanism*.

1.3.1 History

In 1960 Hames reported that the intermetallic compound Ni_2MnGa exhibits ferromagnetism [19]. X-ray and neutron diffraction studies suggest that the alloy has a highly ordered $L2_1$ structure at room temperature. Also the magnetism and structure of the unit cell depend on heat treatment conditions and the chemical composition of the alloy [20, 21]. Stoichiometric composition of the ferromagnetic alloy has a curie temperature of ~376K and a magnetic moment of 4.17, which is largely concentrated on the 'Mn' atoms located in the body center [22]. It has been observed that the Curie temperature is a function of e/a value [23]. Webster et al. reported that Ni_2MnGa exhibits Face Centered Cubic (FCC) structure at room temperature and transforms to a complex tetragonal structure when cooled to 202K [16].

1.3.2 Structure

Ni-Mn-Ga alloys exhibit a cubic $L2_1$ structure (space group: $Fm\bar{3}m$) in austenite phase below 600 °C [24]. The structure resembles four interpenetrating Face Centered Cubic (FCC) sub-lattices. Ni atoms occupy the corner positions in the unit cell while Mn and Ga reside in the sub lattice centers. Although Ni occupies the body center of the unit cell, most of the magnetic moment lies with the Mn atoms occupying the body center positions in the sub lattices.

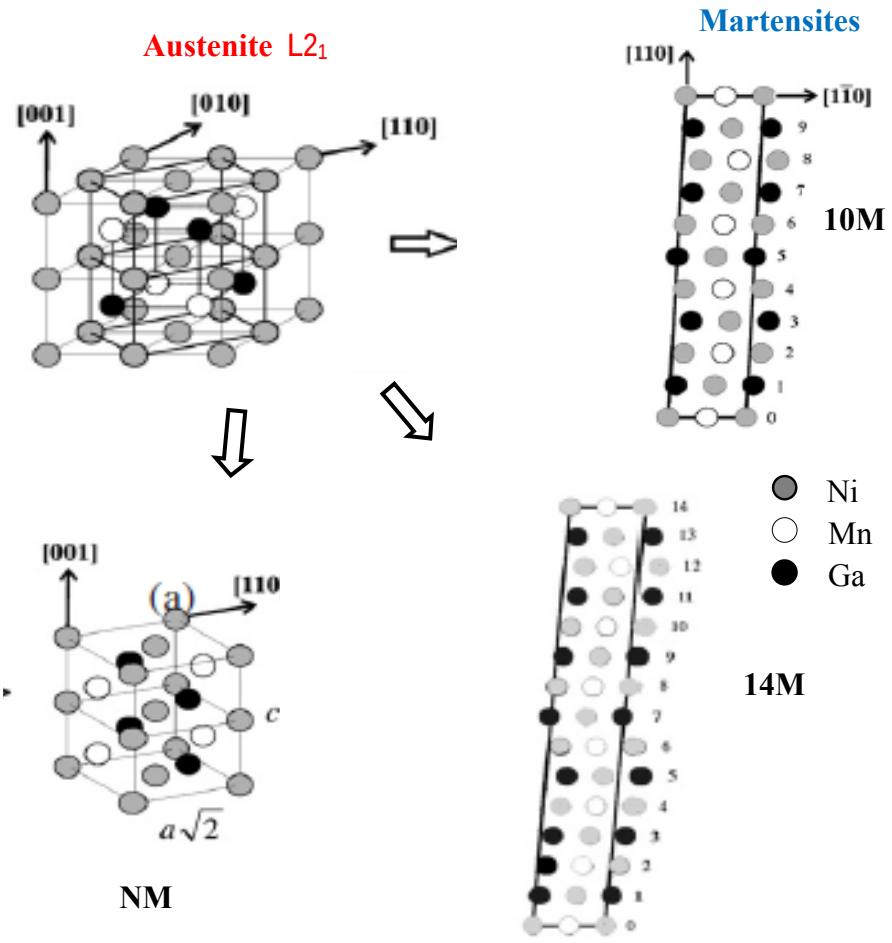

FIG. 1.9 Austenite – Martensite crystal structures in Ni-Mn-Ga [12].

Note: The martensite structures in the above figure have been designated in Modulate approach. In periodic stacking approach 10M, 14M and NM would correspond to 5M, 7M and 2M

The stoichiometric Ni_2MnGa undergoes a martensitic phase transformation to one of the martensitic structures shown below without any volume change [12]. This makes it is easy to visualize the change in crystal structure from austenite to martensite. The resulting martensite structure depends on a number of conditions like composition, processing conditions etc. [12, 23, 25].

In shape memory alloys numerous forms of martensitic phases have been reported. Several of them have layered structures with periods ranging from 2-10 planes. The structure of these martensite phases characterized by super-lattice dots in selected area diffraction (SAD) pattern is very complicated and has been the interest of research. Efforts have been made to develop an accurate interpretation of these structures. In the literature, two predominant methods have been in use [26].

a) **Periodic stacking** of nearly closed-packed planes
b) **Shuffling** of atomic planes – **Modulated structure**

1.3.2.1 Periodic stacking

This approach describes the layered martensite structures as long period stacking of close-packed planes derived from the {110} type planes of cubic $L2_1$ austenite or {111} planes of $L1_0$ cell. The unit cell is described as a monoclinic lattice giving the term 'M' in the denomination of 5M, 7M or NM. The crystallographic a, b, c axes of the monoclinic unit cell are aligned along $[1\bar{1}0]$, [001], [110] axes of the cubic austenite cell respectively.

Figure 1.10 shows the correspondence between austenite and martensite structures of Ni-Al alloy. In periodic stacking approach, $L1_0$ axes of the face-centered-tetragonal martensite are used to construct the unit cell. They are commonly referred to as "monoclinic axes". The bct axes indicated in (b) are used to construct the unit cell in modulate approach. They are referred to as "Cubic axes" and are parallel to the cubic austenite axes.

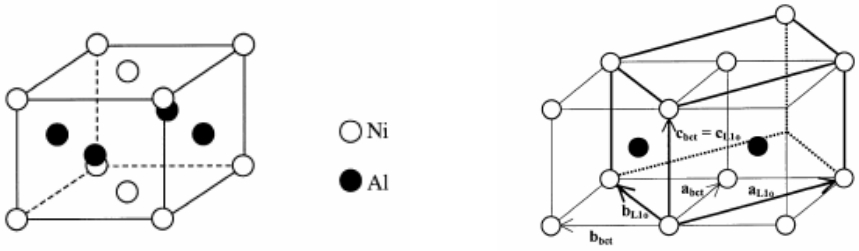

FIG. 1.10 (a) $L1_0$ unit cell in Ni-Al alloys (b) Lattice correspondence of "cubic" and $L1_0$ axis. [27].

Martensite structures with this monoclinic unit cell follow different stacking sequences. The 5M martensite are known to have a $(3\bar{2})_2$ sequence while the 7M martensite has $(5\bar{2})_2$ sequence in Zhdanov notation.

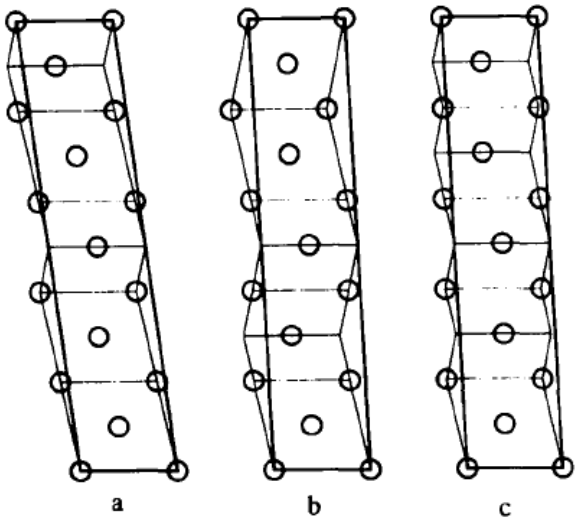

FIG. 1.11 Three possible stacking sequences for periodically stacked 5-layered martensite (a) $(4\bar{1}\bar{1})_2$ (b) $(32\bar{2})_2$ (c) $(2\bar{1}\bar{1}1\bar{1})_2$ [28].

1.3.2.2 Modulated approach

In this approach the axes of the martensite unit cell are parallel to the cubic austenite phase. The modulated structure is described by using crystallographic axes along $[\bar{1}\bar{1}0]$, [001] and [110] direction (the same as the "monoclinic axes" of periodic stacking approach. The cell is considered to be modulated by shuffling of the basal planes along $[\bar{1}\bar{1}0]$. The displacement of each j plane from its regular position is given by a function Δ_j where

$$\Delta_j = A \sin(2\pi j/L) + B \sin(4\pi j/L) + C \sin(6\pi j/L) \quad [29]$$

Where ‘L’ is the modulation period

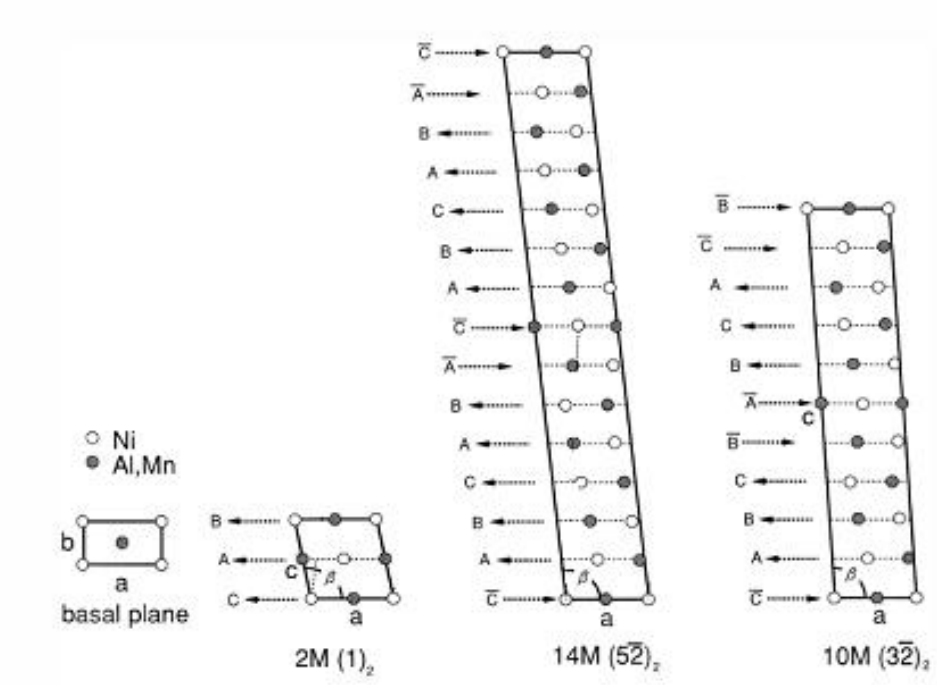

FIG. 1.12 Crystal structure of NM, 5-layer, 7-layer martensite in modulated approach [29].

Figure 1.12 shows the modulated structure of 2M, 10M and 14M structures obtained by periodic shuffling of A, B, C plane. The periodic shuffling follows a sequence as given by Zhadanov notation. The modulation in the structure is described as shuffling of the basal planes along $[\bar{1}10]$ as described above.

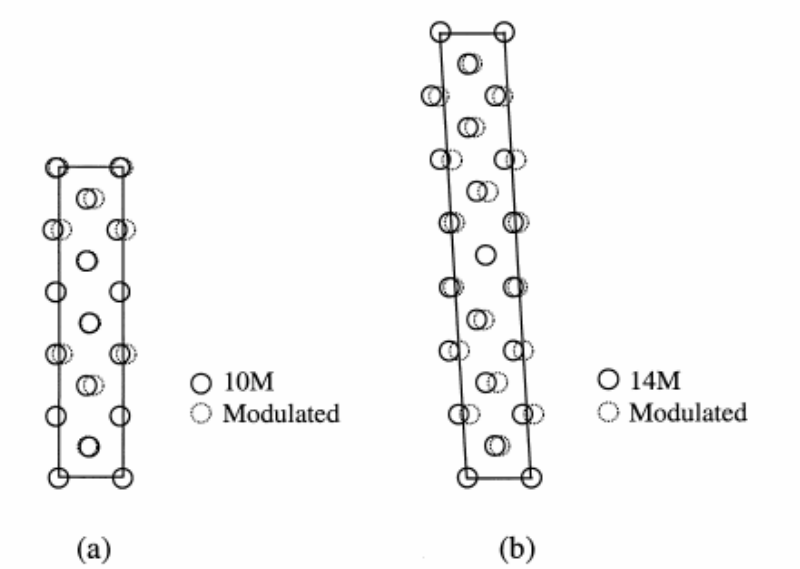

FIG. 1.13 Comparison of martensite structure constructed using periodic stacking and modulated structure approach for (a) 5-layered (b) 7-layered martensite [27].

HRTEM and atomic simulation studies have been used to discern the accuracy of the periodic stacking and shuffling approaches. While the periodic stacking approach is widely agreed to be accurate for 5-layered martensite structure, the modulated approach has been deemed to be more accurate for 6, 7, 10, 12 layered martensite structures [26 , 27, 28, 29].

1.4 NiMnGa THIN FILMS

With a 9% magnetic field induced strain reported [6], Ni-Mn-Ga is a very attractive material system not just for actuator applications but also a model system for fundamental research to understand the formation and propagation of magnetic domains in martensite phase.

Extensive research has been centered on bulk Ni-Mn-Ga to understand its mechanical and magnetic properties and phase transformation behavior. This system in bulk form is in general very brittle in polycrystalline state, making it difficult to deform into desirable shape. Ductility can be improved in a single crystal or thin film form. Poly-crystalline thin films deposited with various physical vapor deposition (PVD) methods show superior mechanical properties [30, 31].

Ni-Mn-Ga thin films are promising candidates for actuators in future MEMS devices. Micro-actuation models taking advantage of magnetic field induced re-orientation and magnetic shape memory effect have been proposed [10,11, 32, 33, 34, 35]. With magnetic field operation, they are bound to have the advantage of quick response, efficient energy conversion and high frequency operation provided a good control of microstructure and composition can be attained.

1.4.1 Deposition

A variety of techniques like sputtering [11, 36, 37, 38, 39], melt-spinning [39], pulsed laser deposition [32, 38], molecular beam epitaxy [40], flash evaporation [41] have been used to deposit thin films.

Radio frequency (RF) and direct current (DC) sputtering techniques have been used to deposit polycrystalline [38] and epitaxial thin films [11]. Using Sputtering it is easy to tailor the composition which is a critical parameter for many desired properties related to actuation and shape memory. Composition can be tailored either by varying

the deposition parameters such as deposition power, base pressure, target temperature or by using co-sputtering method.

Depositions can be performed at room temperature or elevated substrate temperatures. Films deposited at room temperature can have amorphous or nano-crystalline structure [42] and need to be annealed to obtain better texture and in turn that show enhanced magnetic and shape memory properties.

1.4.2 Composition and microstructure

It is challenging to deposit films with unique microstructure and composition that can deliver advanced shape memory properties. Microstructure and chemistry of films affects the mobility of martensite variants and the critical stress for inducing permanent strain in martensite [43] and in turn very closely related to shape memory properties of thin films. The deposition method needs to tune both microstructure and composition well. Sputtering is an effective technique. Using co-sputtering the composition of NiMnGa can be fine tuned by adding Ni or Mn to vary the overall composition. Usually the thin film is found to have ~ 3-5% increase in Ni and a corresponding decrease in Mn and Ga depending upon the deposition parameters [44, 45]. Desired thin film composition can also be obtained by appropriate adjustment of target alloy composition.

By selecting a target composition to compensate for the loss of volatile Mn and Ga at high temperatures during deposition, a uniform stoichiometry is preserved in the deposited films. Substrate temperatures in the range of 250 - 800 °C resulted in thin films with desirable texture, phases, and grain size [11, 45, 46].

1.4.3 Epitaxial and polycrystalline films

Expitaxial films can be considered as the most promising structure for microactuators. With no grain boundary constraint, single crystal samples can lead to the highest strains. Ni-Mn-Ga epitaxial thin films have been deposited using pulsed laser deposition (PLD) [45] and magnetron sputtering techniques [11, 37, 46].

Ferromagnetic shape memory behavior in a free standing bridge structure of an epitaxial film has been demonstrated by Dong et al. [47]. In substrate constrained epitaxial films, room temperature shape memory effect has been observed [46]. Heczko et al. showed that thin films deposited on $SrTiO_3$ substrate showed epitaxial structure with a twinned orthorhombic martensite [46]. Khelfaoui et al. reported epitaxial thin film deposition on Mg (001) substrate using DC magnetron sputtering at substrate temperature of 350 °C [11]. The films were partially released and showed martensite phase transformation. Magnetically induced re-orientation in constrained film has been reported by Thomas et al. [37]. Ni-Mn-Ga films deposited on MgO (001) substrate at elevated temperature has been used to demonstrate MFIR effect [37].

Although epitaxial films are of tremendous research interest for the study of maximum strain, developing a recipe for fabricating polycrystalline magnetic shape memory films is of immense technological interest. Polycrystalline films can be deposited at room temperatures on Si substrate [38]. Being the most commonly used material in semiconductor fabrication, the use of silicon gives the advantage of transferable micro-fabrication methods for making actuators in the future. Free standing

thin films have been fabricated using PVA substrate or simply peeling out thin films from the substrates after deposition [35].

1.4.4 Influence of heat treatment

As-deposited thin films deposited by magnetron sputtering at room temperature are partially crystalline with little or no magnetic and shape memory properties [44]. Thermal annealing is necessary for magnetic ordering and grain growth that facilitate ferromagnetic and shape memory behavior. Grain boundaries act as a barrier for shape change while structural order is necessary for the magnetic dipoles in the unit cells to align for ferromagnetic behavior [36].

In the literature three different types of annealing procedures have been proposed. a) in-situ annealing during deposition, b) ex-situ homogenization and ordering and c) ex-situ rapid thermal annealing (RTA). We now briefly describe the three techniques

(a) In-situ annealing: In this case, the substrate is held at elevated temperatures (300-800°C) during deposition. Higher substrate temperature increases the mobility of ad-atoms as compared to the bulk diffusion process in ex-situ annealing, and allows the substrate to act as an effective template for getting textured films. Vovk et al. suggested that post deposition annealing gives partial recovery of crystal structure and magnetic properties. They demonstrated that of crystal structure and magnetic properties of thin films deposition on substrate held at higher temperatures is more well defined compared to room temperature deposited thin films annealed at the same temperature [42].

Thermal energy imparted to the thin film during the deposition facilitates crystallization and ordered growth of the thin film during the deposition process. Zhang et al. showed that in-situ deposition gives thin films with a high degree of crystallinity, chemical uniformity and morphology [45].

(b) Ex-situ homogenization and ordering: Annealing using ex-situ homogenization and ordering involves two steps. A high temperature annealing at 800 - 1000°C intended to induce chemical order followed by a low-to-intermediate temperature anneal at 250 - 600°C for structural ordering in the thin films. This method is a replication of bulk heat treatment procedure for Ni-Mn-Ga alloys. High temperature chemical ordering is also found to suppress the formation of γ' precipitates in high temperature compositions [25]. Suzuki et al. demonstrated two-way shape memory effect in a low constrained aged thin film subjected to low temperature annealing.

(c) Rapid Thermal Annealing: Rumpf et al. showed a similar behavior of small scale ferromagnetism and long-range ordering induced during post-deposition annealing [36]. In their work rapid thermal annealing (RTA) technique that is usually employed in semiconductor fabrication for achieving structural order without chemical intermixing of layers is employed for Ni-Mn-Ga thin films that are plagued with loss of volatile Mn and Ga during annealing. Ferromagnetism that requires short range order sets in at lower temperature anneals while shape memory behavior sets in after a critical gain size is achieved at higher temperatures.

1.4.5 Challenges

In spite of the progress made in studying NiMnGa alloys, significant scientific and technical challenges remain as follows:

- Free-standing films - Releasing substrate constraint to harvest achievable macroscopic strains from MFIR and magnetic shape memory effect in thin films on substrates [46].
- Phase stability - The formation of non-transformable $L1_2$ phase in Ni-rich compositions during thermal annealing will reduce the transformation strain [25, 48].
- Oxidation issue - The formation of MnO during deposition and heat treatment have detrimental effect on mobility of magnetic domain boundaries [49].
- Integration - Developing a processing technology for the integration and fabrication of free-standing microactuators of Ni-Mn-Ga thin films with movable parts [11].

1.5 PHASE TRANSFORMATION INDUCED EVOLUTION OF PHYSICAL PROPERTIES

In magnetic shape memory alloys like Ni-Mn-Ga drastic change in the behavior of materials is observed over phase transformation. A change in thermal, mechanical, electrical and magnetic properties with phase transformation have been observed in this material [6, 25, 37, 50, 51, 52, 53]. Changes in these properties can be used to detect phase transformation characteristics like transformation temperature and hysteresis. In this section, some of the phase transformation induced evolution of physical properties will be described.

1.5.1 Crystal structure

The phenomenon of lattice instability plays a key role in phase transformation of shape memory alloys. In Heusler alloys like Ni-Mn-Ga where Ni atoms exist in a BCC type environment in austenite state, a tendency to occupy more stable natural FCC lattice positions leads to instability [54]. This instability unfolds as a uniform shear along $[\bar{1}\bar{1}0]$ direction accompanied by shuffling in the atomic planes resulting in a complex modulated structure below phase-transformation temperature. In order to accommodate the stressed produced due to these Bain transformations, secondary invariant lattice strains involving the same shear system resulting in a twinned microstructure [55]. The lower-symmetry close-packed martensite phase is known to exist in 2, 5, 7, 10 – layered structures depending on the composition and heat treatment [25, 48, 56].

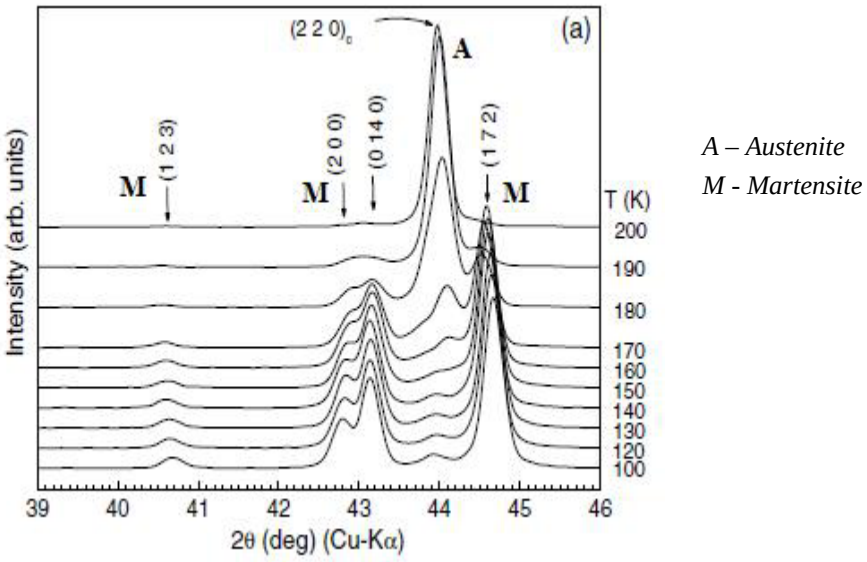

FIG. 1.14 XRD spectrum showing phase transformation from martensite to austenite [57].

For austenite which has an $Fm\bar{3}m$ FCC structure is usually characterized by a high intensity (220) peak. Due to modulated nature, martensite structure is characterized by twin peaks indicating the twin modulated structure. A clear change in crystal structure is observed before and after phase transformation. Figure 1.14 shows the change in XRD spectrum across the phase transformation zone.

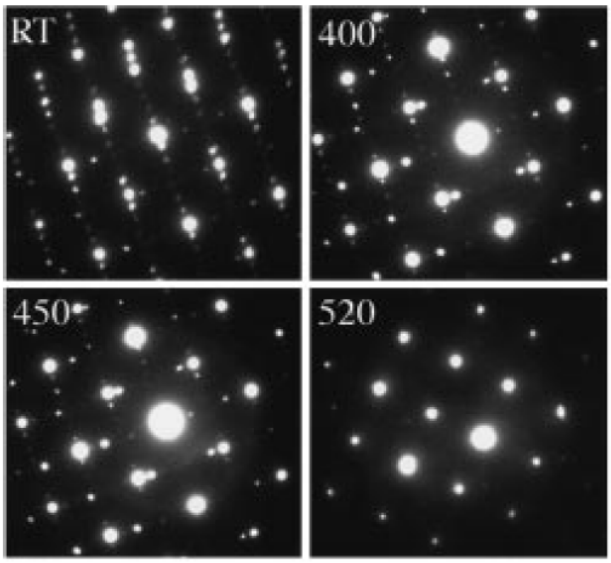

Temperature indicated in °C

FIG. 1.15 In-situ TEM heating experiment on Ni-Mn-Ga thin film showing 7M→ Cubic austenite transition at T_A ~520°C [44].

Change in microstructure can also be manifested using selected area diffraction (SAD) patterns (SADP) of martensite grains during in-situ TEM experiment. Figure 1.15 shows one such in-situ TEM heating experiment on ion-beam sputtered thin films reported by Ahn et al. [44].

1.5.2 Thermal properties

Phase transformation in shape memory alloys is a diffusionless phenomenon. The transformation is characterized by a release or absorption of heat and is not dependent on the rate of heating/cooling. Differential scanning calorimetry (DSC) is used to study phase transformation temperatures, precipitation behavior and grain size effect on phase transformation.

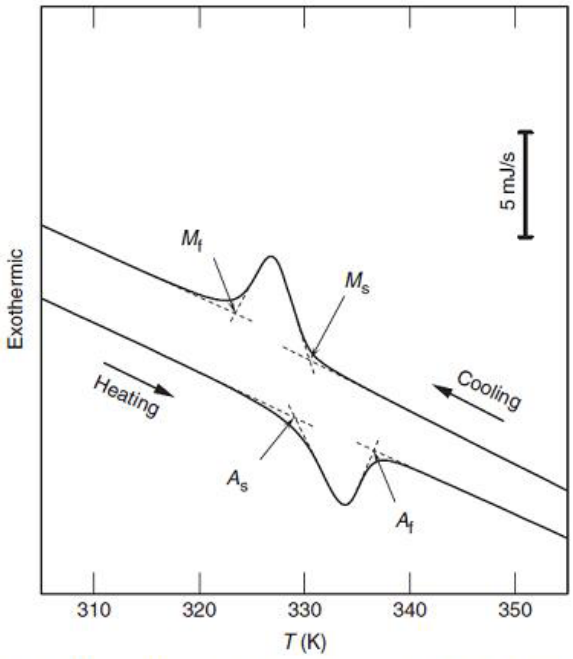

FIG. 1.16 DSC curves showing phase transformation [50].

The austenite → martensite transformation is exothermic characterized by a heat release peak, whereas the martensite → austenite peak is an endothermic peak. Figure 1.16 shows a DSC chart of Ni-Mn-Ga thin film. The martensite and austenite start -

finish temperatures indicated as M_s, M_f, A_s, A_f respectively are the intersection of the tangents at the onset or end of the respective features.

1.5.3 Electrical resistivity

Martensite with its complex modulated structure is observed to have a higher resistivity compared to austenite. There could be two reasons for an increase in resistivity for martensite. a) Differentially oriented twins can acts as scattering centers for the conduction electrons b) The number of charge carriers decrease during transformation [58].

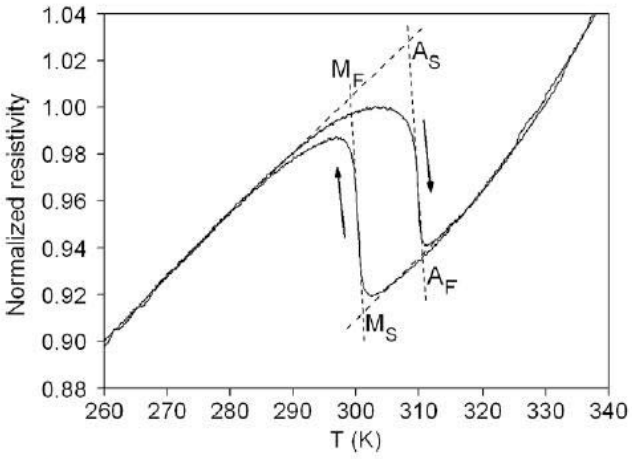

FIG. 1.17 Resistivity vs. temperature curve during phase transformation [53].

As temperature is increased, a linear increase in resistivity is observed owing to thermal scattering, at phase transformation temperature, a sharp decrease in resistivity is observed upto A_f. The resistivity linearly increases thereafter. During cooling, a decrease

in resistivity is observed until phase transformation sets in. At the martensite start temperature M_s, resistivity increases rapidly upto M_f. Thereafter an expected linear decrease with temperature is observed [53]. In the event of inter-martensitic transformations, a similar effect with a change in slope is observed owing to a different martensite structure and hence a different scattering effect [52].

1.5.4 Magnetic properties

In MSMA's like Ni-Mn-Ga phase transformation is closely related to magnetic properties of the material due to the presence of magnetocaloric effect [12]. Hence the change in crystal structure observed during phase transformation is accompanied by a change in magnetic behavior of the material. A sharp change in anisotropy, susceptibility and over all magnetization in the region of phase transformation has been reported in the material [6, 12, 51, 59].

Figure 1.18 shows temperature dependence of low-field AC *magnetic susceptibility* of $Ni_{48.8}Mn_{29.7}Ga_{21.5}$ alloy during heating and cooling cycles. During cooling, an abrupt increase in susceptibility is observed at T_c, indicating the Curie point where paramagnetic austenite transforms into a ferromagnetic state. A decrease in susceptibility at C-7M, 7M-T correspond to phase transformation from cubic $L2_1$ to 7-layered martensite phase, 7M to non-modulated martensite phase respectively. In the heating cycle all the transitions occur in reverse order with some temperature hysteresis.

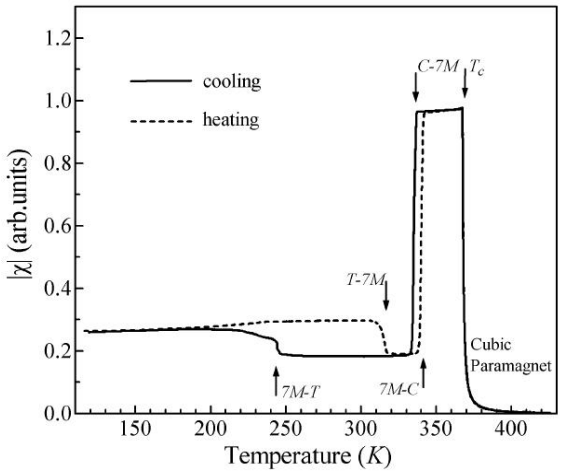

C – ferromagnetic cubic phase

7M – 7-layered martensite phase

T – NM martensite phase

T_c – Curie point

FIG. 1.18 Temperature dependence of low-field AC magnetic susceptibility of Ni-Mn-Ga alloy [59].

After martensitic phase transformation, generally layered martensite structures with multiple variants are formed. These multiple variants give rise to magnetic anisotropy in the sample. With appropriate mechanical treatment a single-variant sample can be prepared. Figure 1.19 shows magnetization measurements on three single variant samples (with 7- layered martensite structure) along the [100], [010], [001] axes [6]. The M (H) magnetization curves indicate that the axis of easiest magnetization is the c-axis while the longest a-axis is the axis of hard magnetization.

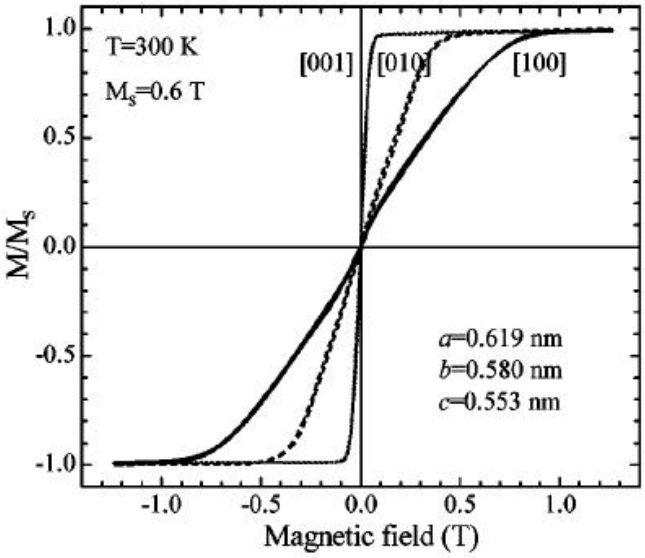

M_s – Saturation Magnetization

M – Magnetization

T – Temperature

FIG. 1.19 Magnetization curves along different axes of 7-layered martensite phase [6].

1.5.5 Stress - Strain

In Ni-Mn-Ga samples that have been subjected to order heat treatment, martensitic phase transformation is accompanied by a shape change. This change in shape can be measured as strain in the sample across phase transformation zone. In specimen that are constrain aged or "trained" a change in phase from cubic austenite to highly twinned, distorted martensite structure is accompanied by a change in volume resulting in macroscopic stress.

Figure 1.20 shows a temperature – strain curve for order-heat treated Ni-Mn-Ga thin films. Near phase transformation temperature, a sharp increase in *strain* due to formation of twinned martensite is observed [25]. This shape change is very sensitive to heat treatment. A considerable difference in hysteresis is observed for different

conditions of heat treatment. Generally a longer heat treatment yields better homogeneity and a narrower hysteresis [25].

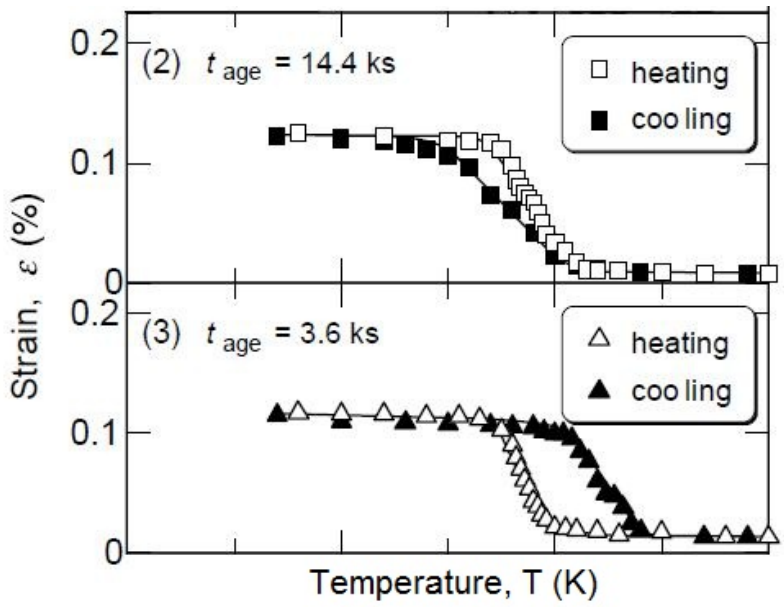

FIG. 1.20 Temperature – Strain curves for Ni-Mn-Ga thin films [25].

1.5.6 Morphology

Techniques like X-ray diffraction, magnetization and DSC that probe the complete volume of a bulk or thin film specimen do not give interface properties at micro-scale. Even in cross section TEM studies specimen preparation could alter the existing microstructure in a sample. Twinned interfaces in martensite can be studied with polarized light microscopy, scanning electron microscopy (SEM) and atomic force microscopy (AFM) [37].

Figure 1.21 shows martensite microstructure in a thin film sample using the mentioned techniques. Polarized light microscopy reveals micrometer wide macroscopic twin variants. Heating above transformation temperature resulted in a loss of contrast. In other words the martensite variants formed below transition temperature transforms to austenite erasing the contrast due to differently oriented martensite variants.

Further examination of these contrast bands under SEM revealed wavy features of 50 - 100nm width indicating microscopic twinning inside the macroscopic twins. AFM measurements confirm the presence of twins with a thickness of about 50 nm on the sample.

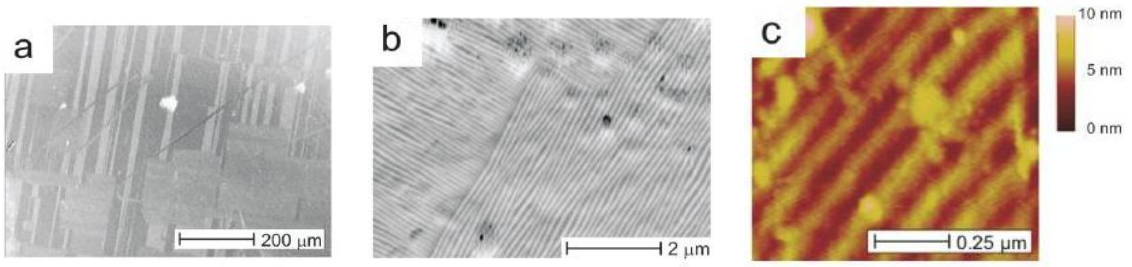

FIG. 1.21 Morphology of twinned martensite surface as seen in (a) Polarized light microscopy (b) Scanning electron microscopy (c) Atomic force microscopy [37].

AFM as a local probe of topography can measure lateral microstructure of a surface at small scale distances. Lateral microstructure can be used as complimentary information to XRD. In-situ studies of topography can be used to manifest the change in topography during a phase transformation cycle.

The martensite microstructure is characterized by high density twins. Martensite variants are known to exist in parallel bands with nearly orthogonally oriented to each other. Figure 1.22 shows topography micrographs of a single crystal Ni-Mn-Ga thin film during a complete temperature cycle.

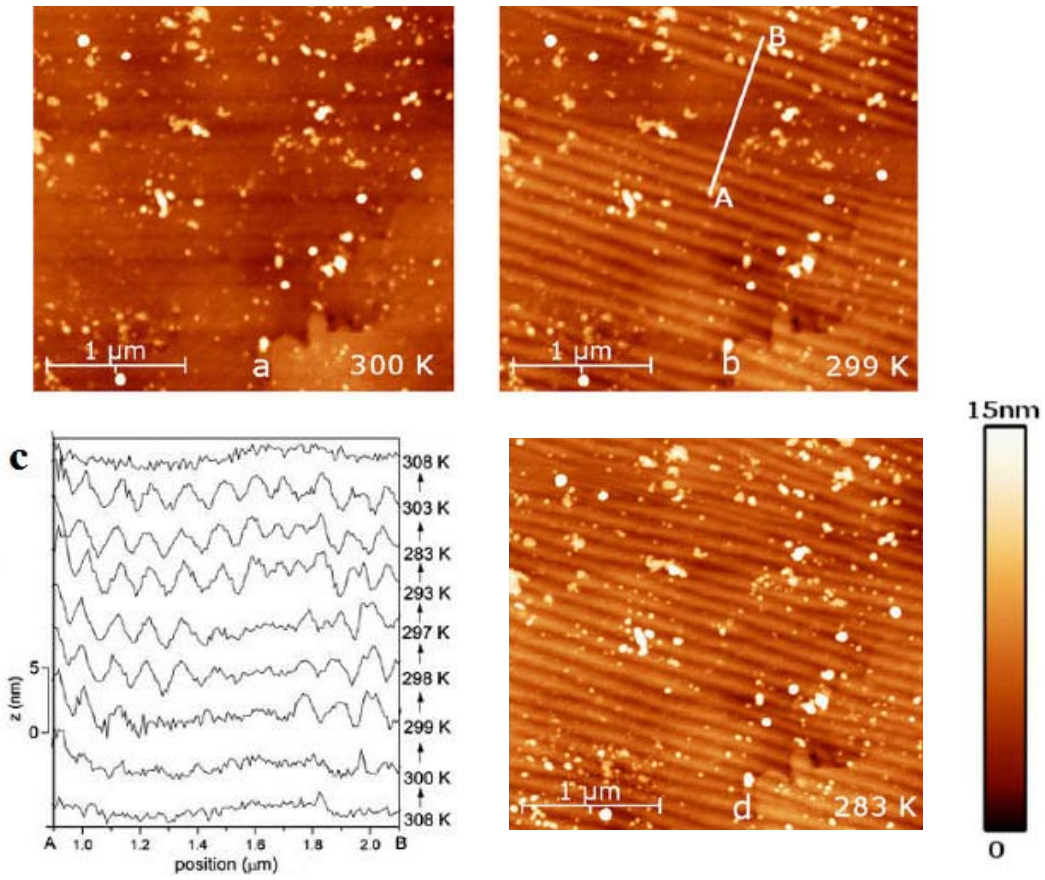

FIG. 1.22 Micrographs of AFM surface topology of Ni-Mn-Ga films during transformation [53].

1.6 COMPOSITIONAL DEPENDENCE OF PROPERTIES

Composition is one of the key parameters in tailoring NiMnGa properties. Several physical properties of Heusler alloy system are very sensitive to composition [2]. A strong compositional dependence of many properties of key to ferromagnetic shape memory effect like saturation Magnetization (M_s), martensite transformation temperature (T_{mart}), Curie Temperature (T_c), magneto crystalline Anisotropy (K_u), electrical resistivity, entropy have been observed [23, 60].

With the addition of Ni to replace Mn/Ga or with the addition of Mn to replace Ga an increase in the transformation temperature along with a decrease in Curie temperature is observed. Chernenko et al. correlated the change in properties with electron concentration of Ni-Mn-Ga alloy compositions [23]. It was deduced that the transformation temperature and Curie temperature had a linear relationship with the valence electron concentration. Increase in valence electron concentration was found to induce instability towards close-packed martensitic phases thereby influencing the first order character of martensitic transformation. Valence electron concentration indicated by e/a, is defined as the number of valence electrons per atom. Assuming that the valence electrons of the elements are [23],

Ni: 10 ($+3d^8\ 4s^2$)

Mn: 7 ($+3d^5 4s^2$)

Ga: 3 ($+ 4s^2\ 4p^1$)

$$e/a = \frac{10\,(\%Ni) + 7\,(\%Mn) + 3\,(\%Ga)}{(\%Ni + \%Mn + \%Ga)}$$

Jin et al. studied the variation in transformation temperatures in order to develop an empirical formula to fit the behavior of Ni-Mn-Ga system [60]. Figure 1.23 shows a linear regression for Martensitic transformation temperature T_{mart}. The literature data was fitted as $T_{mart} = 702.5\ (e/a) - 5067$.

The error for linear fit in Figure 1.23 shows a large standard deviation of 44.7 K and a maximum error of 140.2K were observed in the transformation temperatures. This suggests that the transformation temperature is also sensitive to factors other than valence electron concentration. This observation is iterated by studies that show the influence of processing parameters and microstructure on transformation temperature [36].

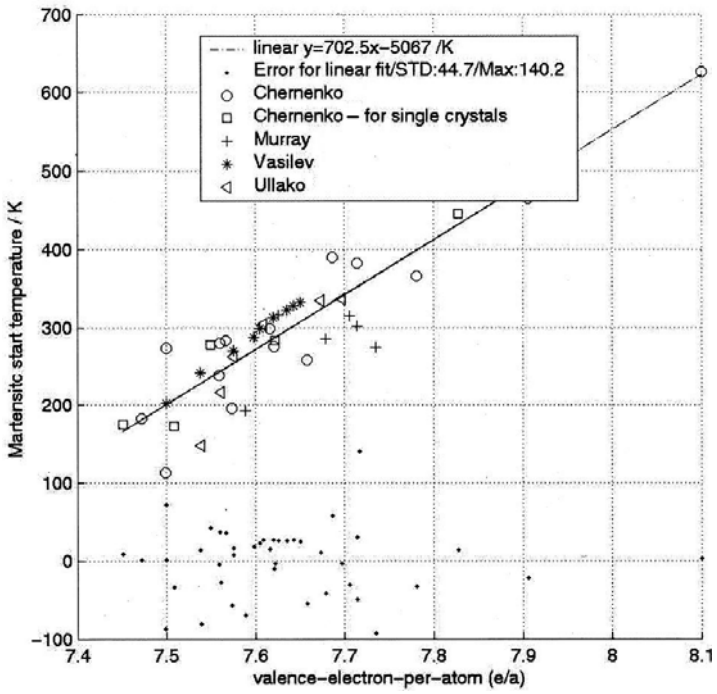

FIG. 1.23 Relationship between Martensite transformation temperature and e/a [60].

The temperature below which ferromagnetic ordering is seen in magnetic materials is called a Curie temperature (T_c). T_c follows an inverse trend with increasing valence concentration. Increasing valence electron concentration results in a lower Curie temperature (T_c). Figure 1.24 shows an empirical curve compiled by Chernenko et al. [23]. Linear and Inverse proportionality of T_{mart} and T_c with e/a can be clearly seen from the data.

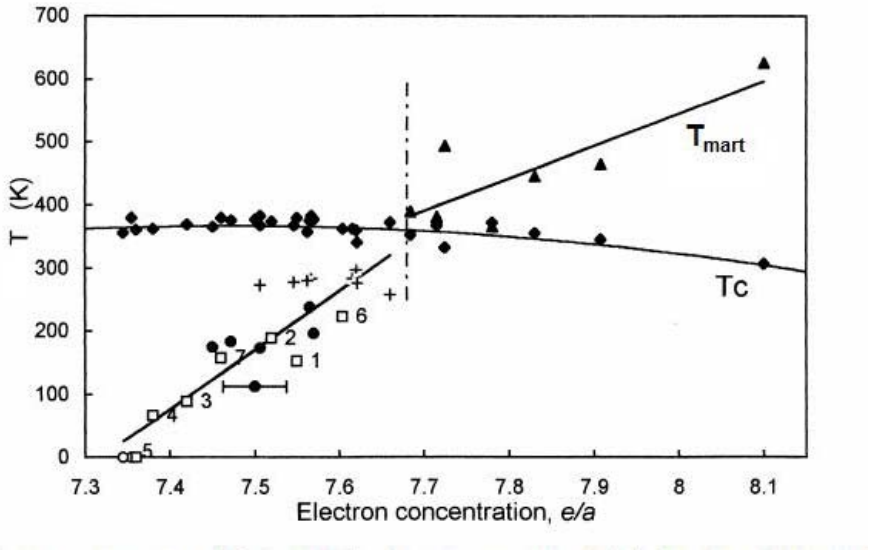

FIG. 1.24 Empirical curves showing compositional dependence of T_c and T_{mart} with e/a [23].

Stoichiometric Ni_2MnGa alloy undergoes phase transformation around 200K, Curie temperature at 376K [16] with a saturation magnetization of ~65emu/g. Though this composition has the highest saturation magnetization, it is not very useful for ferromagnetic shape memory effect. In order to observe ferromagnetic shape memory effect (FSME) or MFIR, the phase transformation temperature of an alloy has to be

around room temperature while still below the Curie temperature. A high value of saturation magnetization (M_s) is desired since M_s is directly related to the magnetic pressure driving twin boundary motion given by $2M_sH$.

Curve fitting of experimental saturation magnetization values by Jin et al. shows a peak at e/a value of 7.5. Stoichiometric Ni_2MnGa shows a maximum value of saturation magnetization of ~65emu/g. For e/a >7.5 M_s is observed to decrease with increasing e/a. Several studies have indicated similar trend in M_s [61].

Enkovaara et al. tried to explain this anomaly using the first principles calculations within density-functional theory. They showed that extra Mn atoms added to stoichiometric composition align anti-ferromagnetically to other moments. This leads to a dependence of magnetization on composition [62].

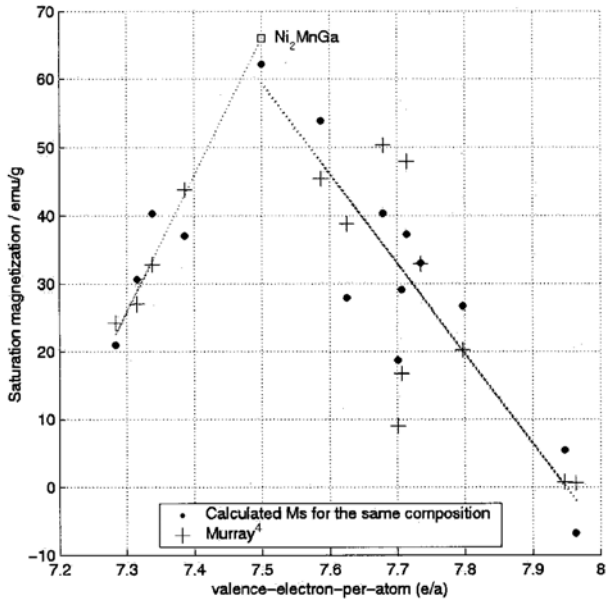

FIG. 1.25 Compositional dependence of saturation magnetization (M_s) with e/a [60].

In addition to physical properties, the microstructure of austenite and martensite phases in NiMnGa is known to be very sensitive to composition. The crystal structure of the austenite is $L2_1$ below 600°C [24] over the whole range of composition with only an increase in lattice parameter with increasing Ni concentration. The lattice parameter of stoichiometric Ni_2MnGa is 5.825Å [63]. Alloys with austenite lattice parameters as high as 5.97 Å have been reported in high temperature alloy compositions [64].

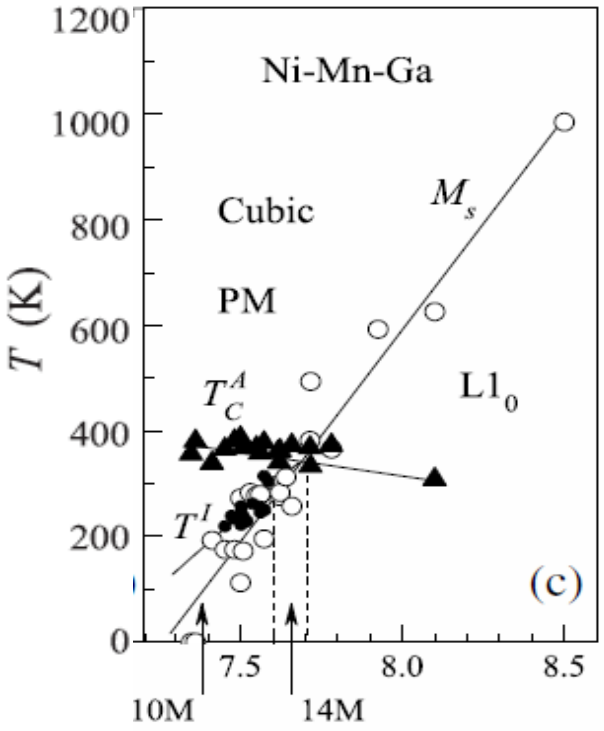

M_s – Martensite start temperature

T – Temperature

FIG. 1.26 Compositional dependence of martensitic structure [2].

At very low concentrations of 'Ga' the alloy transforms to tetragonal $L1_0$ since it is the martensite structure of the ground state $Ni_{50}Mn_{50}$ [2]. Stoichiometric Ni_2MnGa has

been reported to transform to 10M below martensitic transformation temperature [63]. In-between these compositions, the structure of the martensite phase depends largely on the composition. Martensite structure is also found to be sensitive to factors like deposition method, annealing conditions etc. [25, 48]. With increasing e/a, martensite structure evolves as 10M → 14M → $L1_0$ [2].

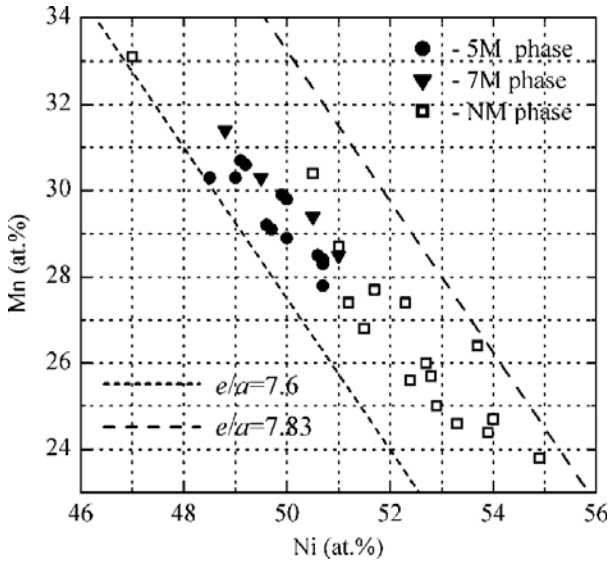

FIG. 1.27 Martensite structures observed in alloys with different Ni/Mn ratio for the same transformation temperature [56].

It is worth noting that the martensite structure is also influenced by the ratio of Ni and Mn. Lanska et al. showed that in small range of e/a, 10M, 14M and $L1_0$ structures can be obtained in martensites by varying the ratio of Ni and Mn (5M, 7M structures correspond to 10M and 14M structures in new system) [56].

2. EXPERIMENTAL METHODS

During phase transformation, shape memory materials undergo a number of changes in their mechanical and physical properties, including hardness, magnetization and electrical resistivity. Hence, a combination of several techniques can be used to detect phase transformation by probing the variation of these properties. In this section the techniques used to deposit and characterize Ni-Mn-Ga thin films are described.

2.1 THIN FILM DEPOSITION

The process of laying or applying films with thickness ranging from nanometers to a few microns, onto a surface called a substrate is called thin film deposition. Several deposition processes have been developed to deposit thin films. They can be grouped under two basic categories called physical and chemical vapor deposition processes.

Depending on the goal of deposition, such as to achieve certain level of residual stress, adhesion, stoichiometry, film density, grain size, impurity etc. one or multiple deposition processes can be selected.

In thin film community the term epitaxy is frequently used referring to processes used to deposit epitaxial films on suitable substrates. Epitaxial films are referred to as thin films with single-crystal like microstructure and typically are grown on single crystal substrates [65].

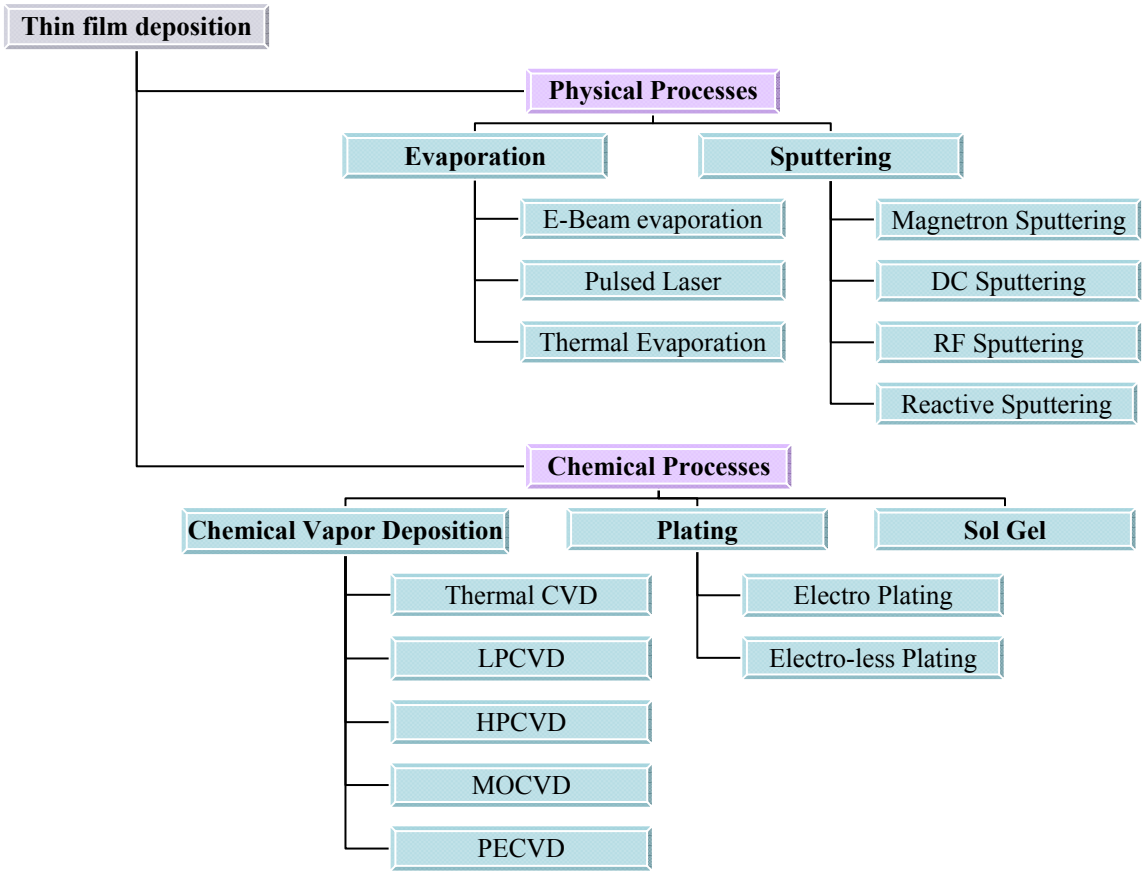

FIG. 2.1 Thin film deposition methods.

2.1.1 Magnetron sputtering

Sputtering is a physical vapor deposition method where ions accelerated under a high voltage bombard the target surface to eject (sputter) atoms. The sputtered target atoms are directed towards the substrate surface by an electric bias, and eventually producing a thin film on substrate. Inert gases like Argon, Neon are usually used as the sputter gas. The material to be deposited is termed as target while the subject that collects the films is called a substrate. A negative voltage in the order of a few hundred

volts is typically applied to the target while the substrate is grounded. Positively charged inert ions accelerate at very high velocities towards the target resulting in a collision cascade. Incoming ions with energy above a critical value result in ejection or sputter of atoms from the target surface. Target atoms, or sometimes cluster of atoms that are usually neutral or negatively charged accelerate towards the substrate and form a thin film.

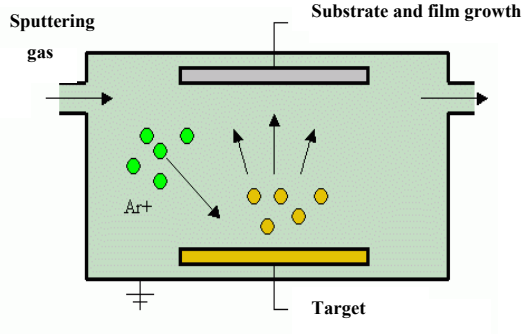

FIG. 2.2 Schematic of sputtering process.

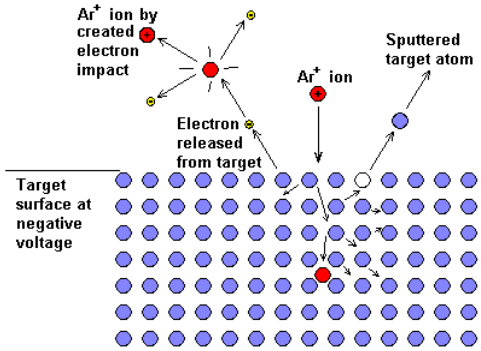

FIG. 2.3 Schematic of ion collision cascade in target.

DC sputtering is used for conductors or materials that can be sputtered easily, while RF Sputtering is used for insulators and semiconductors which are hard to deposit using DC sputtering. Target is a solid form of material usually 99.95% pure that has to be sputtered to deposit the thin film. Inert gas called sputter gas is picked such that the mass of the sputtering gas is comparable with the mass of the target atom to ensure efficient momentum transfer. Hence Neon is used for sputtering light atoms while Krypton or Xenon is used for heavy atoms. For sputtering most of the commonly used metals and semiconductors, Argon or Neon is used as sputtering gas. In the present case,

for depositing Ni-Mn-Ga alloy thin films, Argon was used as the sputter gas and 3-inch diameter Ni-Mn-Ga alloy discs usually 1.25" in thickness are used as targets.

When a magnetic field produced by a permanent magnet referred is used to *increase the path of the electrons* and hence the number of ionized inert atoms, the process is called **Magnetron Sputtering.** More ionized inert atoms in turn result in increased sputtering and hence enhanced deposition rates. Magnetron Sputtering is a flexible technique that can deposit a wide variety of materials – metals, alloys, insulators, semiconductors etc.

Sputter equipment consists of a main vacuum chamber, load lock, substrate holder, vacuum pumps, electric setup, cooling system, sputter gas setup. Sputtering is done under high vacuum conditions to avoid contamination of film. In a typical deposition, base pressure is pumped down to 10^{-6} - 10^{-9} Torr using turbo, cryo pumps. A load lock is pumped down to a vacuum of 10^{-5} Torr for transferring the substrate without breaking the vacuum of main chamber. A substrate with a clean surface is attached to the substrate holder that is fixed at the confocal centre from the target. Sputtering gas is released into the chamber increasing the background pressure to 10^{-3} Torr. On applying a very high negative voltage to the cathode (target), plasma is generated. The Argon atoms in the plasma are ionized and accelerate towards the target at very high velocities due to the bias. Sputtered target atoms with enough velocity get deposited on the substrate surface.

The residual kinetic energy in target atoms is converted to thermal energy which increases their mobility and facilitates surface diffusion. Hence a continuous chain of atoms are formed resulting in a better quality film.

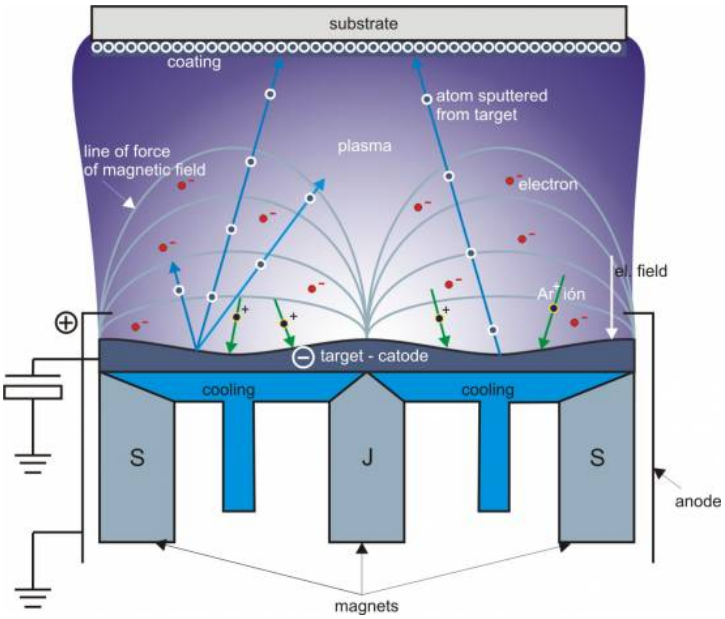

FIG. 2.4 Schematic of magnetron sputtering system.

Magnetron sputtering process has a number of advantages over other sputtering processes. Due to magnetic fields and higher deposition rates, plasma can be sustained at lower Ar pressures and hence resulting in lower level of impurities (Ar). Since the sputtering mechanism is not a thermal evaporation process, even the material with highest melting point can be deposited at room temperature. Sputtered alloy films have a composition close to their target composition. The slight difference is due to difference

in sputter yields of different materials. Sputtering technique produces films with a better adhesion than evaporated films.

Substrate heating can be done by attaching a heater to the sample holder for epitaxial depositions. Thermal energy imparted to the depositing atoms increases the mobility of adatoms forming thin films that have a near perfect atomic stacking during deposition.

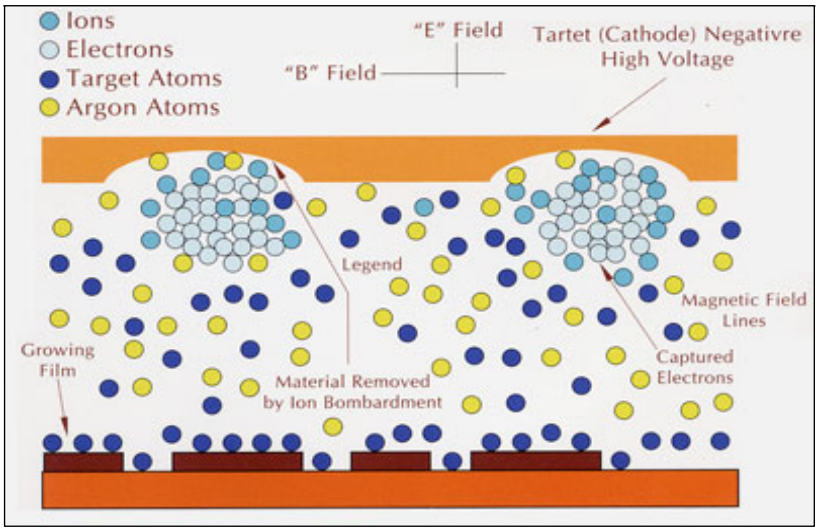

FIG. 2.5 Distribution of ions during sputtering.

Circular magnetron guns are the most commonly used configuration. In these guns, circular permanent magnets are used as magnetrons. This results in a circular 'race course' shaped track where electrons and plasma are concentrated. The target depletion rate will be the highest in this area. The distribution of ions in a cross-section of magnetron sputtering chamber is shown in the Figure 2.5. The two inverted cups in the

target indicate the ‘race course’. It can be noticed that the density of ions-electrons is maximum in this area. Figure 2.6 and 2.7 show the parts of a circular 2-inch magnetron and race course track

FIG. 2.6 Race course track and plasma during sputtering.

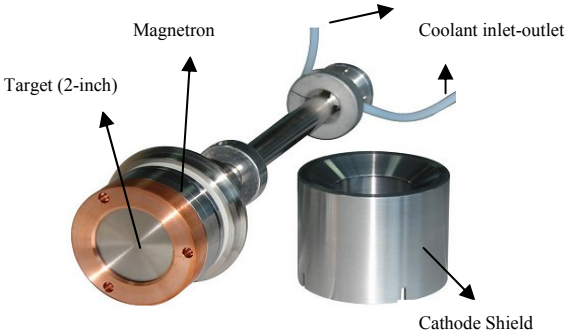

FIG. 2.7 2- inch magnetron gun.

The target is subjected to tremendous heating due to the temperature of the plasma and kinetic energy of the colliding ions. It is very important to cool the target efficiently, especially if deposition of alloys is concerned. Increase in target temperature varies the deposition rates and composition of the deposited film. Films deposited from heated targets have undesirable change in physical properties due to a difference in the energy of the incoming adatoms. Coolant, usually water is continuously circulated to maintain the target at room temperature. Copper backing plate is commonly used to improve thermal contact between coolant and the target. Backing plate also ensures a uniform temperature distribution across the target surface.

In this thesis, a custom-built multi source magnetron sputtering system has been used for thin film deposition. The magnetron sputtering system has 4 sputtering sources arranged in confocal symmetry. The system is capable of automatic multilayer deposition, co-sputtering or deposition with a seed layer or cap layer of a different material. Two sputter sources have a high energy magnetron that can sputter magnetic materials like Ni-Mn-Ga.

The system is capable of DC and RF sputtering. The main chamber can be pumped down to ultra high vacuum using cryo and turbo pumps. Substrates are loaded through a load lock chamber that is connected to the main chamber. The load lock helps in maintaining good vacuum in the main chamber at all times. Ultra high purity Ar is used as the sputtering gas. Sputter gas is injected close to the sputter guns as opposed to releasing it directly into the chamber. This enables deposition at low base pressures. In order to obtain good film uniformity across the substrate, the sample stage rotates during deposition. The temperature of the targets is maintained by circulating chilled water maintained around 15˚C at all times during deposition.

2.2 COMPOSITION

Accurate measurement of the composition of deposited samples is one of the primary steps in characterization and prediction of their phase transformation behavior. The phase transformation behavior of Ni-Mn-Ga alloy is very sensitive to its composition. For instance it has been shown that 0.1 unit increase in e/a value increases the predicted martensite start temperature by about 80 K [2]. Hence it is necessary to use

a compositional analysis technique, such as wavelength dispersive spectroscopy (WDS) that is very accurate.

2.2.1 Wavelength dispersive spectroscopy

When a high energy electron beam (5-50 kV) interacts with matter, it results in the generation of a number of electrons (Auger electrons, secondary electrons, back scattered electrons), emitted X-rays along with cathodoluminescence, heat and absorbed electrons. Of these, the emitted X-rays which carry the signature of the elements in the sample are used to generate a qualitative analysis of the specimen composition.

A spectrometer uses characteristic x-rays generated by individual elements to enable quantitative chemical analysis. Compositional maps can be generated by rastering the beam across the sample. Wavelength dispersive spectroscopy (WDS) is preferred over the other techniques like energy dispersive spectroscopy (EDS) because of its ability to obtain precise chemical analysis of species and high spatial peak resolution. It is a non-destructive technique with spot sizes as low as a few micrometers and detects elements with atomic numbers 4 and above.

A WDS spectrometer often comes with more than one spectrometer mounted in sequence making it easy for testing alloys, minerals etc. In this thesis, *Cameca SX40 electron microprobe* has been used for the compositional analysis. The setup consists of an evacuated chamber with electron beam generated through an electron column typically with a potential difference of 15-20 kV resulting in emitted x-rays. The

generated X-rays are selected using two analytical crystals with specific lattice spacing's.

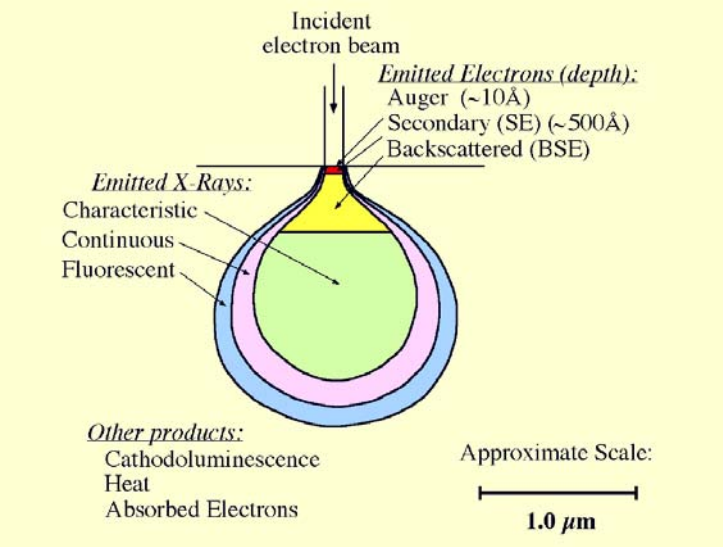

FIG. 2.8 Incident electron beam – resulting emissions.

When the X-rays encounter the analytical crystal at a specific angle θ, only those X-rays that satisfy Bragg's Law are reflected and a single wavelength is passed on to the detector. By changing the position of the analytical crystal w.r.t. the sample the wavelength of the reflected X-rays can be varied. 4 spectrometer detectors with two analyzing crystals each can be used to acquire 8 elements measurements from the specimen by cycling through each crystal during analysis.

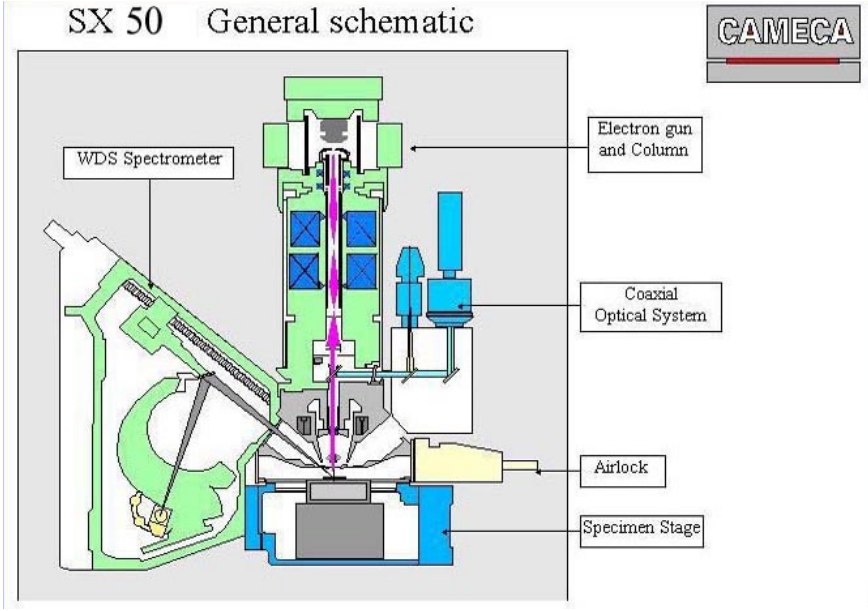

FIG. 2.9 Schematic of Cameca SX60 electron probe.

X-rays of specific wavelength from analytical crystals are passed onto the X-ray detector for all wavelengths of interest. The motion of the analytical crystal and spectrometer is maintained such that both remain on the Rowland circle as shown in Figure 2.10. The setup follows Johansson geometry, so that all of the points of reflection lie on the Rowland circle, which maximized the collection efficiency of the spectrometer. The detectors on the spectrometers are equipped with counters which "count" the amount of a particular X-ray emitted. These values are compared to the standard characterized known values of the elements of interest. The X-ray intensities should also be corrected for matrix effects associated with atomic number (Z), absorption (A) and fluorescence (F). A computer program is used to take the raw counting rates of each element and apply the ZAF correction to display the quantitative weight percentage of elements inside the specimen.

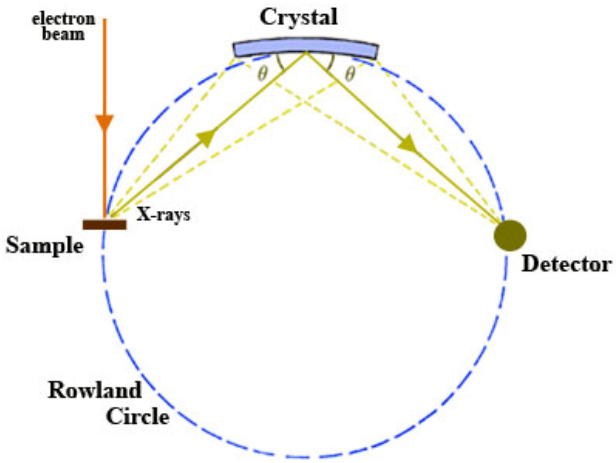

FIG. 2.10 Rowland circle setup of WDS.

Cameca SX60microprobe is equipped with 4 spectrometers each with two diffracting crystals each: TAP (2), PET (2), LIF (2) and 60 and 200A dummy crystals (PC1 and PC3). Rapid automated qualitative as well as quantitative capabilities with on-screen display of 4 simultaneous spectrometers scans is possible. The machine is fully automated with unattended multiple spot analysis capabilities.

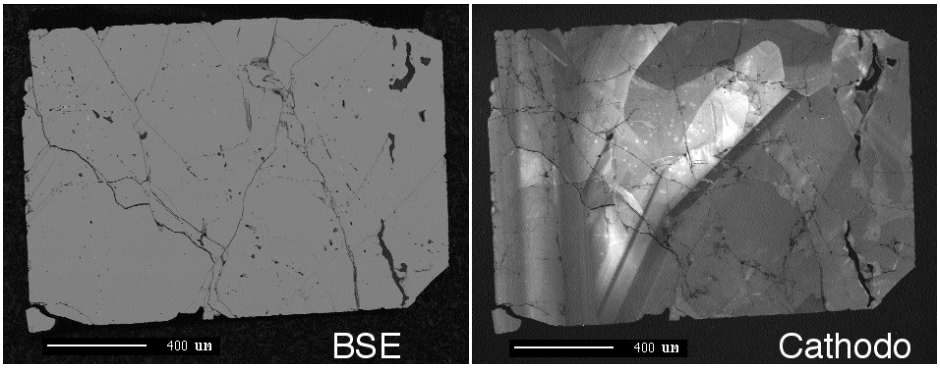

FIG. 2.11 BSE – Cathodoluminescence picture of a Zircon crystal.

Back scattered electrons and cathodoluminiscence reflected from the sample. Together, they offer a good medium to pick data points for analyzing conditions like phase segregation. Figure 2.11 shows both views of a specimen.

2.3 STRUCTURE

For studying shape memory materials that undergo a diffusionless phase transformation characterized by a change in geometry of the unit cell, crystal structure is a fundamental and important tool to determine the phase of the material at a given condition. Moreover, in materials like NiMnGa alloys martensite phase exists in more than one form like NM, 10M, 14M [27]. In other words, determination of crystal structure is indispensible in characterizing shape memory alloys. Two powerful and commonly used techniques for determining crystal structure will be discussed below.

2.3.1 X- ray diffraction

X ray diffraction is governed by the fact that x-rays have wavelengths compared to that of atomic distances and the structure of crystalline materials are regularly repeating. The wavelength of X-rays is a few Angstroms, which is comparable to the atomic distances in crystalline materials.

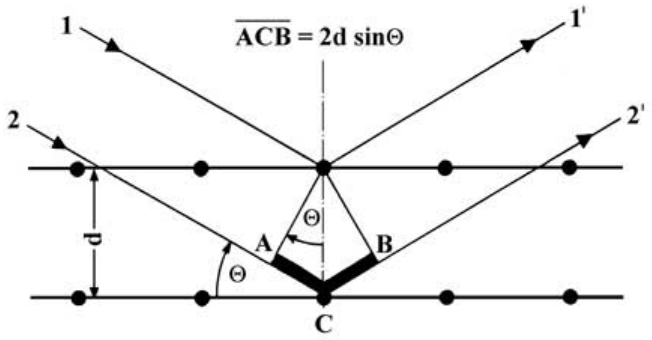

FIG. 2.12 Schematic of parallel rays reflected across atomic planes.

This enables atoms to interact with incident x-rays which get diffracted on contact. The X-rays diffracted from an array of equally spaced atomic planes constructively interfere to give a diffracted beam.

In 1912, W. L. Bragg recognized this predictable relationship and deduced a law, named after him as Bragg's Law. Bragg's law states that:

$$\mathbf{n\lambda = 2d \sin\theta}$$

where,

d – distance between atomic planes (in A˚)

λ – wavelength of the incident X-rays (in A˚)

θ – angle of diffraction (in deg.)

n – integer (1,2,3….)

DIFFRACTOMETER

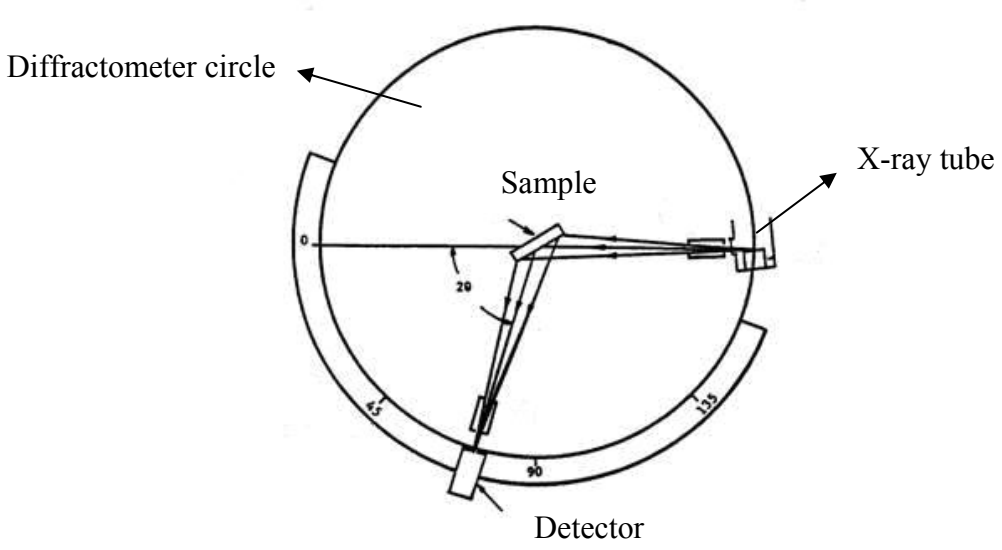

FIG. 2.13 Schematic of X-ray diffractometer.

Diffractometer is used to measure the diffraction spectrum of a crystal structure. It consists of three main parts, X-ray tube, Diffractometer circle and Detector/counter. Parallel x-ray beams are emitted onto the crystal surface and get diffracted by the atomic planes in the crystal. Some of the diffracted beams are detected and recorded w.r.t the angle (2θ). The detector which is in the same plane as the sample, rotates at a constant rate along the diffractometer circle recording the diffracted x-ray intensities as a function of 2θ. 2θ vs. recorded intensities plot gives the dominant crystal planes which translate into crystal structure.

In this study, a *Bruker AXS D8 Advanced Bragg Brentano X-Ray Diffractometer* with Cu – K_α radiation is used for X-ray diffraction analysis of freestanding and substrate constrained thin films at room temperature.

2.3.2 Transmission electron microscopy

A transmission electron microscope works on the same principle as optical microscope. As the name indicates, electrons with a much smaller wavelength are used instead of light. This higher resolution enables the microscope to reveal details in the order of a few angstroms (10^{-10} m). Transmission electron microscopy (TEM) is widely used in medical, biological and materials sciences to examine atomic and cell structures in minute detail.

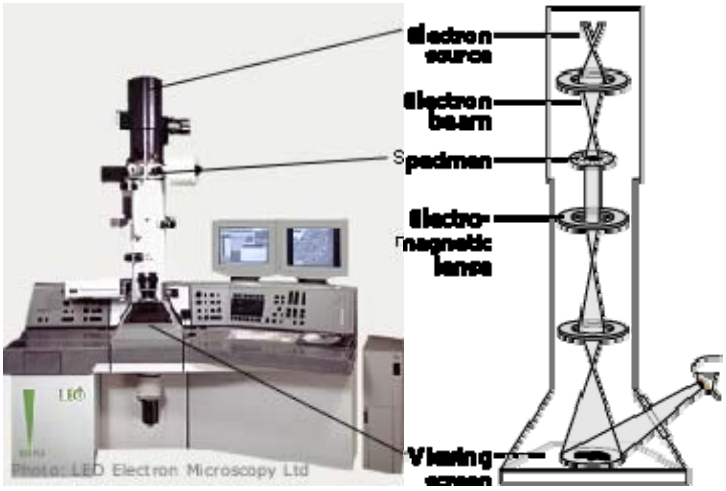

FIG. 2.14 Schematic of transmission electron microscope (TEM).

The setup consists of an electron source. The emitted electron beam is focused using electromagnetic lenses. Focused beam is passed through a carefully prepared specimen which is electron transparent. The electron beam interacts with the sample to give a fingerprint of its crystal structure. The denser areas scatter the electrons while the

thinner areas are transparent. The resulting electron beam passes through a row of lens before it is caught on a fluorescent screen. The image which is a shadow of the specimen can be examined directly or photographed with a camera.

JOEL JEM-2010 Transmission Electron Microscope with 200kV accelerating voltage and LaB_6 filament has been used for TEM analysis. The Transmission electron microscope has a 0.23nm point resolution and is attached with a *Gatan SC1000 ORIUS* CCD camera which can capture image with 4008 × 2672 pixel resolution.

For studying grain size evolution or examining the change in surface texture during transformation, in-situ TEM technique can be used. The *JEOL JEM-2010* apparatus supports an **in-situ heating** stage that allows upto a temperature of 1200°C. A double-tilt holder with ± 30° tilt can be used to take selected area electron diffraction (SAED) patterns of individual grains for a more detailed analysis of crystal structure evolution during phase transformation. Nano beam diffraction (NBD) can collect diffraction pattern a few 1nm feature allowing precise crystal structure analysis.

The most important step in TEM imaging is sample preparation. Prescribed sample preparation techniques for almost any material are available. TEM samples can be broadly divided into two types - Plane view and Cross section. Details of grinding and polishing are fundamental and will not be discussed.

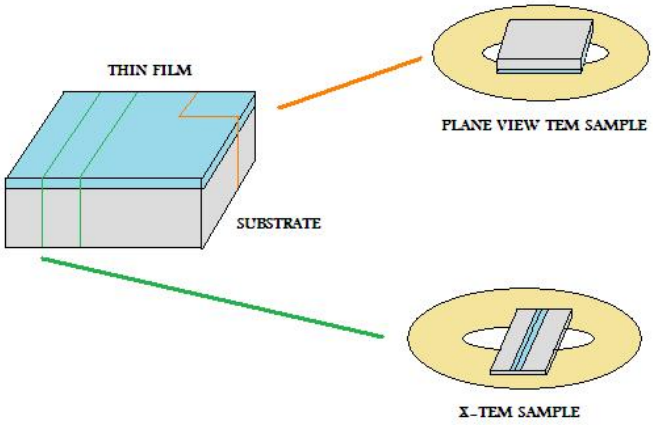

FIG. 2.15 Plane view – X TEM samples.

Ion-milling which involves sputtering using high velocity ions is used to obtain electron transparent specimen. *Gatan Model 691 Precision Ion polishing system* with Ar-ion beams has been used. Two Ar-ion beams accelerated at high velocities are impinged onto the sample to thin it down to electron transparency. Usually 3.5KeV potential with 3rpm sample rotation and 5˚ angle of incident ion beams is used.

2.4 MECHANICAL PROPERTIES

Thin films for future MEMS devices need to have superior mechanical properties. Hardness, Elastic modulus, film stress are few properties that have to be characterized.

2.4.1 Hardness – Nano-indentation technique

Thin films have thickness usually below a few microns. Typical hardness indenters would penetrate through the thickness of the film onto the substrate giving a

convoluted value of substrate and film. Hence nano-indenters with very small loads and indent sizes in nanometers are used for testing thin films.

Fisherscope HM2000 XYp fully automatic, pre-programmable hardness tester has been used to measure the Hardness and Elastic Modulus of thin films. The hardness tester uses a Vickers indenter with a load range of 0.4 – 2000mN, a load resolution of less than 40μN and a penetration depth resolution of $\leq$ 100pm.

The setup of a nano-indenter consists of a diamond indenter tip, a controlled sample stage, capacitance displacement stage for measuring displacement during indentation, springs, magnet and coil. The thin film on substrate is placed on the sample stage. An optical microscope attached to the indenter is used to examine surface of specimens. Indentation spots are selected using the pre programmable option and optical microscope attached over the sample stage.

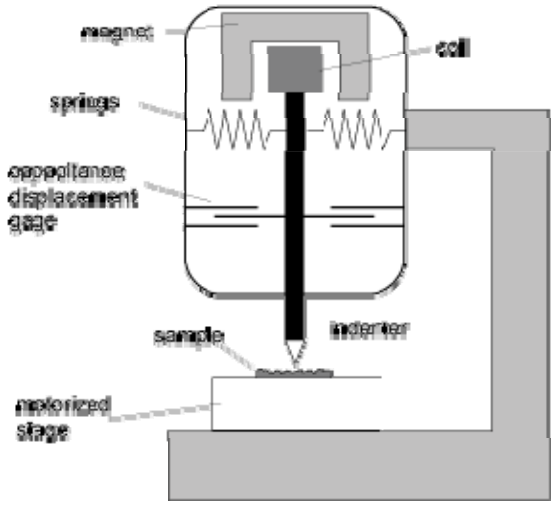

FIG. 2.16 Schematic of nano-indenter.

Usually 9 - 16 or more indents are taken at each depth to calculate the hardness and elastic modulus of the material.

An indent cycle consists of the following steps:

a) Indenter is pressed against the sample and the designated load 'P' is applied

b) Elastic and plastic deformation occurs in the material around the indent

c) Indenter is retreated

d) While elastic deformation is recovered, plastic deformation remains

e) Diagonal lengths of the indents d_1 and d_2 are measured

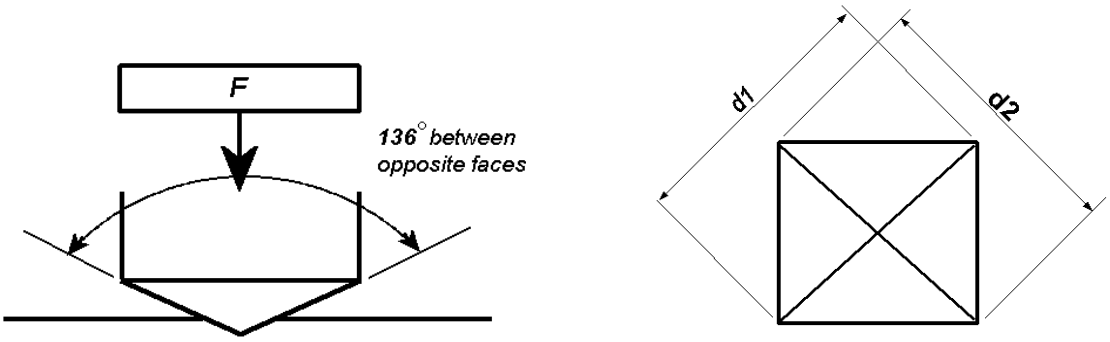

FIG. 2.17 Vickers indenter.

The depth of the indent can be deduced from geometry if d_1 and d_2 are measured. Load and indentation depth are measured during an indentation cycle. A typical curve looks like the curve shown in Figure 2.18. Both hardness and elastic modulus can be calculated using the following equations and load vs. indentation depth curve.

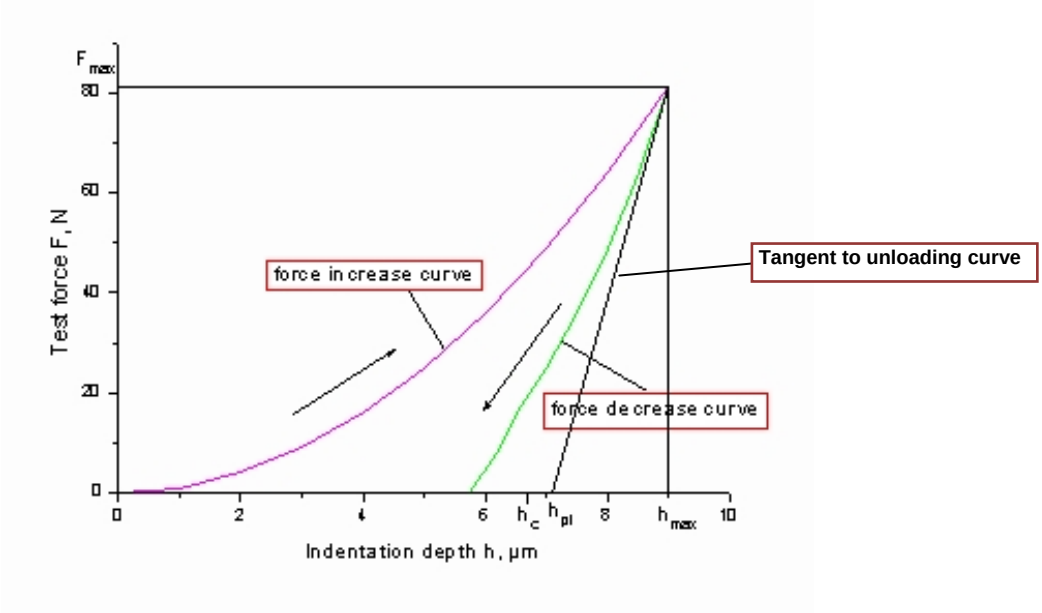

FIG. 2.18 Nano-indentation loading-unloading curve.

In the loading-unloading curve F_{max} indicates the maximum applied load while h_{max} indicates the maximum indentation depth. 'h_{pl}' is the indentation depth value at the tangent to the unloading curve. Indentation hardness, H_{IT} is given by the ratio of the maximum load and the area of contact of the indenter.

$$H_{IT} = F_{max} / A_c$$

Where, F_{max} is the maximum load

A_c is the projected contact area

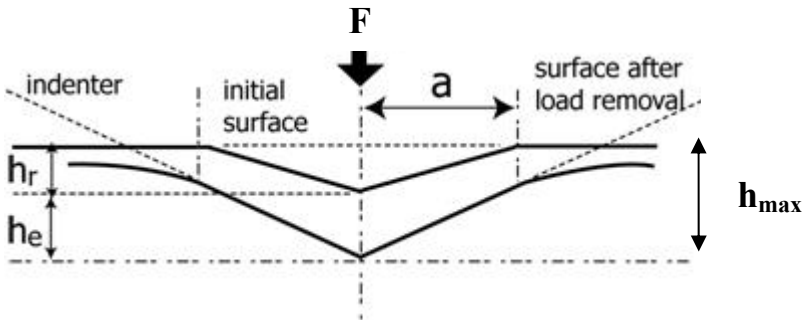

FIG. 2.19 Nanoindent – Important terminology.

$$A_c = f(h_c)$$

Where $h_{c,}$, the height of contact of the indenter is given by

$$h_c = h_{max} - \varepsilon (h_{max} - h_{pl});$$

'ε', is a constant that is a function of the indenter shape.

TABLE 2.1 Values of ε for different indenter geometries.

Indenter shape	**ε**
Flat punch	1.0000
Cone	0.7268
Sphere	0.7500
Paraboloid	0.7500

The value of 'f' is defined for every indenter shape. In this case, f = 24.50 for a Vickers indenter.

$$E_{IT} = (1 - \nu_{IT}^{\ 2}) \Big/ \left\{ \frac{2}{\sqrt{\pi}} X \frac{\sqrt{A(h_c)}}{S} - \frac{(1 - \nu^2_{indenter})}{E_{indenter}} \right\}$$

Where, E_{IT} – Indentation modulus

ν_{IT} – Poisson's ratio for the specimen

A – Area of the indent

h_c - height of contact

$E_{indenter}$ – Modulus of the indenter

$\nu_{indenter}$ – Poisson's ratio of the indenter

2.4.2 Atomic force microscopy and profilometer

Atomic force microscopy is a high resolution scanning probe technique that can measure features with resolution of fraction of a nanometer. Surface information is gathered by a mechanical probe that "feels" the surface features. The probe, usually referred to as cantilever tip has piezoelectric elements that facilitate tiny movements with high level of accuracy.

A *Veeco Dektak 150 stylus profiler* with an automated programmable sample stage has been used for thickness and stress measurements in thin films. The profiler is enabled to do 2-D surface profile measurements. A low-inertia sensor controls the force applied between 1- 15mg and gives a vertical resolution of 1 Å. Profiler is fully automated with a computer assisted operation and programming.

2.5 MAGNETIC PROPERTIES

2.5.1 SQUID - VSM

A vibrating sample magnetometer (VSM) is used to measure magnetic properties. A sample is placed in a uniform magnetic field and physically vibrated in sinusoidal pattern. The magnetic flux across the pickup coils placed around the sample varies sinusoidally inducing a voltage proportional to samples magnetic moment. Magnetization in a sample can be measured under different magnetic fields by varying the strength of the external magnet. In magnetometers with a heating stage, temperature dependence of magnetization can be recorded.

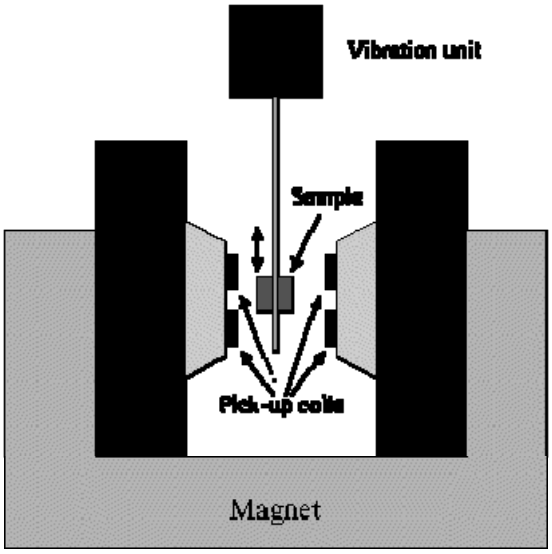

FIG. 2.20 Schematic of Vibration Sample Magnetometer (VSM).

Quantum Design MPMS SQUID VSM has been used to measure the in-plane and out-of-plane magnetic behavior of thin films. The design of the magnetometer combines the sensitivity of super-conducting quantum interference device (SQUID) and the speed of a VSM. M-H and M-T measurements can be done using this apparatus limiting at 7T applied magnetic field and 400K temperature with a sensitivity of $\leq 10^{-8}$ emu.

2.6 PHASE TRANSFORMATION

2.6.1 Differential scanning calorimetry

Differential scanning calorimetry (DSC) is a technique used to study *phase transformation* in materials. Phenomenon such as crystallization, glass-transition, melting etc. can be extensively studied using this technique. A device used for this study is called a differential scanning calorimeter.

For shape memory materials, DSC is a powerful tool to detect crystallization and phase transformation temperature. Though it is a destructive technique, as little as 2mg

of sample is needed to carry out a single run. Due to the high sensitivity, DSC is a widely used technique for thin films. It is necessary that the thin film is free standing to avoid convolution with substrate properties.

The setup of a differential scanning calorimeter consists of two pans connected with heaters and a computer attached to the pan-heater arrangement. A reference pan with known heat capacity and thermal behavior is used alongside the sample pan. After carefully measuring the weight of the sample, it has to be sealed to prevent contamination from oxidation during heating. The two pans are enclosed in an evacuated chamber with heaters attached to controllers. Thermocouples attached to the pans record the temperature of the sample and reference at all times. A computer uses the feedback from the thermocouples to keep the heating rate of both the pans constant at all times.

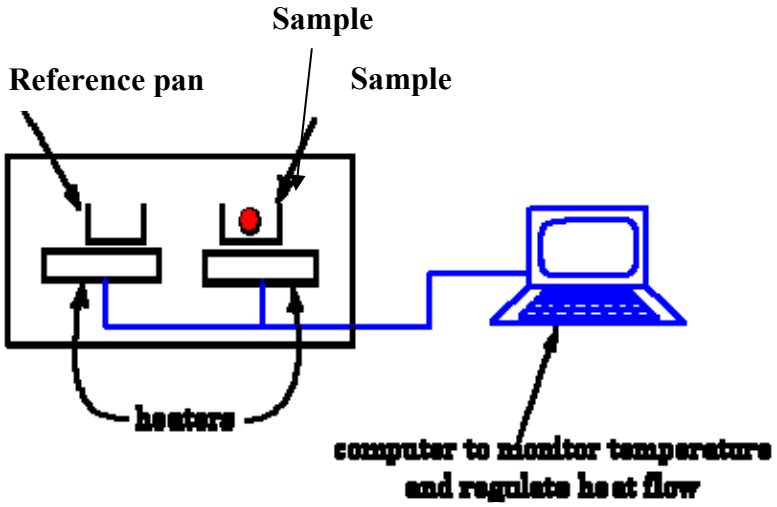

FIG. 2.21 Schematic of differential scanning calorimeter.

To begin with, heating rate, start and end temperatures are entered into the computer. The heat flow of the sample heater as compared with the reference pan is recorded along with the temperature. One heating-cooling run is referred to as a cycle. At the end of a cycle, a DSC plot with temperature on X-axis and Heat flow on the Y-axis is generated. Some of the commonly seen features of the DSC plot are shown in the Figure 2.22.

There are two types of transformations, first and second order transitions. First order phase transformations are the ones that involve a release in latent heat. Crystallization of amorphous metals and martensitic phase transformation are examples of first order transitions as shown in Figure 2.22. While the Second order transitions are ones that do not involve a release of enthalpy. For example, during glass transition no endo- or exothermic peak is observed. Only an increase in specific heat denoted by an elevated heat output is observed as shown in the Figure 2.23.

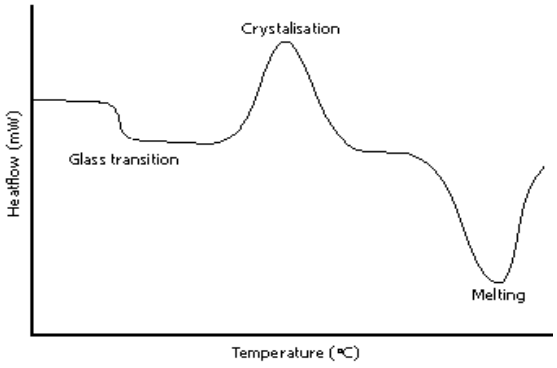

FIG. 2.22 Features in a DSC curve.

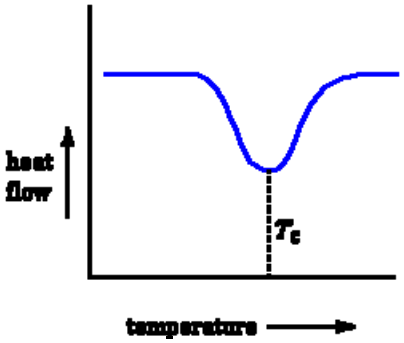

FIG. 2.23 DSC chart – First order transition.

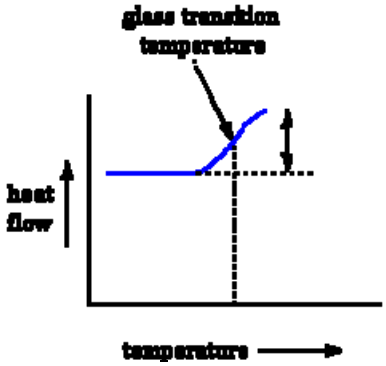

FIG. 2.24 DSC chart – Second order transition.

TA instruments DSC Q1000 has been used for the studies of crystallization and phase transformations in NiMnGa alloy films. The instrument is equipped with a refrigerated cooling system (*RCS*) or finned air cooling system (*FACS*). RCS allows accurate heating and cooling rate control, whereas the FACS gives a higher operation temperature but control heat flow rate only during heating. RCS has a temperature range of -90 to 400ºC and a minimum rate of 10 ºC/min. The temperature range for FACS is RT to 725ºC and is designed rapid heating up to 100ºC/min. The instrument comes with a digital mass flow controller and a 50-position auto-sampler.

A *R180P Sartorius Balance* is used to weigh samples upto 3 decimal accuracy. *TA 900786.901-900779.901 Aluminum pans-lids* which are ideal for temperature range of -180 to 600ºC are used in this case. The weight of the sample and the sample + pans is noted down. The pan with the sample is then crimped using a manual punch to enable better thermal contact and seal the sample.

Universal Analysis 2000 Version 4.5A Build 4.5.0.5 is used for data analysis. Indium which has a low melting point and comparable thermal behavior of typical experimental materials tested is employed as the calibration standard for the system. DSC has been used for determining enthalpy, transformation start, end and peak temperatures.

Enthalpy of reaction,

$$\Delta H = KA$$

K = *Calorimetric constant*

A = *Area under the curve*

Calorimetric constant is unique to the machine and can be determined by using a standard - in this case Indium.

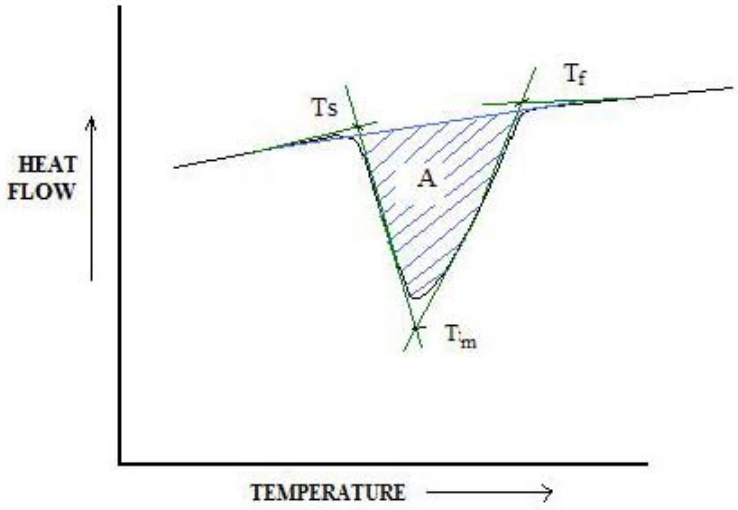

FIG. 2.25 DSC chart analysis.

The tangent option in the software is used to determine the start (T_s), end (T_f) and peak (T_m) temperatures of a transformation. The area under curve option calculates the

area after which the enthalpy of the reaction is determined automatically. Extra features like correcting the baseline etc. can be done with the software.

2.6.2 In-situ annealing in TEM

Temperature is one of the most important factors affecting the state and behavior of materials. For Shape memory materials, in-situ TEM is a powerful tool to detect changes in structure and texture during shape memory effect. Recently in-situ heating TEM has made significant progress in terms of temperature available and resolution attained [66]. Hence TEM can be used to carry out a variety of studies.

Studying grain size evolution and examining the change in surface texture during transformation are some of the studies in-situ TEM technique can be used. A *JEOL JEM-2010* microscope used with an in-situ heating stage attachment allows a temperature upto 1200°C.

2.6.3 In-situ XRD

A *Bruker-AXS D8 diffractometer* with a Beryllium-Dome Temperature Stage (MRI, BTS-Basic) has been used for in-situ X-Ray Diffraction experiments. This high temperature stage is covered with hemispherical Beryllium dome. A mechanical and a turbo molecular pump attachments are provided for achieving high vacuum (~ 10^{-6} mbar) or inert environments inside the Temperature stage. The stage uses Pt (Platinum) heating strip to achieve temperatures as high as 1500 ˚C. A water-cooling system attached to the dome enables stable temperature readings.

Phase transformation from austenite phase which has a $L2_1$ structure below 800˚C to martensite phase which has monoclinic, orthorhombic or tetragonal structure characterized by a number of peaks or vice-versa can be observed. The transformation can be seen as a change in the diffraction spectrum around transformation temperature.

3. SYNTHESIS AND CHARACTERIZATION OF AS-DEPOSITED NiMnGa THIN FILMS

3.1 EXPERIMENTAL METHODS

$Ni_{50}Mn_{31}Ga_{19}$ (C2') and $Ni_{53}Mn_{29}Ga_{18}$ (C4') thin films of 1.7 and 5 μm thicknesses respectively were fabricated using DC magnetron sputtering technique on unheated SiO_2 substrate. The deposition was carried out at a base pressure of $< 1 \times 10^{-7}$ Torr and Ar pressure of $\sim 2.5 \times 10^{-3}$ Torr. Free standing films were obtained by peeling out the deposited films from the substrate manually. *Cameca SX40 electron microprobe* was used to determine the composition with ± 2 at% accuracy. As-deposited crystal structure of films was examined using *Bruker AXS D8 Advanced Bragg Brentano X-Ray Diffractometer* with Cu – K_α radiation. *JOEL JEM-2010* Transmission Electron Microscope with 200kV accelerating voltage and LaB_6 filament has been used for microstructure analysis. Indentation modulus and hardness were obtained by indenting the samples with *Fisherscope HM2000 XYp* fully automatic, pre-programmable hardness tester.

3.2 EVOLUTION OF CHEMISTRY WITH DEPOSITION PARAMETERS

Sputter deposition is a physical process. The sputtering rate of a material is given by its sputter yield (S).

Sputter yield, S = Number of target atoms ejected / Number of incident atoms

Sputter yield is a characteristic of a material and depends on its atomic mass and binding energy. When sputtering an alloy the constituent elements have different

sputtering yields. Hence composition of sputtered alloy thin films depends on the relative sputter yields of individual elements in the alloy. This gives an opportunity to tailor thin film composition by varying deposition parameters such as deposition power, Ar pressure, substrate temperature, that affect sputter yield.

NiMnGa thin films were sputter-deposited by using a 4-source UHV magnetron sputtering system. Two targets with compositions of $Ni_{50}Mn_{25}Ga_{25}$ and $Ni_{49.5}Mn_{30.3}Ga_{20.2}$ have been used. Composition of thin films has been tailored by varying deposition power. Figure 3.1 shows the variation of thin film composition with deposition power density. Basically the concentration of Mn and Ga increase gradually and monotonically with deposition power density, whereas the Ni composition varies in the opposite way.

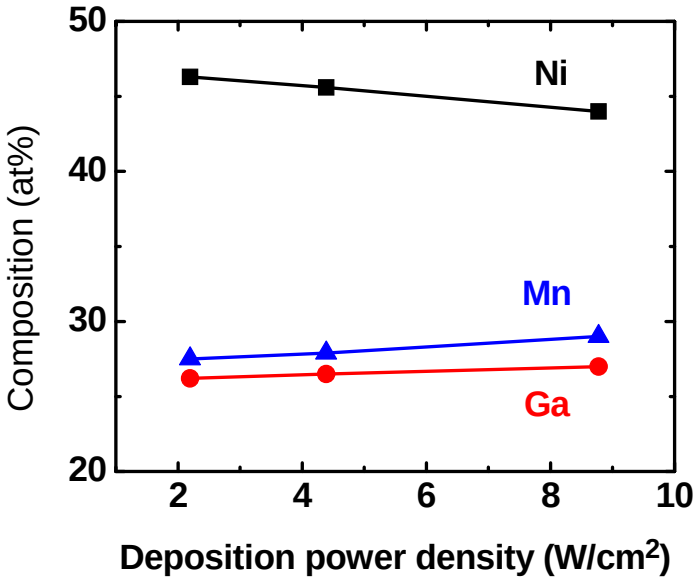

FIG. 3.1 Variation of Ni-Mn-Ga thin film composition with deposition power density.

A similar trend was reported by Lee et al., for ECR – DC (Electro Cyclotron Resonance – Direct Current) magnetron sputtered NiMnGa thin films [31]. The equilibrium vapor pressure of Mn and Ga is 6.0×10^{-38} and 1.1×10^{-36} Pa respectively, much greater than that of Ni (3.9×10^{-63} Pa) [67]. The sputter yield of Mn for 500eV Ar ions is 2.0 compare to 1.0 sputter yield for Ni [68]. Consequently there is a preferential sputtering of Mn and Ga (or loss of Ni) in deposited films. This analysis can be used to develop a recipe to deposit a thin film that shows phase transformation around room temperature. From the e/a vs. temperature chart this corresponds to an e/a range of 7.65-7.7 [2, 23]. Initially stoichiometric $Ni_{50}Mn_{25}Ga_{25}$ target without a backing plate was used for deposition. The compositions of deposited films were determined using wavelength dispersive spectroscopy (WDS) with an accuracy of ±1 at%. The films deposited with this target adhered well to the substrate. The depositions are divided into three groups A, B and C depending on the batch in which they were deposited.

TABLE 3.1 Composition analysis of Batches A and B deposited with $Ni_{50}Mn_{25}Ga_{25}$ target without Cu backing plate.

Sample	Background Pressure	Deposition Power	Ni (at%)	Mn (at%)	Ga (at%)	O (at%)	e/a*
A1	1.6mT	400W	44	27	29	0	7.16
A2	1.6mT	200W	45.6	26.5	27.9	0	7.25
A3	1.6mT	100W	46.3	26.2	27.5	0	7.29
B1	1.6mT	200W	52.6	21.7	25.7	0	7.56
B2	3.2mT	200W	53.1	23.05	23.85	0	7.64
B3	3.2mT	100W	56.9	21.6	21.5	0	7.74

*e/a – [(Ni at%) × 10+(Mn at%) × 7+(Ga at%) × 3] / (Ni at% + Mn at% + Ga at%)

The samples in the **Batch A** were the ones deposited at the very beginning. These films show greater amounts of Ga and low Ni and Mn compared to the target. Increase in base pressure resulted in higher Mn content at the expense of Ga while Ni was relatively unaffected. It can be noticed that these films showed nearly 2.5 - 4 at% higher levels of 'Ga' compared to the target. The e/a ranged between 7.16 - 7.29 which is very low compared to the desired value, ~ 7.5 that can lead to phase transformation at room temperature.

In **Batch B,** thin films were sputtered using the nominal composition target to check reproducibility

During the course of depositions, it was observed that the composition of the films deposited at the same deposition condition was not reproducible. This anomaly can be explained by *target heating effect* possibly due to insufficient cooling of the target. During the sputtering process, the target is subjected to very high thermal energy from the incoming 'Ar' atoms that collide with the target at high velocities. 'Ga' which has a very low melting temperature of 29.7 °C can be easily evaporated from an improperly cooled target. Typically, the cooling system is designed to dissipate this heat and maintain the temperature of the target. Failure to calibrate the target temperature accurately or establish good thermal contact between the target and the cooling system will lead to target over heating effect.

The reproducibility problem has been addressed by providing a Cu (copper) backing plate on the target. Copper which has high thermal conductivity acts as a good

heat exchange layer between the target and coolant. Due to the reduced thermal energy, the sputtered atoms from a well cooled target have lower energies, and hence eliminate thermal evaporation of Ga and Mn.

We have tested the influence of target cooling on film composition control with a 'Mn' rich $Ni_{49.5}Mn_{30.3}Ga_{20.2}$ target with a Cu backing plate. The composition of the films deposited using this target at different powers and background pressures are listed in Table 3.2.

Films deposited using Mn rich target showed compositions close to the target and were reproducible. The influence of deposition power and base pressure on the relative Ni, Mn and Ga contents followed a similar trend as the previous batches.

TABLE 3.2 Composition analysis of Batch C deposited with $Ni_{49.5}Mn_{30.3}Ga_{20.2}$ target without Cu backing plate.

Sample	Background Pressure	Deposition Power	Ni (at%)	Mn (at%)	Ga (at%)	O (at%)	e/a*
C1	2.58mT	100W	50.05	31.15	18.75	0.05	7.75
C2	2.58mT	200W	49.71	31.23	19.06	0	7.72
C3	1.83mT	200W	50.76	31.01	18.23	0	7.79
C4	2.58mT	400W	51.09	30.43	18.48	0	7.79

C2 and C4 compositions were selected for depositing thicker films that can be released from the substrate. Films with thickness of 1.7 and 5μm were deposited on partially oxidized Si (100) substrates at deposition conditions C2 and C4 respectively. These samples will be referred to as C2' and C4' in the rest of the document.

TABLE 3.3 Composition analysis of C2' and C4'.

Sample	Background Pressure	Deposition Power	Ni (at%)	Mn (at%)	Ga (at%)	O (at%)	e/a*
C2'	2.58mT	200W	50.04	31.16	18.8	0	7.75
C4'	2.58mT	400W	53.31	29.10	17.59	0	7.9

The compositions of C2' and C4' are slightly different from the predicted compositions due to the considerably long deposition compared to the previous samples C2 and C4 which are 365 and 415 nm thick respectively. From this we learn that for long depositions, some target heating effect can be anticipated even after adding a Cu backing plate.

3.3 MICROSTRUCTURE OF AS-DEPOSITED THIN FILMS

3.3.1 X – ray diffraction

X- Ray Diffraction of as-deposited films of both the samples showed a broad peak between 43° and 44°. This could suggest partially crystalline structure in the deposited films. Similar observation was reported in sputtered films by Rumpf et al. [36, 69] and PLD deposited films by Tello et al. [48].

The broad peak is indicative of a partially crystalline matrix. The width of the peak indicates grain sizes in the order of nanometers. The peak for samples C2' and C4' are seen at 2 theta values of 42.9° and 43.1° respectively. This shift in the peak indicates a decrease in the lattice parameter in C4'. This is expected from the composition of the films. The atomic radii of Ni, Mn, Ga are:

Ni- 1.62 Å; Mn – 1.79 Å; Ga – 1.81 Å [70].

Compared to C2', the composition of C4' is higher in Ni and lower in Mn and Ga. Fewer Mn and Ga atoms give a smaller unit cell. Hence the peak positions for the same atomic plane in C2' will be at a lower 2θ value than C4' as seen in the XRD spectrum.

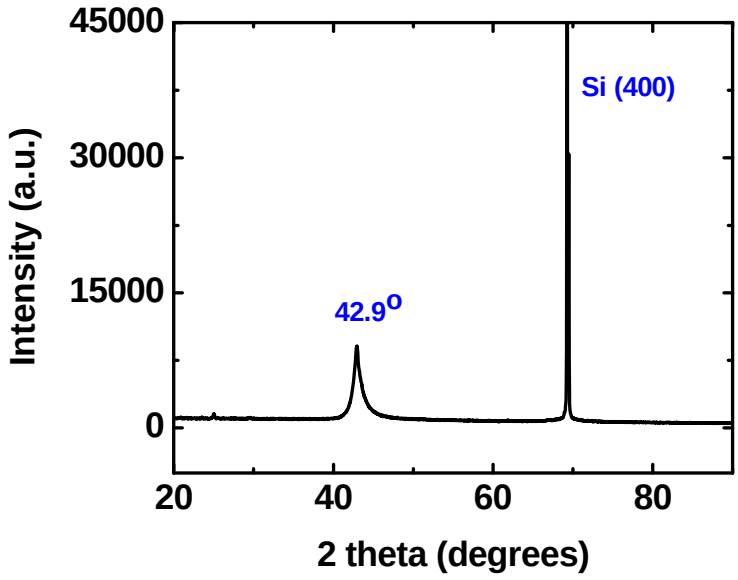

FIG. 3.2 XRD of as-dep C2' film on partially oxidized Si (100) substrate.

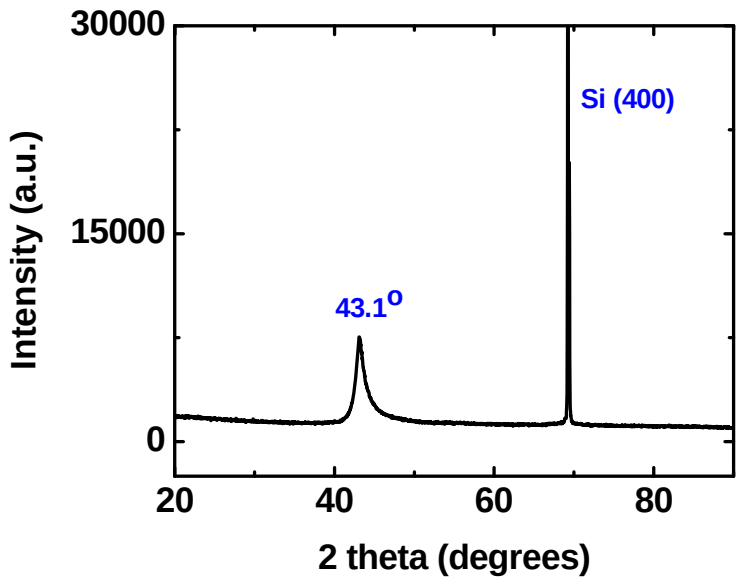

FIG. 3.3 XRD of as-dep C4' film on partially oxidized Si (100) substrate.

3.3.2 Transmission electron microscopy

Plane view TEM of free-standing C2' and C4' confirms the presence of amorphous nano-crystalline matrix. The diffraction pattern for both compositions have circular concentric rings indicating randomly oriented grains. The grain size from the bright field images can be measured to be a few nanometers. Li et al. reported nano-crystalline grains in sputtered films on different substrates including Si [31]. Vovk et al. showed that amorphous disordered films are formed by deposition at RT [42]. Nanocrystalline grain structure was also reported by Rumpf et al. in DC sputtered films [36] and Bernard et al. in RF sputtered films [71].

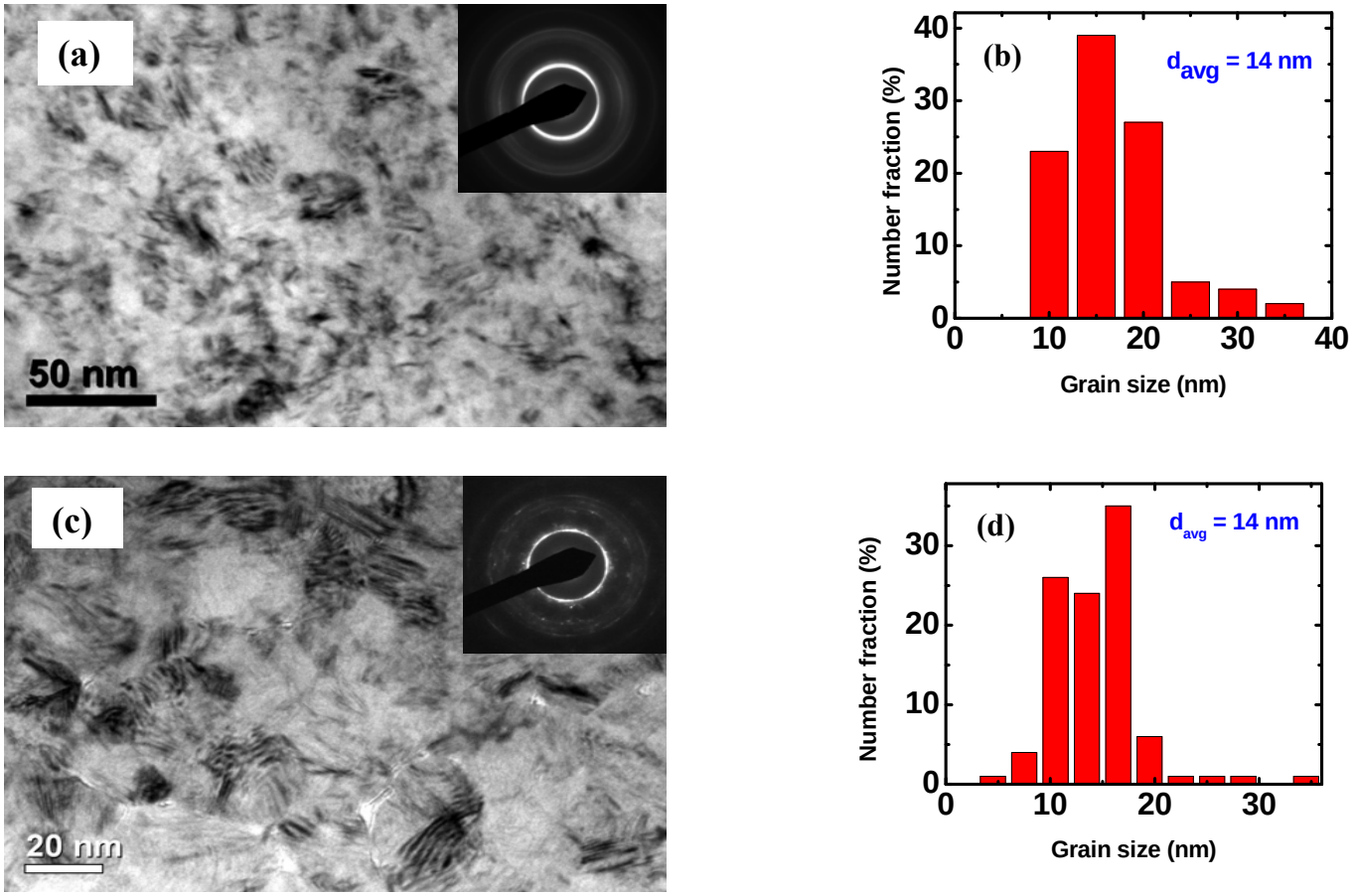

FIG. 3.4 Microstructure of as-dep of C2' and C4'(a) BF of as-dep C2' (b) Grain size chart for as-dep C2' (c) BF of as-dep C4' (d) Grain size chart for as-dep C4'.

The features on the grains indicate fine twinned martensite type texture indicating the existence of nano-crystalline grains with martensites distributed in a seemingly amorphous matrix.

3.4 MECHANICAL PROPERTIES OF THIN FILMS

As-deposited thin films on partially oxidized Si (100) substrates were used for measuring mechanical properties using Nano-indentation. For film C2' indentations were done at 100, 150, 200 and 250 nm. The indentation hardness H_{IT} was measured as 7 ± 0.4 GPa while indentation modulus E_{IT} was measured as 119 ± 6 GPa. Film C4' on partially oxidized Si (100) substrate was indented at 100, 200, 300, 400 nm. The indentation hardness is measured as 7.0 ± 0.2 GPa and the indentation modulus is 133 ± 7 GPa.

The hardness and modulus data for C4' are shown in the Figure 3.6. The indentation modulus values are in agreement with the room temperature sputter deposited thin films reported by and Liu et al. [30], Bernard et al. [71] and Ohtsuka et al. [72]. The higher modulus and hardness values compared to E_{IT} of 80 -95 GPa and H_{IT} of 3-3.5GPa of bulk [72] are suggested to be due to pinning effect during sputter deposition by Ohtsuka et al.

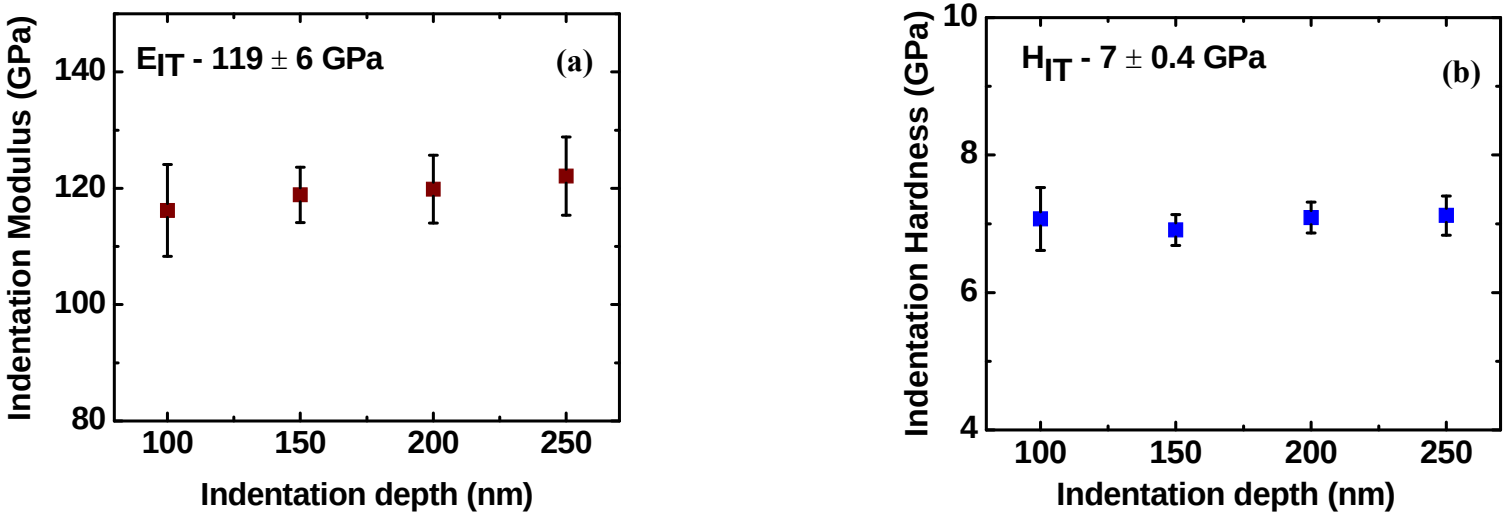

FIG. 3.5 Mechanical properties of C2' (a) Indentation modulus (b) Indentation hardness.

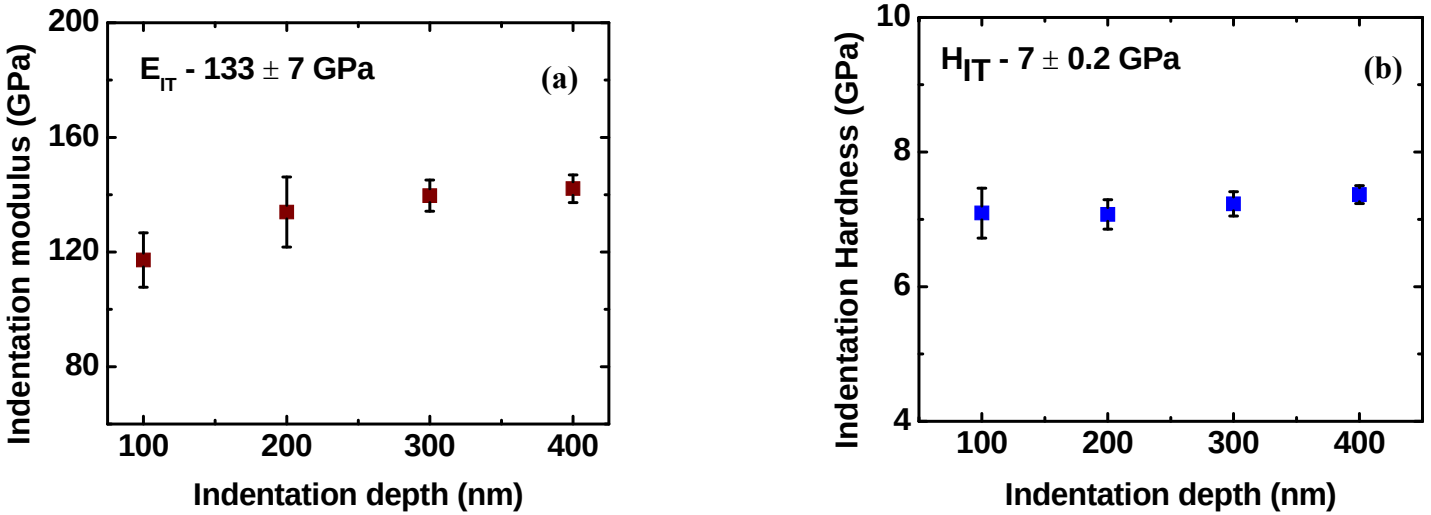

FIG. 3.6 Mechanical properties of C4' (a) Indentation modulus (b) Indentation hardness.

4. PHASE TRANSFORMATION IN Ni-Mn-Ga THIN FILMS

The phase transformation behavior of as-deposited free standing $Ni_{50}Mn_{31}Ga_{19}$ (C2') and $Ni_{53}Mn_{29}Ga_{18}$ (C4') films have been studied using DSC, in-situ XRD and in-situ TEM techniques. *TA instruments Q1000* differential scanning calorimeter with refrigerated cooling system (RCS) and finned air cooling system (FACS) has been used to study the thermal properties of thin films during crystallization and phase transformation. Pressurized DSC cell with FACS attachment was used for Kissinger's analysis of C4' films while DSC cell with RCS attachment was used for the rest of the DSC experiments. In general ~ 2 mg of sample is sealed in Al pans using a hand punch. Transformation in crystal structure of as-deposited 5 μm free-standing C4' film has been studied using *Bruker AXS D8 diffractometer* with a Beryllium-dome temperature stage (MRI, BTS-Basic). The high temperature stage covered with hemispherical Beryllium dome is connected to mechanical and turbo molecular pump attachments for achieving high vacuum (upto 7.5×10^{-7} Torr). Additionally the system can work under inert gas environments. The stage uses a Pt (Platinum) heating strip to achieve temperatures as high as 1500 ˚C. A water-cooling system attached to the dome enables stable temperature readings. TEM samples were prepared after in-situ experiment for grain size and thermal stability analysis. A *JEOL JEM-2010* transmission electron microscope operated at 200kV was used for room temperature and in-situ heating transmission electron microscopy (TEM) experiments. Windows application Powdercell [73] and

Checkcell [74] are used to determine the crystal structure. *Quantum Design MPMS SQUID VSM* has been used to measure magnetic properties of thin film samples.

4.1 CRYSTALLIZATION KINETICS – DSC STUDY

Heating and cooling curves of as-deposited free standing samples of C2' and C4' were obtained using a differential scanning calorimeter (DSC). Isochronous heating curves were used to calculate the crystallization energy using Kissinger's equation.

In the first heating cycle of a typical DSC curve for as-deposited C2' and C4' samples, an exothermic peak corresponding to crystallization is observed as shown in the Figures 4.5 and 4.6. This peak indicates the crystallization of amorphous matrix in the as-deposited films. Figure 4.1 shows the isochronous curves for C2' at heating rates 10, 20, 40 and 80 °C/min. In these films crystallization peak temperature varied from 210 °C to 235 °C at increasing heating rates. The peak crystallization temperatures from different heating rates were used to calculate the activation energy for crystallization using the Kissinger's equation.

$$\ln (\beta/T_p^2) = C - E_a/RT_p \qquad (1)$$

where, T_p is the peak crystallization temperature,

β is the heating rate,

E_a is the effective activation energy for crystallization,

R is the gas constant,

C is a constant.

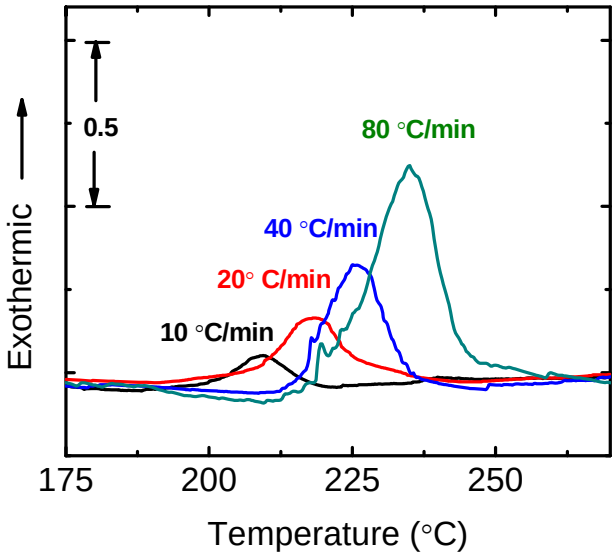

FIG. 4.1 The influence of heating rates on the crystallization of C2' film investigated by DSC technique.

Figure 4.1 is a Kissinger plot of ln (β/T_p^2) vs. $1/T_p$. The effective crystallization energy E_a, was determined to be 157 ± 9 kJ/mol for C2' films. Similar studies were performed for C4' films. For Kissinger's analysis, DSC curves for C4' films were obtained using pressurized DSC cell at ~ 2 atm with FACS attachment. Figure 4.3 shows isochronous heating curves for these films at 10, 20 and 40 °C/min. Crystallization temperatures in the order of 220 – 250 °C were observed at different heating rates. The data from isochronous heating curves is inputted into equation (1) to calculate the activation energy. The computed activation energy E_a is 157 ± 13 kJ/mol. Kissinger plot for C4' films is shown in Figure 4.4.

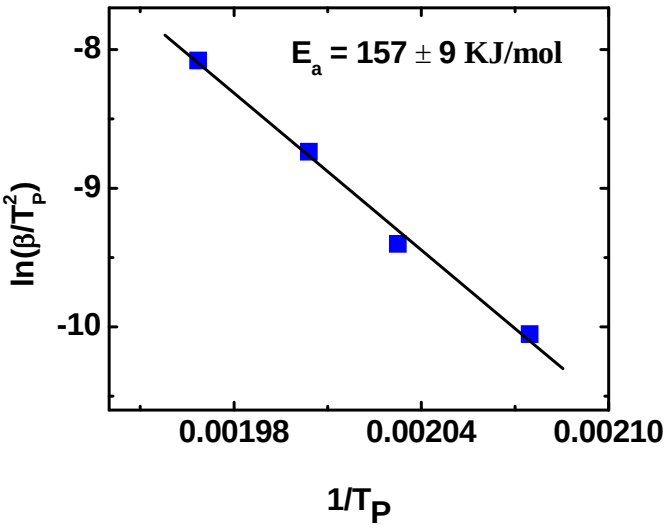

FIG. 4.2 Kissinger's plot for C2' films.

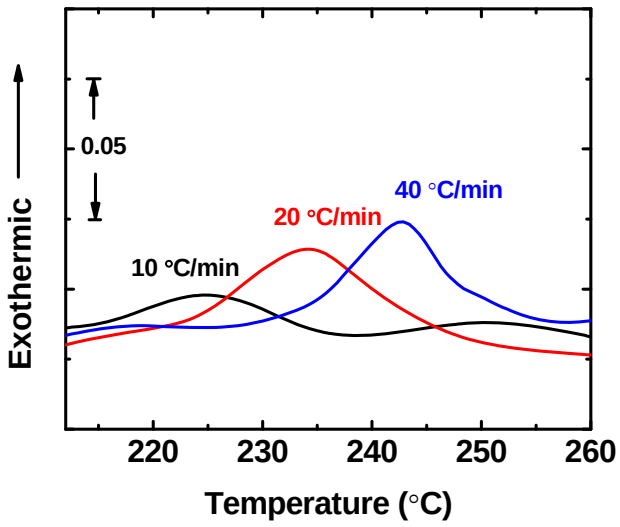

FIG. 4.3 The influence of heating rates on the crystallization of C4' film investigated by DSC technique.

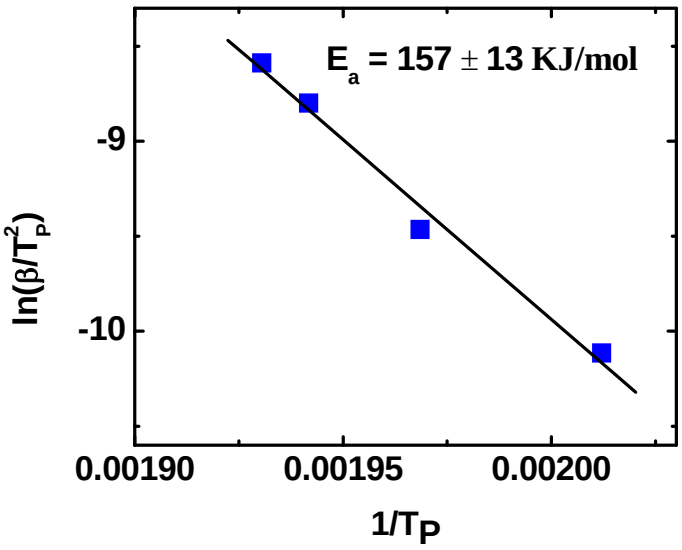

FIG. 4.4 Kissinger's plot for C4' films.

4.2 PHASE TRANSFORMATION

After crystallization in the first heating cycle, the films undergo phase transformation from high temperature cubic austenite phase to low temperature martensite phase during cooling. On consequent heating, reverse phase transformation from martensite to austenite can be observed. This phenomenon has been studied using DSC, in-situ XRD and in-situ TEM techniques.

4.2.1 DSC study of phase transformation in NiMnGa films

C2' films were examined using DSC with RCS attachment. Figure 4.5 shows DSC curve for as-deposited C2' films at a heating rate of 20 °C/min. Crystallization is

observed at the onset temperature which is ~ 193 °C in the first heating cycle. In the 2nd cycle, sample is cooled to room temperature. Martensite start temperature, M_s indicating transformation from austenite to martensite transformation is observed at 117 °C. On heating, a reverse transformation is observed at 69 °C. Subsequent heating and cooling cycles (not shown in the figure) showed reversible phase transformation.

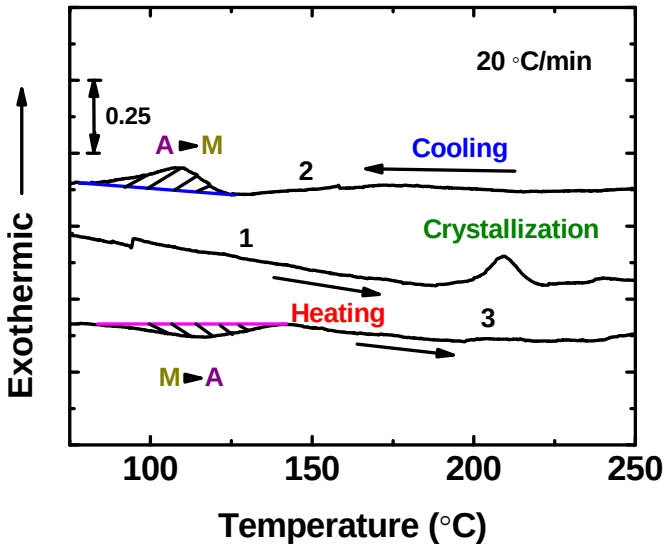

FIG. 4.5 DSC chart for C2' free-standing films.

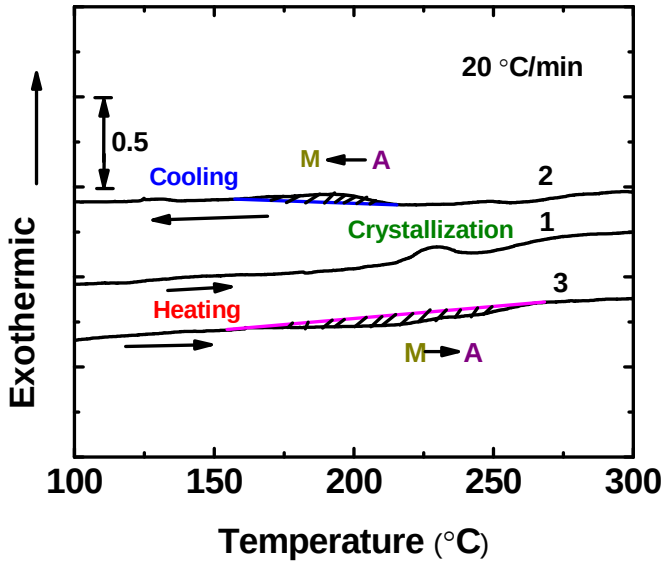

FIG. 4.6 DSC chart of C4' free-standing films.

DSC curves for as-deposited C4' films show the same trend. As shown in Figure 4.6, crystallization occurs at ~ 220 °C for heating rate of 20 °C/min. In the cooling curve, austenite to martensite phase transformation is observed at ~ 205 °C while martensite to austenite phase transformation is observed at ~ 180 °C in the second heating curve. Subsequent heating and cooling curves showed reversible phase transformation.

4.2.2 In – situ XRD

A 5 μm C4' free-standing film was chosen for in-situ XRD experiment to study phase transformations. A 2 × 10 mm film is held onto the heating stage using Al_2O_3

clamps. Specimen was heated to elevated temperature and XRD profiles were collected as shown in Figure 4.7. At 150 °C or lower, a broad peak was observed at ~ 43°. Crystallization is evident after heating the specimen to 250 °C. The major peak was identified as $L2_1$ (022) ($Fm\bar{3}m$; a = 5.84 Å). On further heating this peak diminished in intensity while a new peak to its left became predominant. The new peak can be indexed as $L1_2$ (111) ($Pm\bar{3}m$; a = 3.62 Å). This can be explained as phase segregation of Ni rich precipitates at temperatures above 250 °C.

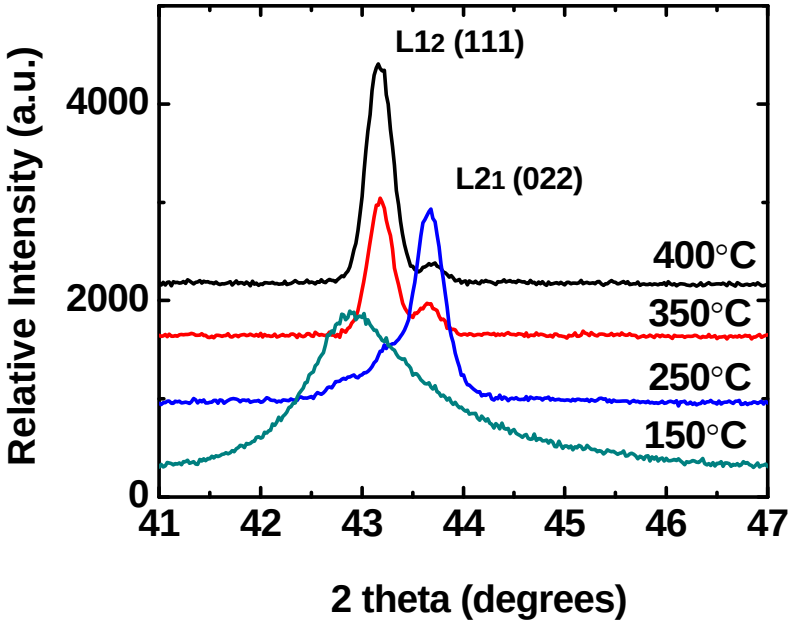

FIG. 4.7 In-situ XRD profiles of NiMnGa films during the first heating cycle. A broad peak is observed at 150° C or below. After heating to 250 °C, crystallization occurs and $L2_1$ phase is identified, which then transforms to a cubic $L1_2$ phase after heating to 350 °C or higher. The $L1_2$ phase appears dominant at 350° C or higher.

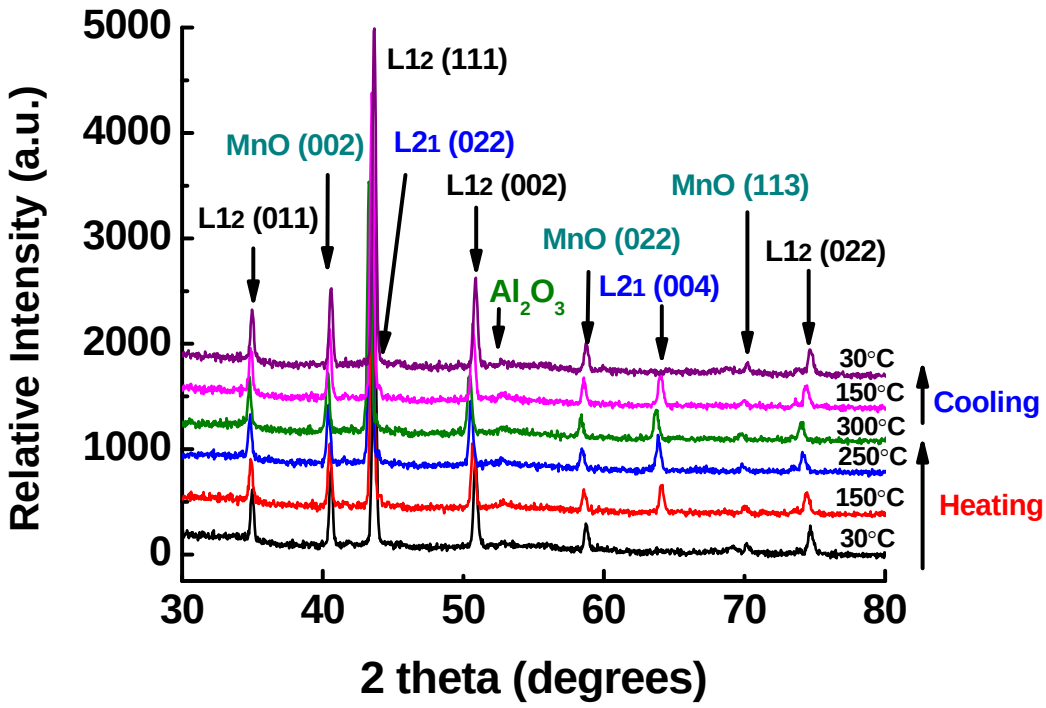

FIG. 4.8 In-situ XRD spectrum for second heating and cooling cycles.

After heating to 400 °C, cooling was applied. In the first cooling cycle (not shown here) the $L2_1$ peaks disappeared indicating phase transformation. To check reproducibility, a second heating and cooling cycle was applied and results are shown in Figures 4.8 and 4.9. From Figure 4.8, it is evident that a majority of the phase appears to be $L1_2$, and it does not transform during heating and cooling. MnO was formed due to the oxidation of films in XRD system. The reversible phase transformation process was captured and shown in a zoom-in XRD profile shown in Figure 4.9. $L2_1$ phase, indicated by $L2_1$ (022) and (004) peaks appears after heating to 150 °C, whereas $L2_1$ peaks

disappear after cooling the specimens to below 150 °C. The martensite peaks have low intensity and overlap with the $L1_2$ phase, and hence cannot be indentified unambiguously.

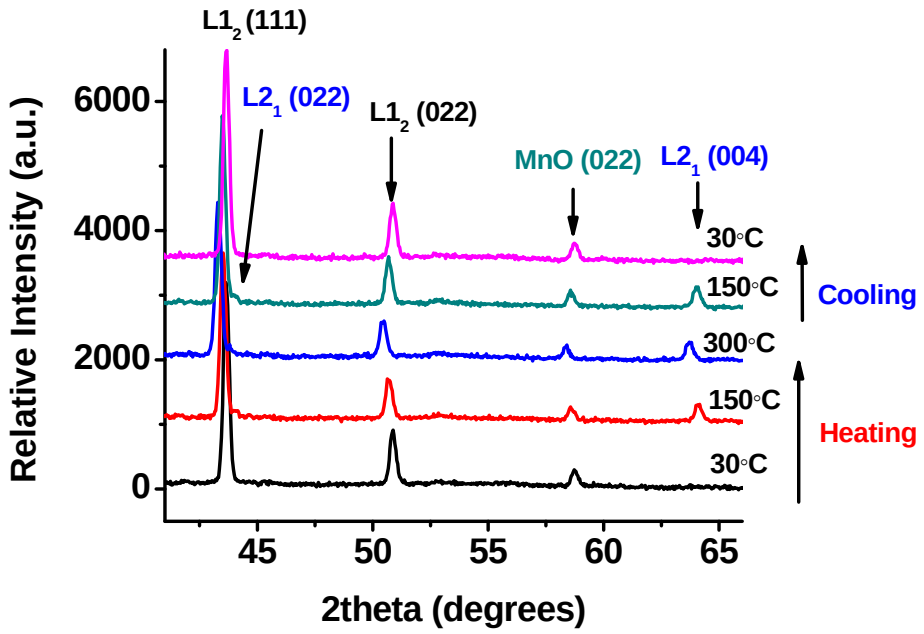

FIG. 4.9 Zoomed in-situ XRD spectrum for second heating and cooling cycles.

To reveal the formation of martensite peaks during in situ XRD studies, one has to suppress or reduce the formation of $L1_2$ phase. As shown in the first heating cycle in Figure 4.7, $L2_1$ phase is predominant at 250 °C, and the phase segregates to $L1_2$ at higher temperature. So we designed an in situ XRD experiment to limit the heating temperature to 250 °C. A 2 × 5mm C4' free-standing film was cycled between RT and 250 °C three times under a vacuum of < 8 x 10^{-5} Torr. In the first heating cycle, crystallization at 250

°C is observed with a well defined $L2_1$ (022) peak at 43.6°. A low intensity $L1_2$ (111) ($Pm\bar{3}m$; a = 3.63 Å) peak is observed at 43.2°. The peak positions agree well with the previous in-situ XRD results. Numerous heating and cooling cycles were performed and results show reversible phase transformation between austenite and martensite. Figure 4.10 shows the evolution of XRD profile during the third heating and cooling cycles. From the relative intensities of $L2_1$ and $L1_2$ peaks we can conclude that the $L1_2$ phase segregation has been considerably suppressed. Below ~ 125 °C the $L2_1$ (022) peak transforms to a split peak with 44.3 and 45.4° 2θ values. These peaks can be indexed as 14M (202), (-127) and (-211) respectively (P2; a = 4.26 Å b = 5.43 Å c = 29.54 Å α=β= 90° γ = 94.3°) using the crystal structure reported by Bernard et al. [71]. The experiment was successful in suppressing the formation of $L1_2$ phase while monitoring the phase transformation between austenite ($L2_1$) and martensite phases.

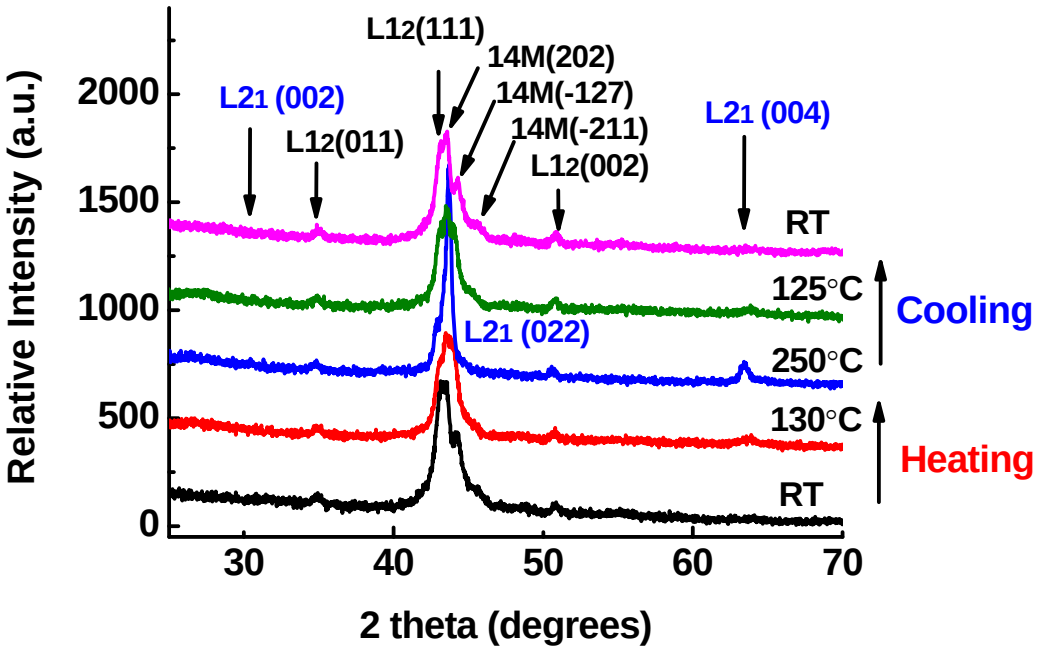

FIG. 4.10 In-situ XRD spectrum for third heating and cooling cycles.

4.2.2.1 Ex-situ TEM analyses (room temperature studies)

TEM samples were prepared from the two specimens used for in-situ XRD experiments for studying the evolution of microstructure. Figure 4.11 (a) shows the bright field TEM images of 250 °C annealed (in-situ XRD sample) specimen. A majority of grains have diameters of 50 nm or less, and the selected area diffraction (SAD) pattern shows a continuous ring. The average grain size is estimated to be ~ 21 nm as shown in Fig. 4.11 (b).

For the 250 °C sample, clear indication of well defined grain structure can be seen from the diffraction pattern. Although not a lot of grain growth is seen, the martensite twins inside the grains are well defined compared to as-deposited samples. In the 400 °C post in-situ XRD sample, grains of a few hundred nanometers with well defined martensite twins are observed. Figure 4.12 shows a bright field image of 400 °C post in-situ XRD sample. In the 400 °C post in-situ XRD sample, as shown in Figure 4.12 (a), grains of a few hundred nanometers with well defined martensite twins are observed. Besides martensite grains, a large population of grains without obvious twin morphology are also observed. Grain coarsening is evident after annealing at elevated temperature. The average grain size is ~ 190 nm for this sample as shown in Figure 4.12 (b).

To examine the phase of grains in more detail, systematic SAD was performed in the specimen annealed at 400 °C. Figure 4.13 (a) shows an area with the co-existence of dark grains with twins as well as precipitates that are brighter and featherless inside the grains. Figure 4.13 (b) - (d) show SAD patterns of labeled grains. Smaller apertures were used to focus the beam on the grains of interest while taking the diffraction patterns. Grain 1 and grain 2 can be indexed as $L1_2$ precipitates. The diffraction pattern of grain 3 shows a 10-layered modulated martensite structure [27]. The high density twins observed on the bright field image of the grain agree well with the diffraction pattern.

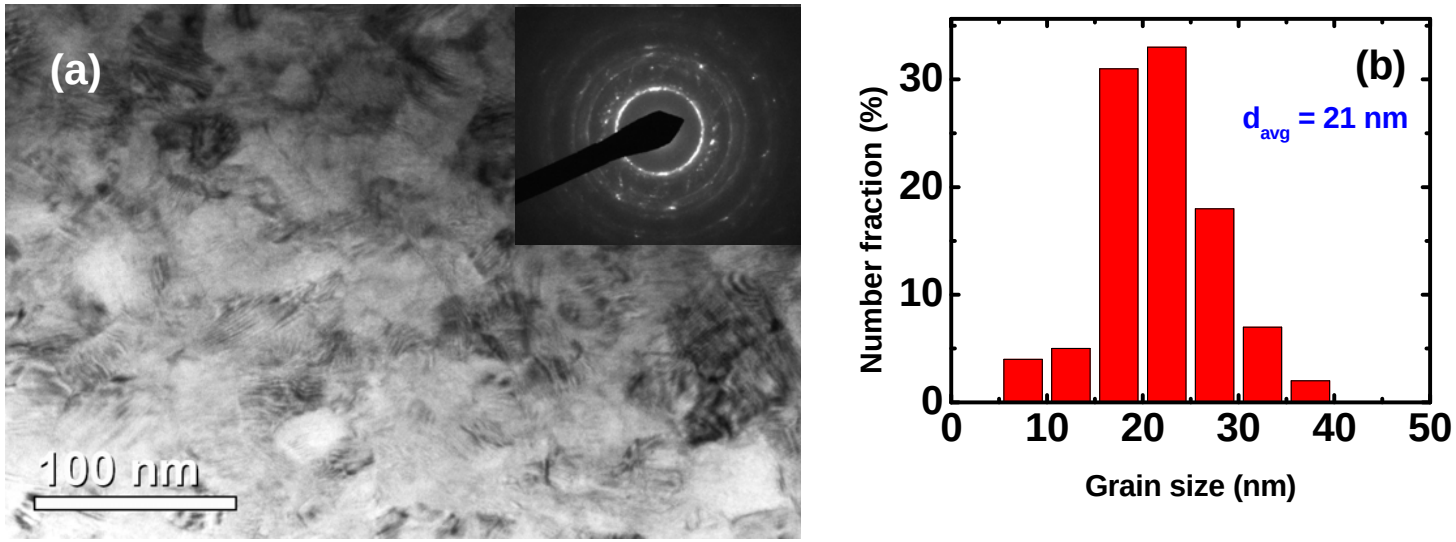

FIG. 4.11 (a) Bright field image of 250 °C in-situ XRD sample (b) Grain size analysis.

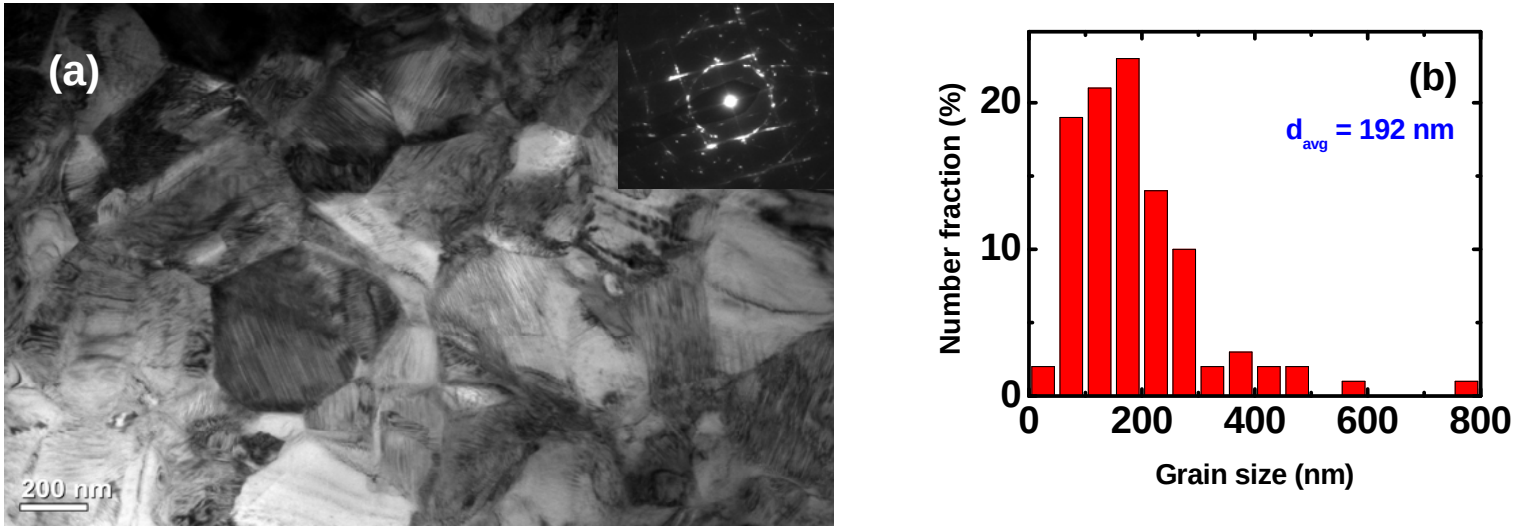

FIG. 4.12 (a) Bright field image of 400 °C in-situ XRD sample (b) Grain size analysis.

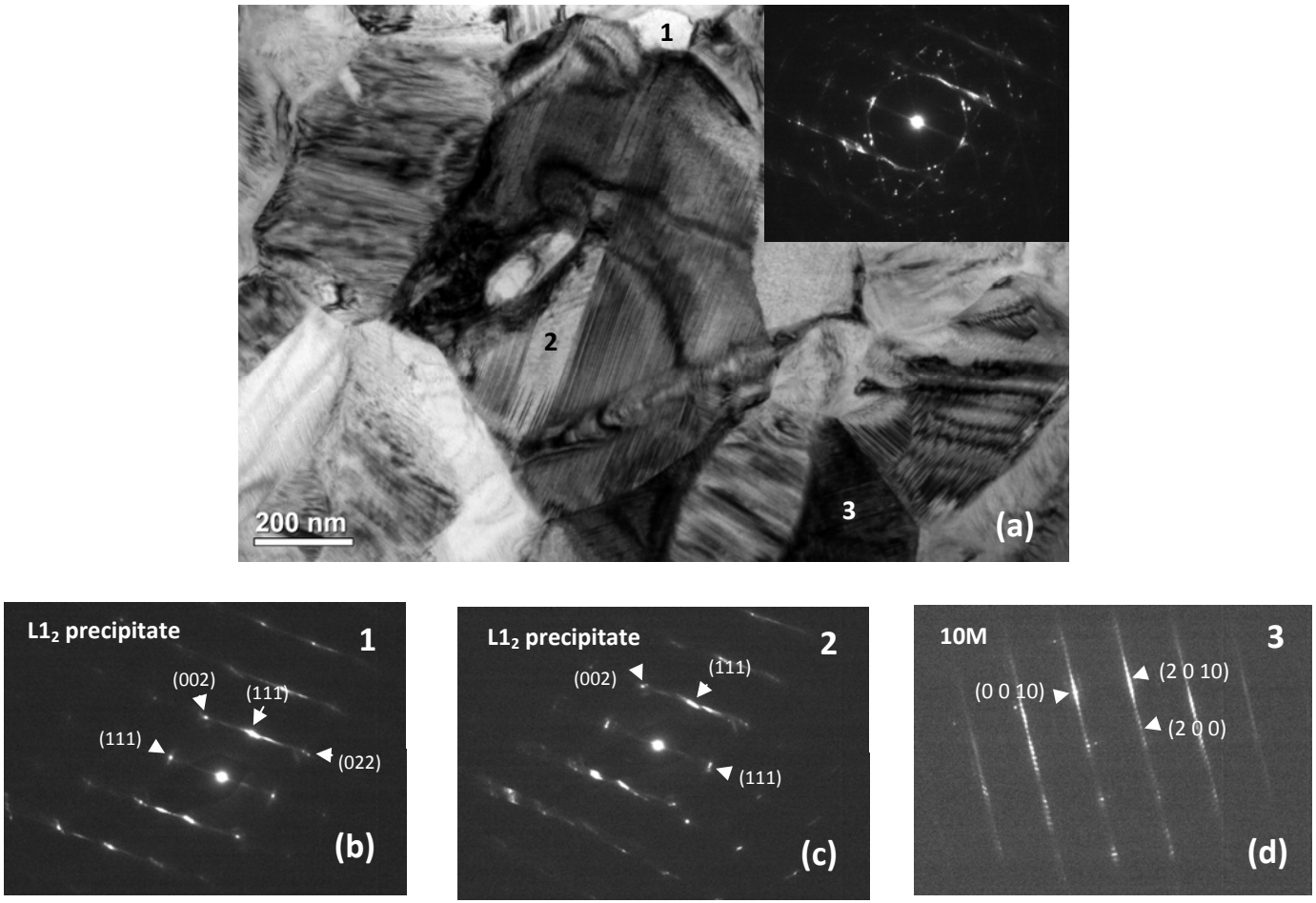

FIG.4.13 Microstructure analysis of 400 °C XRD sample (a) BF image (b) DP of grain1 (c) DP of grain2 (d) DP of grain3.

4.2.3 In – situ TEM studies of phase transformation

4.2.3.1 In - situ TEM of C2'

To examine the evolution of microstructure during phase transformation, in situ TEM experiments were performed on NiMnGa films. Figure 4.14 (a) shows in-situ TEM snap shots of as-deposited C2' sample. As-deposited sample was heated to 500 °C and cooled to room temperature. At room temperature, the bright field image shows nano-grains with an average grain size of ~ 14 nm. The diffraction pattern shows partially crystalline structure with diffuse rings that can be indexed as body center tetragonal, $L1_0$ structure (I4/mmm; a =b= 3.7 Å, c = 7.1 Å). During the heating cycle after 200 °C signs of crystallization are observed in the pattern with well defined rings in the DP. Since the sample is kept at high temperatures for short durations during the in-situ experiment, clear diffraction pattern with austenite structure is observed only beyond 400 °C. Figure 4.14 (b) shows bright field image and DP of this sample at 500 °C.

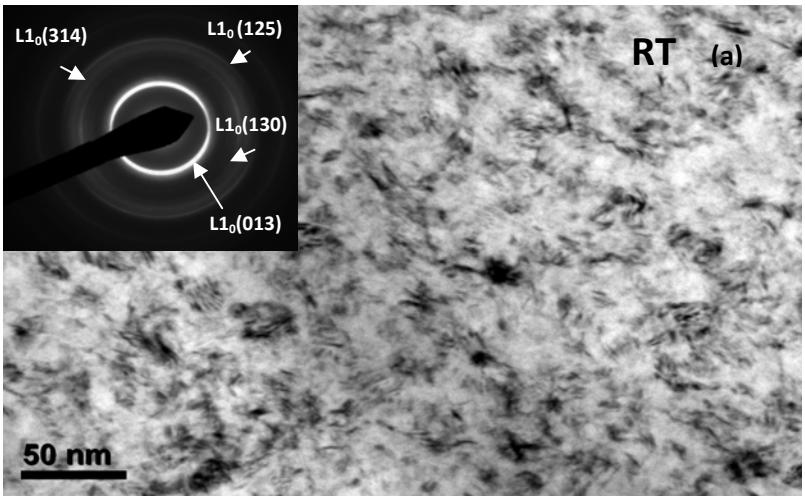

FIG. 4.14 In-situ TEM of C2' sample at (a) RT (b) 500 °C (c) 50 °C.

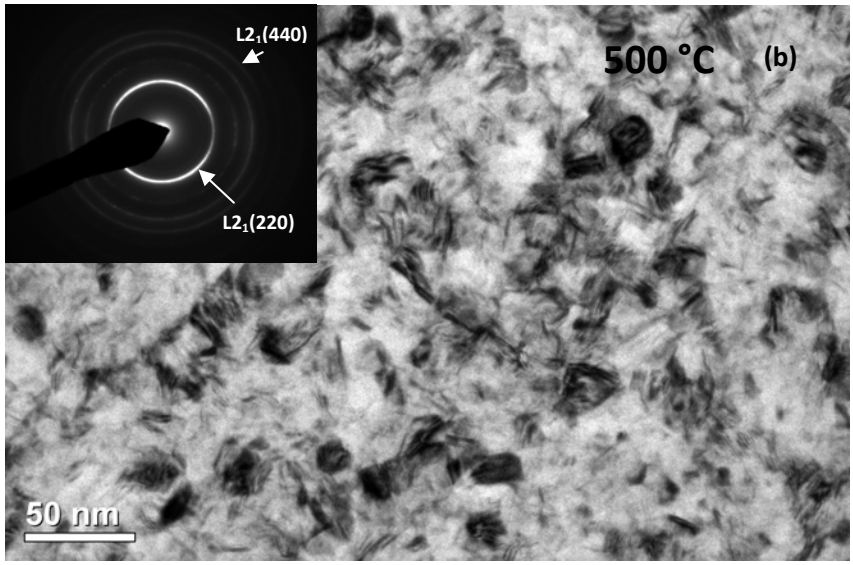

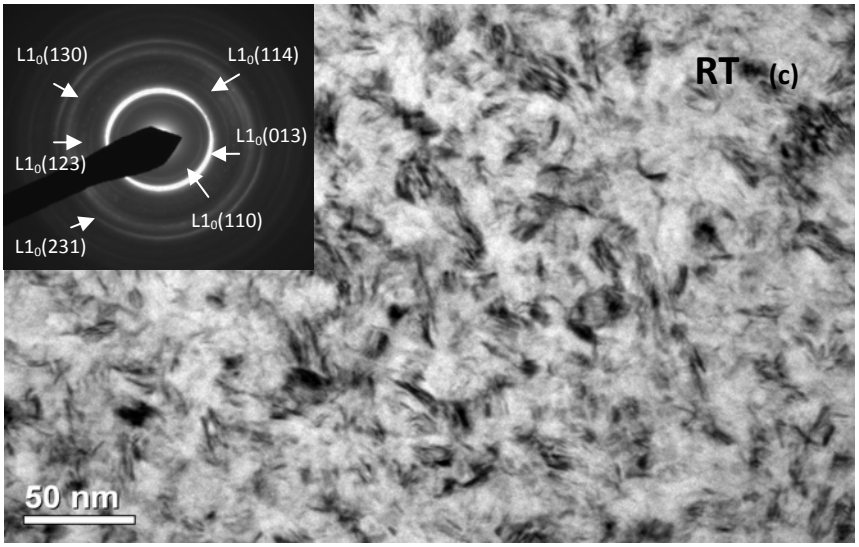

FIG. 4.14 continued.

Larger grains with cubic crystal structure are observed in Figure 4.14 (b). The structure can be indexed as cubic $L2_1$ structure (Fm3m; a = 5.7 Å). A change in DP is observed during the cooling cycle. Figure 4.14 (c) shows the microstructure and DP of the films at room temperature. The structure can be indexed as tetragonal $L1_0$ structure (I4/mmm; a=b= 3.6 Å c = 7.6 Å). The diffraction pattern shows a more defined crystal structure compared to as-deposited sample.

4.2.3.2 In-situ TEM of C4'

TEM sample has been prepared from 400 °C post in-situ XRD specimen. Phase transformation and corresponding crystal structure change in the grain highlighted in Figure 4.15 (a) was studied during the in-situ experiment. At room temperature, the grain has fine twin texture. The SADP of the grain indicates modulated texture characterized by the super lattice dots in the diffraction pattern.

At approximately 170 °C, a change in the crystal structure is noticed as shown in Figure 4.15 (b). The bright field image of the grain shows a change in twinned texture on the grain. In Figure 4.15 (c) near the peak transformation temperature at 230 °C the crystal structure transforms completely to cubic structure. The crystal structure in the DP can be indexed as a $L2_1$ austenite structure (a = 5.84 Å). Cooling to room temperature induces a reverse transformation to martensite structure with twinned texture and modulation in the diffraction pattern as shown in Figure 4.15 (d).

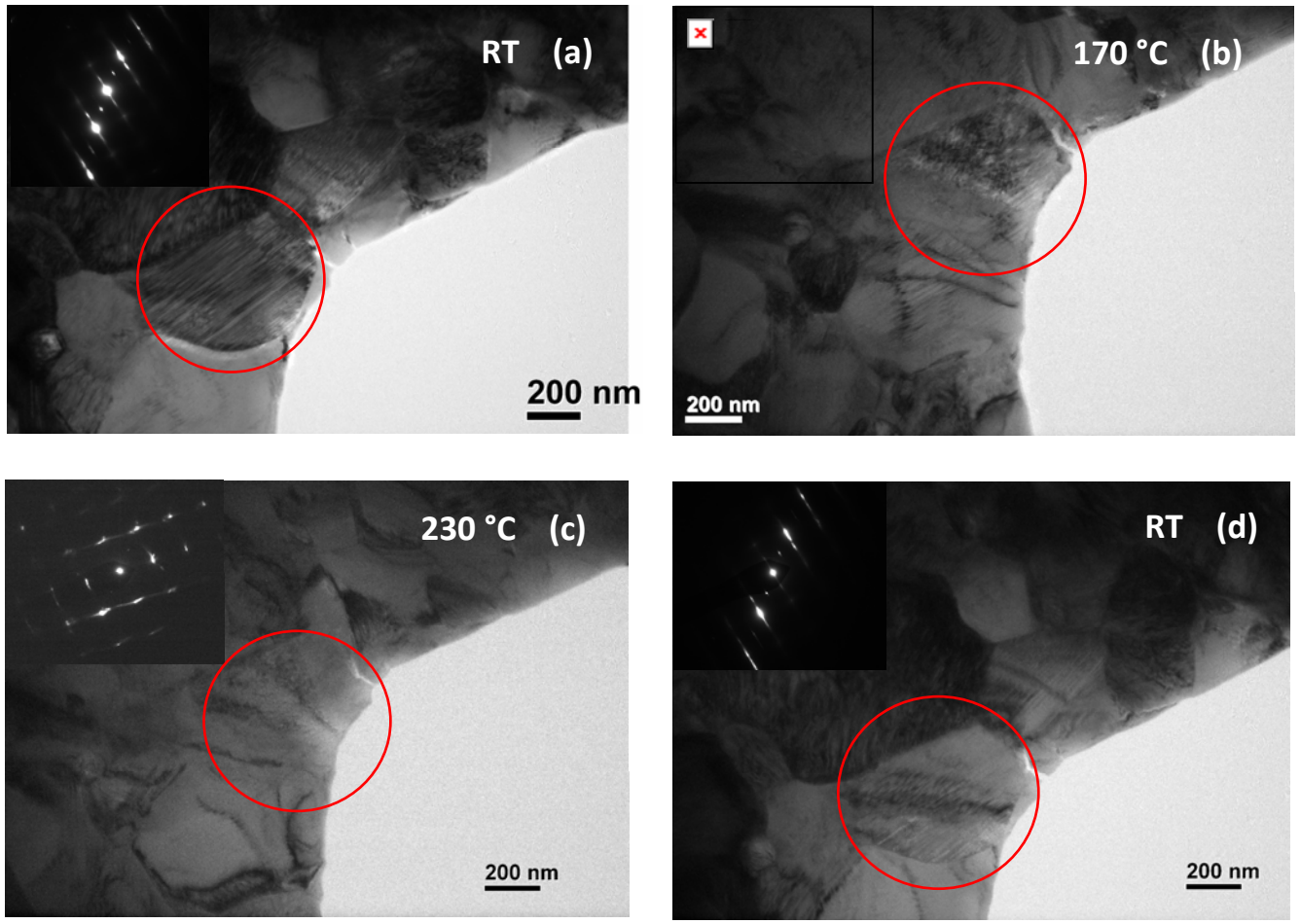

FIG. 4.15 In-situ TEM experiment on 400 °C in-situ XRD sample (a) RT (b) 170 °C (c) 230 °C (d) RT.

4.3 PRELIMINARY STUDIES ON MAGNETIC PROPERTIES

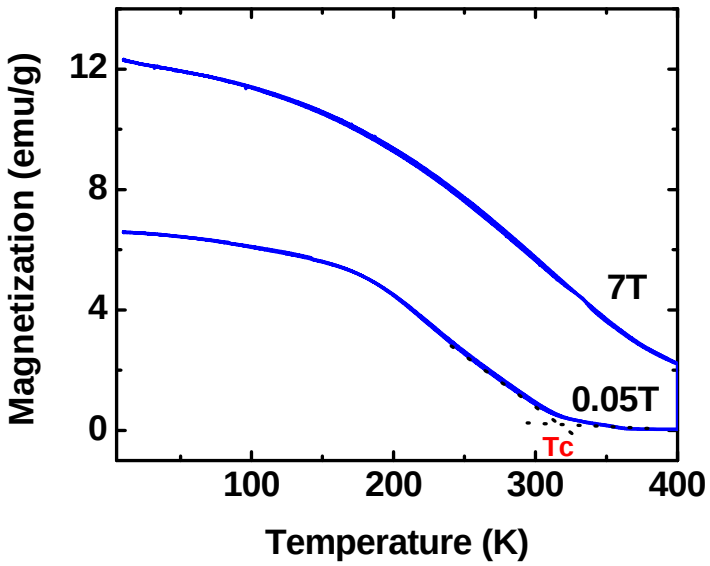

FIG. 4.16 M -T curve of 250 °C in-situ XRD sample.

Magnetization vs. temperature (M-T) curves for 250 °C in-situ XRD sample were obtained using Quantum SQUID VSM. Zero field cool (ZFC) at 0.05 T and field cooled (FC) measurements at 7 T were obtained while heating and cooling the sample from 400 – 4K. Magnetic transformation was observed in the ZFC M-T curve at 318 K. Figure 4.16 shows M-T curve for heating and cooling cycles at ZFC and FC.

4.4 DISCUSSION

We have shown that films with compositions $Ni_{50}Mn_{31}Ga_{19}$ (C2') and $Ni_{53}Mn_{29}Ga_{18}$ (C4') of 1.7 and 5 μm thickness respectively were deposited on unheated

SiO_2 substrates. By manually releasing them from the substrate, free standing thin films were obtained. The microstructure of sputter-deposited NiMnGa films has been consistently reported as nano-crystalline grains distributed in amorphous matrix [31, 42, 71]. In our films, similar grain structure with twins is observed inside the nano-grains. X-ray diffraction of these films showed a broad peak between 43 - 44° typical of NiMnGa thin films [36, 48, 69] suggesting fine grain size. In this section, we will discuss the thermal processing and property measurements carried out on these as-deposited films.

a) Mechanical properties

One of the main motivations for studying NiMnGa in thin film is the poor ductility of bulk NiMnGa. Due to its brittleness, bulk NiMnGa cannot be bent into required shape for applications.

In our study, we determined the hardness and modulus of as-deposited thin films C2' and C4' as 7 ± 0.4 GPa (H_{IT}), 119 ± 6 GPa (E_{IT}) and 7.0 ± 0.2 GPa (H_{IT}), 133 ± 7 GPa (E_{IT}) compared to 3 - 3.5GPa (H_{IT}), 80 -95 GPa (E_{IT}) for bulk [72]. From microstructure study, it can be concluded that thin films deposited using sputter deposition have nanograins which act as barriers for the propagation of dislocations, and hence the nanograins lead to strengthening of the material. This is consistent with previous observations [72].

b) Crystallization kinetics

From microstructure studies, it is clear that partially crystalline grain structure exists in as-deposited films. There is high driving force for the amorphous matrix to

crystallize and for coarsening of nanograins. Both events will decrease the overall Gibbs free energy of the system. The crystallization process has been studied by conducting isochronous heating experiments for C2' and C4' films in DSC. Kissinger's equation listed as equation (1) is used to calculate the activation energy for crystallization E_a from the isochronous heating curves. E_a is determined to be 157 ± 13 kJ/mol (C4') and 157 ± 9 kJ/mol (C2'). Consistent crystallization values of C2' and C4' suggest similar microstructure in as-deposited films of both compositions. The crystallization temperature and activation energy values agree well with the value reported by Wu et al. for r.f. sputtered near stoichiometric NiMnGa thin films [75]. Typically, sputtered thin films of shape memory alloys like NiTi have a much higher crystallization temperature and activation energy of the order of 511 °C and 416 kJ/mol for $Ti_{49.93}Ni_{50.07}$ [76]. The low crystallization values for NiMnGa thin films could be due to the partial crystallinity in the films. The broad peak in the as-deposited XRD graph supports this theory. In comparing to NiMnCoIn, the crystallization energy of the film with predominantly amorphous matrix is approximately 239 kJ/mol [77].

c) DSC studies of phase transformation

We used DSC curves to study forward and reverse phase transformation phenomenon of C2' and C4' specimens. In a typical DSC curve, crystallization is followed by an exothermic peak indicating transformation to martensite on cooling below phase transformation temperature. When the sample is re-heated, martensite transforms to austenite as indicated by an endothermic peak. These two transformation

peaks have been used to measure the forward and reverse phase transformation temperatures.

Using this method, the martensite start temperature (M_s) for C2' and C4' have been determined as 117 and 210 °C respectively. In literature phase transformation temperatures for Ni-Mn-Ga have been shown to be a function of e/a value [23, 36, 60]. In line with that theory, Jin et al. showed this trend in e/a vs. M_s plot. Shown in the Figure 4.17 is a chart for this empirical relationship. The blue data points embedded on the curve represent our C2' and C4' data obtained from the DSC curves. The observed M_s temperatures agree very well with the prediction of empirical relationship.

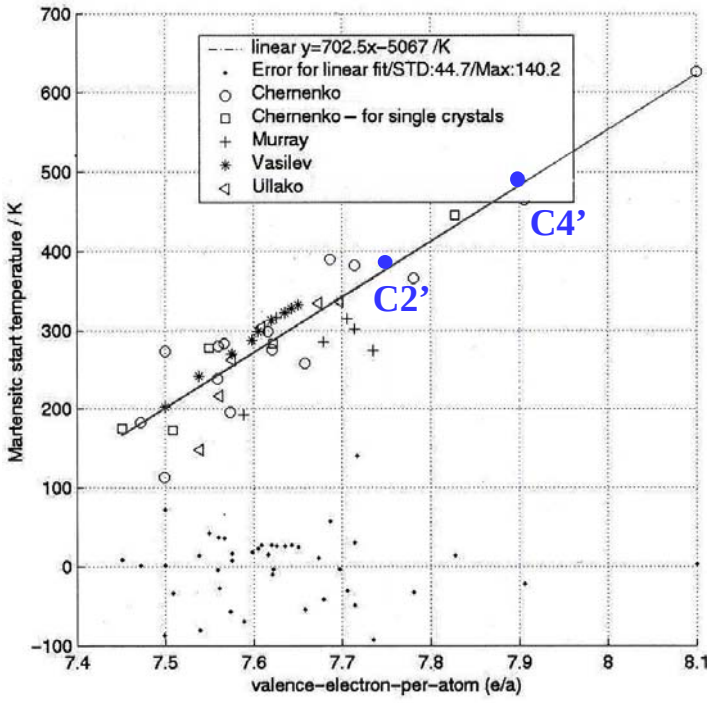

FIG. 4.17 e/a plot showing C2' and C4' compositions.

d) <u>In situ XRD studies of phase transformations</u>

In-situ XRD experiments have been designed to extend phase transformation study and understand the change in crystal structure during transformation. 5 μm thick C4' film has been heated to a maximum temperature of 400 °C. From Figure 4.7 we can observe crystallization in the film at ~ 250 °C which is in good agreement with DSC measurements. The crystallized peak at ~ 44° was indexed as $L2_1$ (022) peak which is the crystal structure for austenite phase. Since the crystallization temperature is higher than the estimated transformation temperature (from DSC), the crystallized grains are expected to have an austenite phase.

Further heating shows phase segregation into a cubic $L1_2$ phase. From the peak intensities, it appears that $L1_2$ phase segregation is aided by high temperatures. At 400 °C this phase dominated the diffraction pattern indicating large volume fraction of this phase. Ni rich compositions in bulk [78] and thin films [25] have been reported to form these precipitates which commonly have $Ni_3(MnGa)$ compositions with $L1_2$ ($Pm\bar{3}m$) crystal structure and a small unit cell (a ~ 3.6 Å). No indication of phase transformation was observed in these precipitates. Santamarta et al. referred to these precipitates as γ' phase in bulk specimen. This phase was found to have $Ni_3(MnGa)$ composition that was very different from the matrix composition [78].

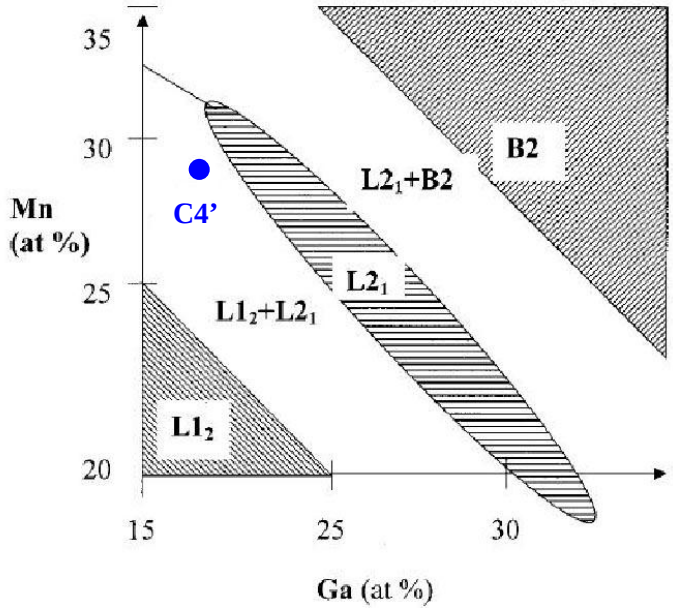

FIG. 4.18 Phase diagram of Ni-Mn-Ga alloy [48].

Tello et al. proposed a hypothetic phase diagram for Ni-Mn-Ga using Thermocalc shown in the Figure 4.18 [48]. The black dot shows the composition of C4' on the phase diagram which predicts a mixture of $L1_2$ and $L2_1$. Our observations in the diffraction spectrum shown in Figure 4.8 and TEM study shown in Figure 4.13 is consistent with this prediction.

Apart from phase segregation to $L1_2$, formation of MnO ($Fm\bar{3}m$; a = 4.4 Å) is observed in the first and second cycles of XRD spectrum. Formation of MnO precipitates in NiMnGa films is observed even during annealing in inert gas environments [25]. Suzuki et al. conducted annealing experiments for NiMnGa thin films under vacuum and inert conditions. They showed that MnO precipitates are always observed in annealed films irrespective of the method of heat treatment [25]. Gerbert et

al. showed the formation of 'Mn' oxides on the surfaces of bulk NiMnGa exposed to air [79].

Although reversible phase transformation can be deduced from austenite peaks shown in Figures 4.8 and 4.9, there is no trace of martensite in the XRD spectrum. Martensite peaks in thin films are usually observed near 42 - 44° [36, 48, 69, 71]. In this specimen, due to the high relative intensity from $L1_2$ phase, the martensite peaks could have been embedded in it.

Since $L1_2$ phase does not transfer to martensite, it is desirable to suppress their formation. In-situ XRD annealing experiment using low temperatures (RT → 250 °C) has been used on another C4' as-deposited specimen. The low annealing temperature (250 °C) would suppress precipitation and provide temperatures just enough for crystallization. Figure 4.10 shows the diffraction spectrum of the second heating cycle from this experiment. The as-deposited film showed crystallization at ~ 250 °C. A well defined $L2_1$ (022) peak was formed in the crystallized specimen. As per the prediction of the theoretical phase diagram, low intensity $L1_2$ peak is observed even for the low annealing temperature. However, we were successful in showing suppression in $L1_2$ phase segregation. In line with the previous argument, martensite peaks were observed between 42 - 44°. The crystal structure of martensite could be ambiguously indexed as 14M using the structure suggested by Pons et al. [27]. In-situ XRD experiment has been a powerful tool to study crystal structures and phase segregation associated with NiMnGa thin films.

e) Ex situ TEM analyses

TEM analysis of in-situ XRD samples was done to better understand the changes in microstructure during in-situ heating in XRD. Grain growth analyses and evidence for phase segregation was probed during these experiments. Figures 4.11 (a) and 4.12 (a) show bright field TEM images of 250 °C and 400 °C in-situ XRD annealed samples. From the grain size analysis shown in Figure 4.11 (b) and 4.12 (b), a clear distinction in grain size and its distribution is seen in 400 °C compared to the low temperature annealing experiment. The SAD pattern of 250 °C in-situ annealed XRD sample showed a well defined crystal structure with an average grain size of 21nm. The concentric ring pattern in DP is indicative of randomly oriented nano-crystalline grains.

The 400 °C in-situ XRD sample showed large martensite grains ~ 200 nm in diameter with well defined twins inside grains. In the SAD patterns of this sample, extra spots on the diffraction pattern are a clear indication of modulated structure commonly seen in Ni-Mn-Ga martensites. From the TEM images, it is clear that even though reversible transformation to martensite occurred in the matrix, due to the relative intensity of the $L1_2$ peaks, it cannot be detected in the XRD pattern.

SAD analysis of an area in 400 °C in-situ XRD annealed sample shown in Figure 4.13 shows the co-existence of $L1_2$ precipitates and martensite grains. No feather (twin) like features were seen on the precipitate grains supporting the observation from in-situ XRD experiment that they do not transform. $L1_2$ precipitates seemed to be randomly distributed in the sample.

Growth in grain size is coupled with well defined ordering in martensite grains resulting from larger grain growth. Rumpf et al. showed that larger grain size in NiMnGa alloy allows accommodation of modulated martensite structures that leads to well defined ordering in martensite structure [36].

f) In situ TEM analyses of microstructure evolution during phase transformation

In-situ TEM analysis was done on the specimen that was in situ annealed in XRD up to 400 °C to demonstrate reversible phase transformation from modulated structure in martensite phase to cubic structure in austenite phase. Figure 4.15 shows bright field and SAD pattern on a single grain in the sample. A grain showing well defined modulations highlighted in Figure 4.15 (a) was probed during in-situ heating and cooling in the microscope. A clear indication of transformation from distorted martensite structure to cubic austenite structure can be observed. The SAD images at different temperatures manifested this transformation well. The M_s, M_f and T_M temperatures agreed well with the DSC results for this sample shown in Figure 4.6.

As-deposited C2' sample was also annealed in-situ in TEM. The diffuse ring structure indicative of nanocrystalline grains at room temperature transformed to well defined structure that could be indexed as a mixture of austenite and martensite. A good diffraction pattern showing austenite structure could be obtained only after heating to 500 °C possibly due to short annealing times used in the in situ experiment. As suggested before from the work of Rumpf et al., it is necessary to reach a critical grain size for observing shape memory related transformation in grains. On cooling to room temperature, martensite phase indexed as tetragonal $L1_0$ structure was formed.

g) Magnetic properties

M – T curves for 250 °C in-situ XRD sample at ZFC and FC from 400 K to 4 K showed magnetic transformation above room temperature at 318 K. Figure 4.19 shows an empirical T_c vs. e/a plot proposed by Chernenko et al. [23]. The plot shows that Curie temperature is a function of e/a value and is inversely related to it. The blue data point on the plot indicated the T_c value of C4' as measured from M-T curve. We can see that the value agrees well with the empirical profile.

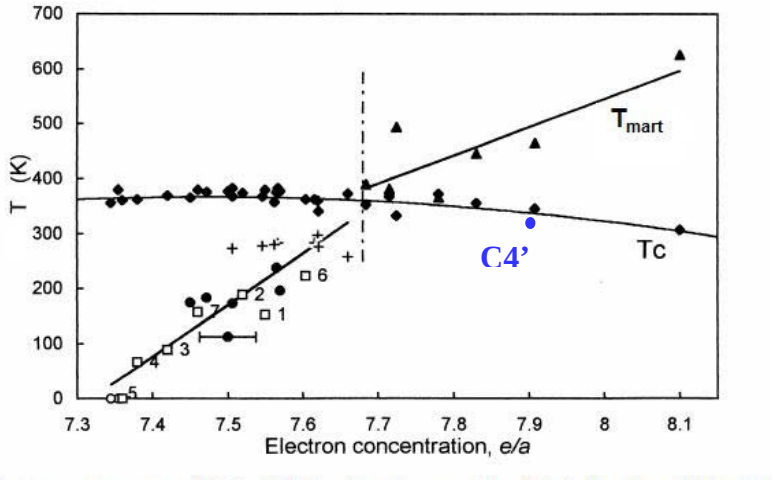

FIG. 4.19 T_c vs. e/a plot showing T_c value of C4' from M-T curve.

A maximum magnetization of 6.5 emu/g is observed in this sample. Rumpf et al. showed that as-deposited sputtered thin films show little or no ferromagnetism due to lack of magnetic ordering in the nanometer size grains [36]. Evolution of magnetic ordering was observed by annealing the thin films to obtain larger grains in the order of a few hundred nanometers. With an average grain size of a 192 nm, we predict that the low value of magnetization is due to the small grain size.

5. SUMMARY AND CONCLUSIONS

Free standing films have been fabricated using magnetron sputtering technique. Composition of the deposited alloy was tailored by varying deposition parameters. Increase in power density resulted in favorable sputtering of Mn and Ga while Ni followed a reverse trend. The higher sputter yield of Mn and low vapor pressure of Ga over Ni are assumed to be responsible for this behavior. The microstructure of as-deposited thin films was characterized by nanometer size grains with martensite like features distributed in an amorphous matrix. Thin films, $Ni_{50}Mn_{31}Ga_{19}$ (C2') and $Ni_{53}Mn_{29}Ga_{18}$ (C4') with thicknesses 1.7 and 5 μm respectively are chosen for further analysis. Crystallization kinetics of these films showed a crystallization temperature around 200 °C. Kissinger's equation has been used to calculate the activation energy for crystallization as 157 ± 9 kJ/mol and 157 ± 13 kJ/mol for C2' and C4' respectively.

Hardness and modulus of these films measured using nano-indentation showed superior hardness and modulus compared to bulk NiMnGa [80]. Hardness values were determined as 7 ± 0.4 GPa and 7 ± 0.2 GPa while indentation modulus E_{IT} was measured as 119 ± 6 GPa. and133 ± 7 GPa respectively for C2' and C4'. These values are higher compared to the bulk values of 3-3.5 GPa and 80 -95 GPa for hardness and modulus [80]. This is attributed to the pinning effect in sputter deposited thin films [72].

DSC experiments showed reversible phase transformation in both the compositions. C2' showed the austenite start temperature at ~ 69 °C in the heating cycle and martensite start temperature at 117 °C in the cooling cycle. C4' showed austenite

transformation at ~ 183 °C and martensite transformation at ~ 205 °C. The increased temperatures are due to the higher e/a owing to the composition of C4'. Phase transformation of free-standing C4' films was examined using in-situ XRD experiments. In the first experiment, the sample was heated to 400 °C and cooled to room temperature. Crystallization was observed ~ 250 °C during the first heating cycle. Reversible transformation was observed in the $L2_1$ austenite peaks. Phase segregation to $L1_2$ was observed at temperatures above 200 °C. This phase did not show any transformation during the heating and cooling cycles. The detection of martensite phase is compromised since the dominant $L1_2$ (111) peak near the 2θ value coincides with several martensite peaks in NiMnGa. In the second in situ XRD experiments, heating up to 250 °C is enough to crystallize the films, whereas the temperature is sufficiently low to suppress the formation of $L1_2$ phase significantly. And consequently the formation of martensites are clearly observed during phase transformation.

Microstructure study of post in-situ XRD sample annealed up to 400 °C shows well defined martensite grains in the sample. Hence it can be concluded that the absence of martensite peaks in the diffraction spectrum is due to the dominant precipitate intensity. Clear indication of $L1_2$ precipitates distributed around the matrix is seen from TEM analyses. *In-situ* TEM analysis of this sample shows a clear transformation in crystal structure from modulated structure at room temperature to cubic $L2_1$ austenite structure at temperatures greater than the martensite-to-austenite transformation temperature consistent with DSC studies.

The diffraction patterns showed crystallization at 250 °C and reversible phase transformation below 175 °C. $L1_2$ phase is observed although the volume fraction is low. The martensite peaks can be indexed as 14M according to a structure proposed by Bernard et al. [71]. TEM study of post in-situ XRD sample shows grain growth and well defined martensite structure compared to as-deposited samples. The limited grain growth could be due to the lower annealing temperatures used in the XRD experiment.

M-T measurements for this sample show a magnetic transformation from high temperature paramagnetic austenite to weakly magnetic austenite at Curie temperature, T_c = 318 K. Below this temperature, the material is already in martensite phase. The magnetization value for martensite is ~ 6.5 emu/g.

In summary, we were able to demonstrate that high quality polycrystalline free standing films for use in future MEMS devices can be fabricated on SiO_2 substrates using DC magnetron sputtering. As-deposited thin films showed superior mechanical properties compared to bulk. Films showed low value of activation energy that eases the temperature required for re-crystallization of the films. Phase segregation in Ni-rich compositions could be suppressed by using low temperature annealing process. Thermal and micro-structural changes associated with reversible phase transformation and thermal shape memory effects have been corroborated using DSC, in-situ XRD and in-situ TEM techniques. Magnetic properties of the films showing magnetic transformation temperature (T_c) and magnetization in martensite phase has been obtained using SQUID – VSM technique.

6. FUTURE WORK

Ideal ferromagnetic shape memory alloys have transformation temperature (T_{mart}) around room temperature, low saturation magnetization of martensite (M_s), high Curie temperature (T_c). In this project, we were able to produce thin films with T_{mart} ~ 218 °C, M_s 6.5 emu/g, T_c 318 K that showed reversible phase transformation. To develop Ni-Mn-Ga thin films that can be used as future MEMS actuator materials, improvement in achieving desirable composition, microstructure and magnetization properties are necessary. Figure 6.1 shows an empirical map of Ni-Mn-Ga alloys proposed by Jin et al. [60]. The grayed area indicates the desired Ni-Mn-Ga alloys that show high saturation magnetization while retaining magnetic shape memory properties at room temperature. The highlighted area on the map shows the ideal composition of thin films that we aim to fabricate. In order to develop processes to produce such thin films a threefold investigation as detailed below is necessary.

a) Annealing of thin films ex-situ using a two step annealing condition to improve thermal stability and magnetic properties of thin films. Ex-situ annealing of polycrystalline thin films is shown to improve the structural, magnetic ordering and thermal stability of Ni-Mn-Ga alloys [36]. A two step ordering using high temperature homogenization and low temperature ordering can suppress the formation of $L1_2$ in Ni-rich compositions [25]. Moreover, larger grain sizes of thin films are shown to ease magnetic and shape memory effect due to reduced constraint from grain boundary easing re-orientation and phase transformation in grains [36].

b) Deposition conditions for fabricating Ni-Mn-Ga alloy thin films with lower e/a value that have T_{mart} near room temperature and higher saturation magnetization can be produced using the behavior of Ni, Mn and Ga seen in this project. Richard et al. showed that compositions with Ni > 50% lead to anti-ferromagnetic coupling of Mn atoms resulting in a lower overall magnetization value [81]. Hence we would like to tailor the composition to vary e/a by increasing Mn at the expense of Ni leading to compositions that have high magnetization values.

c) Deposition of epitaxial thin films on heated substrates to produce thin films devoid of defects and superior magnetic ordering. High growth temperatures have been shown as necessary for ferromagnetic ordering in Ni-Mn-Ga [36, 38].

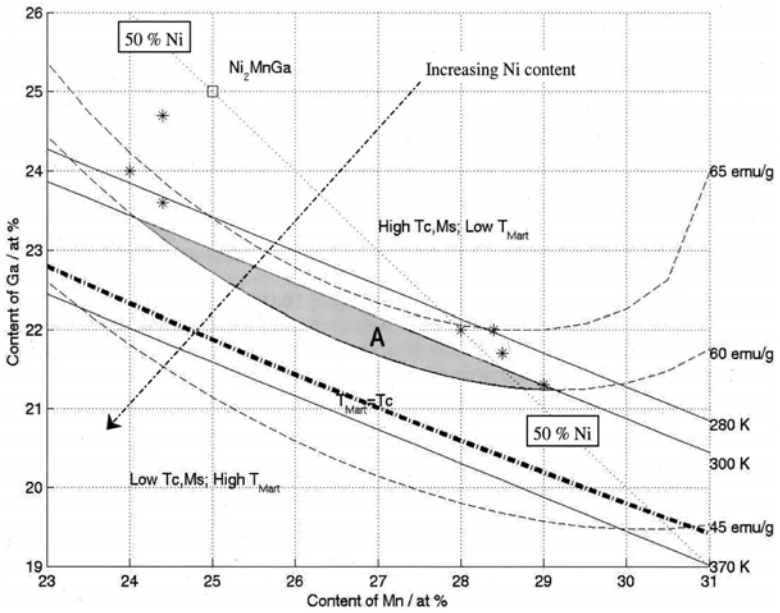

FIG. 6.1 Empirical composition map for Ni-Mn-Ga [60].

REFERENCES

[1] E. P. Wohlfarth and K. H. J. Bushchow: *Ferromagnetic materials* (Elsevier, U. K., 1980).

[2] R. Abbundi and A. E. Clark: J. Appl. Phys. Vol. 49 (1978), p. 1969.

[3] D. G. Lord, V. Elliott, A. E. Clark, J. P. Teter, H. T. Savage and O. D. McMasters: J. Appl. Phys. Vol. 63 (1988), p. 3910.

[4] K. Ohtsuka, H. Sakamoto and K. Shimizu: Acta Metallurgica Vol. 27 (1979), p. 585.

[5] R. C. O' Handley, S. J. Murray, M. Marioni, H. Nembach and S. M. Allen: J. Appl. Phys. Vol. 87 (2000), p. 4712.

[6] A. Sozinov, A. A. Likhachev, N. Lanska and K. Ullakko: Appl. Phys. Lttr. Vol. 80, No. 10 (2002), p. 1746.

[7] K. Ullakko, J. K. Huang, C. Kantner, R. C. O'Handley and V. V. Kokorin: Appl. Phys. Lett. Vol. 69 (1996), p. 1966.

[8] F. Heusler, F. Starck and E. Haupt: Verh. Phys. Ges. (German) 1903 Vol. 5 (1903), p. 220.

[9] Author data not available: *http://www.adaptamat.com/technology/properties/* Properties comparison of MSM with other smart materials, (AdaptaMat, Helsinki, Finland) Accessed online on 5/27/2010.

[10] M. Kohl, S. Hoffman, Y. Liu, M. Ohtsuka and T. Takagi: J. De Phys. IV: JP Vol. 112 II (2003), p. 1185.

[11] F. Khelfaoui, M. Kohl, J. Buschbeck, O. Heczko, S. Fahler and L. Schultz: Eur. Phys. J. Special Topics Vol. 158 (2008), p. 167.

[12] A. Planes, L. Manosa and M. Acet: J. Phys. Condens. Matter Vol. 21 (2009), p. 233201.

[13] Author data not available: *http://www.resonancepub.com/actuator.htm* Hysteresis loops in shape memory alloys (Rutgers University, Piscataway, NJ), Accessed online on 5/27/2010.

[14] Author data not available: *http://www.mete.metu.edu.tr/pages/sma/* Effect of temperature on mechanical properties of Smart materials (Middle Eastern Technical University, Ankara, Turkey), Accessed online on 5/27/2010.

[15] Author data not available: *http://www.riken.go.jp/lab-www/nanomag/research/ heusler_e. html* Half metallic ferromagnets – Heusler alloys, Accessed online on 5/27/2010.

[16] P. J. Webster and K. R. A. Ziebeck: Landolt-Barnstein New Series Group III Vol. 19C (1988), p. 75.

[17] R. A. de Groot, F. M. Mueller, P. G. van Engen and K. H. J. Buschow: Phys. Rev. Lett. Vol. 50 (1983), p. 2024.

[18] C. Zener: Phys. Rev. Vol. 81, No. 4 (1951), p. 440.

[19] F. A. Hames: J. Appl. Phys. Vol. 31:5 (1960), p. 307S.

[20] J. Soltys: Acta. Phys. Pol. A Vol. 46 (1974), p. 383.

[21] J. Soltys: Ibid. Vol. 47 (1975), p. 521.

[22] A. N. Vasil'ev, A. D. Bozhko, V. V. Khovailo, I. E. Dikshtein and V. G. Shavrov: Phys. Rev. B Vol. 59 (1999), p. 1113.

[23] V. A. Chernenko: Scr. Materialia. Vol. 40, No. 5 (1999), p. 523.

[25] R. W. Overholser and M. Wuttig: Scripta Materialia Vol. 10 (1999), p. 1095.

[25] M. Suzuki, M. Ohtsuka, M. Matsumoto, Y. Murakami, D. Shindo and K. Itagaki: Mater. Trans. Vol. 43, No. 5 (2002), p. 861.

[26] J. Pons, R. Santamarta, V. A. Chernenko and E. Cesari: Mater. Science and Engg. Vol. A (2006), p. 438.

[27] J. Pons, V. Chernenko, R. Santamarta and E. Cesari: Acta Mater. Vol. 48 (2000), p. 3027.

[28] S. Morito, K. Otsuka: Mater. Science and Engg. A Vol. 208 (1996), p. 47.

[29] Kainuma R., Nakano H. and Ishida K.: Metallurgical and Mater. Trans. Vol. 27A (1996), p. 4153.

[30] C. Liu, Z. Y. Gao, H. B. Wang, L. X. Gao and W. Cai: Appl. Surf. Sci. Vol. 254 (2008), p. 2861.

[31] C. Li, J. Sun, G. Sun, G. Yao and Z. Chen: Surf. Coatings Tech. Vol. 201 (2007), p. 5348.

[32] V. O. Golub, A. Y. Vovk, L. Malkinski, C. O'Connor, Z. J. Wabg and J. K. Tang: J. Appl. Phys. Vol. 96 (2004), p. 3865.

[33] K. Bhattacharya and R. D. James: Science Vol. 307 (2005), p. 53.

[34] C. Biswas, R. Rawat and S. R. Barman: Appl. Phys. Lett. Vol. 86 (2005), p. 202508.

[35] M. Kohl, A. Agarwal, V. A. Chernenko, M. Ohtsuka and K. Seemann: Mater. Sci. Engg. A Vol. 438 (2006), p. 940.

[36] H. Rumpf, H. Craciunecu, H. Modrow, Kh. Olimov, E. Quandt and M. Wuttig: J. Magnetism and Magnetic Materials Vol. 302 (2006), p. 421.

[37] M. Thomas, O. Heczko, J. Buschbeck, U. K. Robler, J. McCord, N. Scheerbaum, L. Schultz and S. Fahler: New J. Phys. Vol. 10 (2008), p. 023040.

[38] A. Hakola, O. Heczko, A. Jaakkola, T. Kajava and K. Ullakko: Appl. Phys. A Vol. 79 (2004), p. 1505.

[39] M. Matsumoto, M. Ohtsuka, K. Itagaki, T. Takagi and T. Fujino: J. Phys. IV France Vol. 11 (2001), p. 275.

[40] J. W. Dong, L. C. Chen, J. Q. Xie, T. A. R. Muller, Carr D. M., C. J. Palmstrom, S. McKernan, Q. Pan and R. D. James: J. Appl. Phys. Vol. 88, No. 12 (2000), p. 7357.

[41] J. Dubowik, Y. V. Kudryavtsev and Y. P. Lee: J. Magn. Magn. Mater. Vol. 1178 (2004), p. 272.

[42] A. Vovk, L. Malkinski, V. Golub, C. O'Connor, Z. Wang and J. Tang: J. Appl. Phys. Vol. 97 (2005), p. 10C503.

[43] K. Otsuka and C. M. Wayman: *Shape memory materials* (Cambridge University Press, Cambridge, 1998).

[44] A. Jae-Pyoung, N. Cheng, L. Thomas and M. K. Kannan: IEEE Trans. Magn. Vol. 37, No. 4 (2001), p. 2141.

[45] Y. Zhang, R. A. Hughes, J. F. Britten, W. Gong, J. S. Preston, G. A. Botton and M. Niewczas: Smart Mater Struct Vol. 18 (2009), p. 025019.

[46] O. Heczko, M. Thomas, J. Buschbeck, L. Schultz and S. Fahler: Appl. Phys. Lett. Vol. 92 (2008), p. 072502.

[47] J. W. Dong, J. Q. Xie, J. Lu, C. Adelmann, C. J. Palmstrom, J. Cui, Q. Pan, T. W. Sheild, R. D. James and S. McKernan: J. Appl. Phys. Vol. 95 (2004), p. 2593.

[48] P. G . Tello, F. J. Castano, R. C. O'Handley, S. M. Allen, M. Esteve, F. Castano, A. Labarta and X. Batlle: J. Appl. Phys. Vol. 91, No. 10 (2002), p. 8234.

[49] Y. Murakami, D. Shindo, M. Suzuki, M. Ohtsuka and K. Itagaki: Acta Mater. Vol. 51 (2003), p. 485.

[50] M. Ohtsuka, M. Matsumoto, K. Itagaki: J. Intelligent Matr. Sys. and Struc. Vol. 17 (2006), p. 1069.

[51] Segui C., Chernenko V. A., Pons J., Cesari E., Khovailo V. and Takag T.: Acta Materialia Vol. 53 (2005), p. 111.

[52] W. H. Wang, Z. H. Lie, J. Zhang, J. L. Chen, G. H. Wu, W. S. Zhang, T. S. Chin, G. H. Wen and X. X. Zhang: Physical Review B Vol. 66 (2002), p. 052411.

[53] J. Buschbeck, R. Niemann, O. Heczko, M. Thomas, L. Schultz and S. Fahler: Acta Materialia Vol. 57 (2009), p. 2516.

[54] P. Entel, V. D. Buchelnikov, V. V. Khovailo, A. T. Zayak, W. A. Adeagbo, M. E. Gruner, H. C. Herper and E. F. Wassermann: J. Appl. Phys. Vol. 39 (2006), p. 865.

[55] V. A. Chernenko: Advanced Materials Research Vol. 52 (2008), p. 3.

[56] N. Lanska, O. Soderberg, A. Sozinov, Y. Ge, K. Ullakko and V. K. Lindroos: J. Appl. Phys. Vol. 95:12 (2004), p. 8074.

[57] V. A. Chernenko, V. A. L'vov, V. V. Khovailo, T. Takagi, T. Kanomata, T. Suzuki and R. Kainuma: J. Phys.: Condens. Matter Vol. 16 (2004), p. 8345.

[58] P. J. Brown, A. Y. Bargawi, J. Crangle, K. U. Neumann and K. R. A. Ziebeck: J. Phys. :Condens. Matter Vol. 11 (1999), p. 4715.

[59] A. Sozinov, A. A. Likhachev, N. Lanska, O. Soderberg, K. Ullakko and V. K. Lindroos: *Proceedings of SPIE, Active Materials, Behavior and Mechanics Vol. 4699*, edited by Christopher S. Lynch (SPIE Digital library 2002), p. 195.

[60] X. Jin, M. Marioni, D. Bono, S. M. Allen and R. C. O' Handley: J. Appl. Phys. Vol. 91, No. 10 (2002), p. 8222.

[61] K. Tsuchiya, A. Ohashi, D. Ohtoyo, H. Nakayama, M. Umemoto and P. G. McCormick: Mater. Trans. JIM Vol. 41 (2000), p. 938.

[62] J. Enkovaara, O. Heczko, A. Ayuela and R. M. Nieminen: Physical Review B Vol. 67 (2003), p. 212405.

[63] P. J. Webster and K. R. A. Ziebeck and S. L. Town: Phil. Magazine B Vol. 94, No. 3 (1984), p. 295.

[64] V. A. Chernenko, E. Cesari, V. V. Kokorin and I. N. Vitenko: Scr. Matell. Mater. Vol. 33, No. 8 (1995), p. 1239.

[65] K. S. Sree Harsha: *Principles of physical vapor deposition of thin films* (Elsevier, 2006).

[66] S. Hiroyasu, K. Takeo, A. Shigeo and S. Katsuhiro: MRS Bull. Vol. 33, No. 2 (2008), p. 96.

[67] R. Hultgren, P. D. Desai, D. T. Hawkins, M. Gleiser and K. K. Kelley: *Selected values of the thermodynamic properties of the elements* (American Society of Metals, Ohio, 1973).

[68] N. Matsunami , Y. Yamamura, Y. Itikawa, N. Itoh, Y. Kazumata, S. Miyagawa, S. Morita, R. Shimizu, H. Tawara: in *Energy dependence of the ion-sputtering yields of monoatomic solids*: in *Atomic data and nuclear data tables* Vol. 31, No.1, (Elsevier, 1984), p. 1.

[69] H. Rumpf, J. Feydt, D. Lewandowski, A. Ludwig, B. Winzek and E. Quandt: Active Materials: Behavior and Mechanics, Proceedings of SPIE 2003 Vol. 5053 (2003), p. 191.

[70] K. Barbalace: *http://EnvironmentalChemistry.com/yogi/periodic/ atomicradius.html* Periodic Table of Elements - Sorted by Atomic Radius (EnvironmentalChemistry.com 1995 – 2010), Accessed on-line on 4/22/2010.

[71] F. Bernard, P. Delobelle, C. Rousselot and L. Hirsinger: Thin Solid Films Vol. 518 (2009), p. 399.

[72] M. Ohtsuka, M Matsumoto and K. Itagaki: J. Phys. IV:JP Vol. 122 II (2003), p. 899.

[73] W. Kraus and G. Nolze: *Windows version of PowderCell 1.0*, J. Appl. Crystallogr. Vol. 29 (1996), p. 301.

[74] J. Laugier and B. Bochu: Windows version of Checkcell, a program for analyzing the solutions given by powder indexing programs, Laboratoire des Materiaux et du Genie Physique, Date not available.

[75] S. K. Wu, K. H. Tseng and J. Y. Wang: Thin Solid Films Vol. 408 (2002), p. 316.

[76] J. Z. Chen and S. K. Wu: J. Non-Cry. Solids Vol. 288 (2001), p. 159.

[77] S. Rios, I. Karaman and X. Zhang: Appl. Phys. Lett. Vol. 96 (2010), p. 173102.

[78] R. Santamarta, E. Cesari, J. Muntasell, J. Font, J. Pons and P. Ochin: Intermetallics Vol. 18 (2010), p. 977.

[79] A. Gebert, S. Roth, S. Oswald and L. Schultz: Corrosion Sci. Vol. 51 (2009), p. 1163.

[80] I. Dadda, H. J. Maier, I. Karaman and Y. I. Chumlyakov: Acta Materialia Vol. 57 (2009), p. 6123.

[81] M. L. Richard, J. Feuchtwanger, S. M. Allen, R. C. O' Handley, P. Lazpita, J. M. Barandiaran, J. Gutierrez, B. Ouladdiaf, C. Mondelli, T. Lograsso and D.Schlagel: Philosophical Magazine Vol. 87 (2007), p. 3437.

VITA

Nishitha Jetta received her Bachelor of Engineering degree in Mechanical Engineering from Osmania University, Hyderabad, India in 2007. In August 2007, she started her Master of Science program in Mechanical Engineering at Texas A&M University. She received her M.S. degree in August 2010.

During her graduate study, she held positions as student worker and research assistant. Her major areas of study are Thin film deposition, Materials characterization, Microelectronic process engineering and MEMS fabrication technology. She may be reached at nishiitha.j@gmail.com.

Address:

Department of Mechanical Engineering,

Texas A&M University,

3123 TAMU,

College Station TX 77843-3123.